UNIVERSITÉ PARIS.DIDEROT (Paris 7)

ÉCOLE DOCTORALE 404

MATIÈRE CONDENSÉE ET INTERFACES

THÈSE DE DOCTORAT

DYNAMIQUE DES FLUIDES ET DES TRANSFERTS

PABLO JAVIER COBELLI

MESURES RÉSOLUES EN TEMPS ET EN ESPACE D'ONDES À LA SURFACE DE L'EAU: APPLICATION AUX MODES PIÉGÉS

SPACE-TIME RESOLVED MEASUREMENTS IN WATER WAVES: FOCUS ON TRAPPED MODES

Thèse dirigée par Philippe PETITJEANS

Soutenue le 19 novembre 2009

JURY

M. Christophe Baudet	Rapporteur
M. Christophe Josserand	Rapporteur
M. Mathias Fink	
M. Patrice Le Gal	
M. Jacques Magnaudet	
Mlle. Agnès Maurel	Co-Directrice de Thèse
M. Vincent Pagneux	Co-Directeur de Thèse
M. Philippe Petitjeans	Directeur de Thèse

Résumé

Cette thèse est une contribution à la compréhension de certains phénomènes d'ondes de surface sur des problèmes d'intérêts actuels. Des résultats significatifs ont été obtenus grâce à une nouvelle technique de mesure de la surface libre qui a été mise au point pour ces études.

Cette technique de profilométrie optique consiste à projeter un réseau de franges sinusoïdales de caractéristiques connues sur la surface libre et à observer l'image projetée depuis une autre direction. La déformation de la surface, ainsi que la perspective introduisent une modulation locale de fréquence du réseau de franges. L'analyse de l'image déformée et sa comparaison avec une image de référence permet de reconstruire la déformation de la surface libre. En particulier, cette technique à l'avantage de déterminer le profil de la surface étudiée à partir de l'acquisition d'une seule image, ce qui permet l'étude des écoulements en temps réel et des processus dynamiques fortement non-stationnaires. La haute résolution spatiale et temporelle atteinte permettent pour la première fois l'exploration d'une grande variété de phénomènes à la surface d'un liquide.

Principalement deux études expérimentales sur des ondes de surface ont été effectuées. Dans la première, nous nous concentrons sur l'étude des résonances d'ondes de surface autour d'un cylindre circulaire de rayon a dans un guide d'onde de largeur $2d$ (modes piégés). Les paramètres adimensionnels pertinents sont, d'une part la fréquence des ondes kd (k étant le nombre d'onde) et, d'autre, le rapport d'aspect a/d entre le cylindre et le guide. Dans le cadre de cette étude, un grand nombre de rapports d'aspect ont été explorées.

Ce travail fournit la première caractérisation expérimentale complète des modes piégés dans l'espace des fréquences ainsi qu'une analyse détaillée de leur structure spatiale. Cette caractérisation a été obtenue en décomposant le champ de déformation de la surface libre en harmoniques du forçage, ce qui nous a permis d'évaluer la contribution relative des modes linéaires et non-linéaires. Nos résultats montrent que la composante linéaire est dominante dans nos expériences, ce qui valide les approches théoriques basées sur la théorie linéaire des ondes de surface. Une décomposition de la partie linéaire du champ de déformation de la surface libre en fonction des symétries naturelles du problème permet, pour la première fois, la mise en évidence expérimentale de la structure spatiale des modes piégés. Ils se manifestent comme des oscillations non propagatives de la surface libre, antisymétriques par rapport à l'axe longitudinal du guide, confinées au voisinage du cylindre. Deux types de modes piégés ont été observés : symétriques et antisymétriques perpendiculairement à l'axe du canal. Alors que le premier type de mode est toujours présent, le second n'a été observé que dans le cas des plus grands rapports d'aspect. Nos résultats sur la structure spatiale de ces modes confirment les prédictions théoriques issus d'une méthode d'expansion en multipôles.

La caractérisation en fréquence des modes piégés a été obtenue par une analyse en champ lointain plus précise qu'une simple mesure locale. En introduisant des coefficients de réflexion et de transmission pour les perturbations antisymétriques dans le guide, nous avons pu construire des courbes de résonance pour chacun des rapports d'aspect a/d étudiés. Sur ces courbes, l'apparition des modes piégés est mise en évidence par la présence d'un ou de deux pics de résonance.

Une forte asymétrie est observée dans ces courbes, qui ne s'ajustent pas au modèle classique de Breit-Wigner. Cette asymétrie a été aussi mise en évidence dans une étude numérique complémentaire. Afin de pouvoir décrire correctement ce comportement, nous avons proposé un modèle qui tient compte de la proximité de la fréquence de coupure du guide. Ce modèle nous a permis de reproduire l'asymétrie de nos courbes de résonance et a été validé expérimentalement par

nos résultats. Les résultats de cette étude sont synthétisés sur une courbe maîtresse qui illustre la dépendance de la fréquence adimensionnelle kd avec le rapport d'aspect a/d. Cette courbe est composée, comme attendue, de deux branches, qui correspondent aux deux types de modes piégés observés. Ces résultats montrent un excellent accord avec les prédictions théoriques existantes dans la littérature.

Dans la seconde étude expérimentale conduite dans cette thèse, la turbulence des ondes de flexion sur une plaque élastique mince est étudiée. Dans ce cas, des mesures de la déformation de la plaque (intégralement résolue dans l'espace et le temps) ont été utilisées pour déterminer, pour la première fois, le spectre tridimensionnel d'énergie de la turbulence d'ondes. L'analyse de ce spectre met en évidence la présence d'une cascade turbulente d'énergie : les petits nombres d'ondes étant caractérisés par une forte anisotropie associée au forçage, tandis que les grands nombres récupèrent l'isotropie. D'autre part, l'analyse du spectre tridimensionnel montre aussi que l'énergie est concentrée au voisinage d'une surface 2D, qui représente une relation de dispersion faiblement non-linéaire. Ce résultat expérimental indique la persistance de la structure spatio-temporelle des ondes dans la plaque.

Notre approche expérimentale de la turbulence d'onde a aussi révélé les principales caractéristiques des ondes faiblement couplées qui peuvent être comparées avec les prédictions de la théorie de la turbulence faible. Cette étude a confirmé et quantifié le comportement faiblement non linéaire des ondes composant la cascade turbulente. En outre, nos résultats ont confirmé que la puissance fournie et le spectre d'énergie suivaient la même loi d'échelle. Nous avons montré un bon accord entre les résultats expérimentaux et la théorie de la turbulence faible.

D'autres études préliminaires sont brièvement évoquées concernant le retournement temporel d'ondes de surface et l'évolution spatio-temporelle de la déformation de la surface d'une couche mince de liquide après l'impact d'une goutte.

Abstract

This thesis represents a contribution to the understanding of certain water wave phenomena of interest in current research. A number of significant results have been obtained by means of a new free-surface measuring technique that has been developed for such studies.

This optical profilometric technique consists in projecting a sinusoidal-profile fringe pattern of known characteristics onto the free surface and in observing the projected images from a different direction. The surface deformation, as well as the perspective, introduce a local frequency modulation of the fringe pattern. Analysis of the deformed image and its comparison with a reference image allow for the reconstruction of the free-surface deformation. In particular, this technique presents the advantage of determining the surface's profile from only one image, which allows the study of highly unstationary surface flows. The high spatio-temporal resolution achieved allow, for the first time, the exploration of a vast variety of water wave phenomena.

Two major experimental studies on surface waves have been carried out during the course of this thesis. In the first one, we focused on the study of water wave resonances around a circular cylinder of radius a placed symmetrically between the parallel walls of a waveguide of width $2d$ (trapped modes). The relevant dimensionless parameters in this case are the frequency of waves kd (k being the wavenumber), and a/d, the aspect ratio between the cylinder and the waveguide. In the framework of this study, several values of the aspect ratio have been explored.

This work provides the first complete experimental characterization of trapped modes in the frequency space, as well as a detailed analysis of their spatial structure. This caracterization has been obtained by decomposing the free surface deformation field in harmonics of the driving frequency, which has allowed us to evaluate the relative contribution of linear and non-linear modes. Our results show that the linear component is dominant in our experiences, therefore validating the theoretical approaches based on the linear theory of water waves. A decomposition of the linear deformation field in terms of the natural symmetries of the problem enables us, for the first time, to provide experimental evidence of the spatial structure of trapped modes. These manifest in the form of non-propagative oscillations of the free surface, antisymmetric with respect to the longitudinal axis of the waveguide, confined to the vicinity of the cylinder. Two different types of trapped modes have been observed: either symmetric or antisymmetric with respect to a line perpendicular to the walls passing through the center of the cylinder. While the first type of trapped mode is always present, the second type has only been observed in the case of the largest aspect ratios. Our results regarding the spatial structure of the trapped modes confirm the theoretical predictions arising from a multipole expansion method.

The frequency characterization of the trapped modes has been obtained by the analysis of the problem in the far field. By introducing reflection and transmission coefficients for the antisymmetric perturbations inside the waveguide, we were able to build resonance curves for every value of the aspect ratio a/d considered. On this curves, the occurrence trapped modes is evidenced by the presence of one or two resonance peaks.

A marked asymmetry is observed on these curves, which cannot be properly described by the classical Breit-Wigner shape. This asymmetry has been also found in a complementary numerical study. In order to describe adequately this behaviour, we have proposed a model which takes into account the proximity to the waveguide's threashold for propagation. This model allowed us to reproduce the asymmetry of the resonance curves and was successfully validated with the experimental results. Finally, all the experimental results are summarized on master curve, depicting the dependence of the trapped mode frequency kd with the aspect ratio a/d. This curve is composed,

as expected, by two branches, corresponding to the two types of trapped modes observed. This results show an excellent agreement with the predictions available in the literature.

The second experimental study conducted in the frame of this thesis regards the turbulence of bending waves in a thin elastic plate. In this case, fully space-time resolved measurements of the plate deformation have been employed to determine, for the first time, the three-dimensional energy spectrum of wave turbulence. Analysis of this spectrum shows the presence of a turbulent energy cascade: low wavenumbers are characterized by a strong anisotropy associated to the forcing, the isotropy being recovered at large wavenumbers. Moreover, analysis of the three-dimensional spectrum leads to the observation that the energy is mainly concentrated in the vicinity of a 2D surface, representing a weakly non-linear dispersion relation. This experimental result confirms the persistence of the spatio-temporal structure of waves comprising the turbulent cascade.

Our experimental approach for wave turbulence revealed also the principal characteristics of the weakly coupled waves that can be usefully compared with the predictions of weak turbulence theory. This study confirms and quantifies the weakly non-linear behaviour of the waves in the turbulent cascade. Furthermore, our results confirmed that the scaling law in the supplied power is the same for the energy spectrum. We have shown a bon accord between experimental results and weak turbulence theory.

Two other preliminary studies are briefly mentioned, regarding the time-reversal of water waves and the spatio-temporal evolution of the free surface after the impact of a drop.

SOME OF THE CONTENTS OF THIS WORK WERE PRESENTED AT THE FOLLOWING CONFERENCES AND SEMINARS

Étude expérimentale des modes d'ondes de surface piégés.
P. J. COBELLI, A. Maurel, V. Pagneux & P. Petitjeans
19ème Congrès Français de Mécanique 2009. Marseille, 28 Août 2009.

Modes piégés dans les ondes de surface.
P. J. COBELLI, A. Maurel, V. Pagneux & P. Petitjeans.
Séminaires du Laboratoire de Physique Statistique, École Normale Supérieure. Paris, 4 Mars 2009.

Étude expérimentale des modes piégés dans un guide d'ondes.
P. J. COBELLI, A. Maurel, V. Pagneux & P. Petitjeans.
Rencontre du Non Linéaire 2009, Institut Henri Poincaré. Paris, 12 Mars 2009.

Modes piégés à la surface d'un liquide.
P. J. COBELLI, A. Maurel, V. Pagneux & P. Petitjeans.
Journées de Physique Statistique 2009. École Supérieure de Physique et de Chimie Industrielles. Paris, 29 Javier 2009.

Ondes de surface : modes piégés.
P. J. COBELLI, V. Pagneux, A. Maurel & P. Petitjeans.
Journées Scientifiques de l'ESPCI – ParisTech. Paris, 20 Novembre 2008.

Mèthode globale pour la mesure de la hauteur de la surface libre d'un liquide.
P. J. COBELLI, P. Petitjeans, A. Maurel & V. Pagneux.
Première Rencontre École Polytechnique – ESPCI – Saint Gobain. Chaire 'Science des Materiaux et Surface Actives'. École Polytechnique à Paris, 22 Octobre 2008.

Profilomètrie 3D d'une surface liquide par une mèthode de projection de franges.
P. J. COBELLI, P. Petitjeans, A. Maurel & V. Pagneux.
Reunion du Groupe de Recherche 'Structure de la Turbulence et Melange'
GdR 2865 CNRS. CEMAGREF Rennes, 29 Janvier 2008.

CONTENTS

Contents **8**

1 Introduction **11**
1.1 Free surface phenomena and water waves . . . 11
1.2 The need for an experimental technique . . . 14
1.3 Topography of the free surface: a not so superficial study . . . 15
1.4 Organization of this thesis . . . 16

2 Global measurement of water waves **21**
Introduction . . . 22
Principle of the method . . . 25
Experimental setup . . . 26
Some ilustrative applications . . . 30
Concluding remarks . . . 31
References . . . 32

3 Phase-to-height relation in FTP **35**
Introduction . . . 36
Derivation of the phase-to-height relations . . . 39
Experimental results . . . 41
On Takeda's calculation . . . 44
Concluding remarks . . . 46
On the fringe spacing in crossed-optical-axes geometry . . . 47
The case of collimated projection . . . 48
References and notes . . . 49

4 Trapped modes in a water wave channel **51**
Main results . . . 55
Experimental study on water-wave trapped modes . . . 61
Introduction . . . 61
Experimental setup . . . 65
Resulting patterns . . . 70
Analysis of the experimental results and comparison with the linear theory . . . 76
Summary and conclusions . . . 88
References . . . 89

5 Wave turbulence in a plate **91**

6 Conclusions and perspectives **99**
6.1 Summary and conclusions 99
6.2 Perspectives 103

A Other experimental studies conducted during the course of this thesis **105**
A.1 Time reversal of water waves 105
A.2 Drop impact onto thin liquid films 107

Bibliography **111**

CHAPTER 1

INTRODUCTION

1.1 Free surface phenomena and water waves

Free surface flows are among the most rich and complex hydrodynamical phenomena commonly found in nature. It is perhaps the mesmerizing charm found in the refined balance between beauty and complexity that has amazed and captivated scientists from the very birth of physics [16]. It is indeed surprising to discover that personalities such as Newton, Laplace, Lagrange, Poisson and Cauchy (to name a few) were deeply involved in the early advances made in the understanding of free-surface phenomena, setting the scene for subsequent work in this area.

Presently, more than two hundred years after those pionneering efforts, free-surface phenomena still enjoys an unceasing interest from both the scientific and engineering communities. In particular, the last five decades have brought a renewed focus on free-surface flows, motivated by scientific and technological developments in closely related fields.

Some of the most prominent advances in this domain concern the interaction of surface waves, either with flow singularities or mutual. In the following paragraphs, we present some of these advances along with a discussion on their scope, limitations, and open questions that still remain to be attended.

The study of the interaction between surface waves and flow singularities can be further classified according to the nature of the singularities, either passive or active. By the term 'passive', we mean an object (or a set of objects) whose presence modifies the original wave field but which does not react to the flow; *e.g.*, a fixed obstacle facing surface waves. Active singularities amount to flow structures such as a vortex, a jet or a floating structure, whose dynamics results from a significative energy exchange with the incident wave field.

The occurrence of trapped modes in water wave theory is one of the most important and striking recent results in the study of the interaction between waves and flow singularities. Consider, for example, the problem of the interaction of linear water waves with a freely-floating structure in open water. In the framework of the classical theory of water waves, this problem is conventionally treated in the frequency domain, where it is decomposed in the so-called scattering and radiation

problems. In the scattering problem, the structure is held fixed in the incident wave field at its prescribed frequency, whereas in the radiation problem the structure is forced to oscillate in the same frequency but in the absence of waves. Both problems are closely related by the equations of motion for the freely-floating structure, differing only in the boundary condition imposed on the surface of the structure which holds the information regarding the forcing.

Solutions to these scattering and radiation problems have been studied since the 50's and, although no proof was available at the time, most researchers in the field believed that such solutions were unique (for a given structural geometry and for every frequency). However, this belief was overthrown by the discovery of trapped modes. A trapped mode is a finite-energy *free* oscillation of the fluid localized in the vicinity of the fixed structure and corresponds to bound states occurring in many situations in physics. For a given structure, trapped modes may exist only at discrete frequencies.

It was later observed that, whenever such modes exist for a particular structure (or array of structures), forcing at the trapped modes eigenfrequency leads to particularly sharp resonances. The implications of this property of trapped modes are multiple, and whether they represent an exploitable feature or are considered to be an inconvenience varies according to the particular problem under study.

For instance, high quality factors in trapped modes resonances are decisive for the design of the so-called metamaterials, whose remarkable properties, such as negative refraction index and cloacking, rely on the resonant nature of their response.

Within the framework of environmental engineering and renewable energy development, in which much effort is being directed towards the design of systems capable of harnessing the energy from the ocean, the occurrence of trapped modes could indeed be the basis of an effective hydroelectrical power device. In assessing the feasibility of such a device, two crucial concerns arise. The first one is whether the bandwidth around a trapped mode frequency is substantially different from that of the near-resonant motions already familiar to designers of wave-power devices. The degree of spatial localization of the energy, as well as its dependency with the structure's characteristics, constitutes the second regard. Although a large literature exists covering many theoretical aspects of the occurrence of trapped modes, these questions still remain as open subjects which evidence the need of a more detailed study on both the frequency and spatial characteristics of the trapped modes.

In the case of marine and coastal engineering, where large off-shore structures based on piles are being built (such oil rigs and stockage platforms, airports and breakwaters), the occurrence of such resonances results in the presence of large loads on the individual elements of the array, and could eventually lead to structural damage. For this reason, their study is of fundamental importance to ensure the successful and safe design of these structures.

Incidentally, another reason the existence of trapped modes should be of concern to engineers steams from the fact that standard numerical methods commonly employed in the design and analysis of structures in interaction with fluid flows will inevitably fail at, or very close to, a trapped mode frequency.

Turning to the interaction of water waves with active singularities, the scattering of surface waves by a (vertical) vortex is a case of particular importance. In the first place, the study of the multiple aspects of this interaction serves as a building block in the understanding of more general and encompassing problems like the scattering of sound by complex vortical structures and the propagation of sound through turbulent flows. In this case, and despite the large amount of data

available from both theoretical and experimental studies, many basic questions such as the respective contributions of large structures of the mean flow in the scattering process are not clearly established and need further consideration.

Moreover, there is another aspect of this system that renders it attractive to theoretical physicists. This steams from the fact that wave–vortex interactions constitute a classical analogue of the Aharonov–Bohm effect, in which the dynamics of a charged quantum particle is affected by the electromagnetic potential even in regions where the associated field vanishes. However, and as opposed to the quantum case, wavefront dislocations arising from this interaction are physically observable. In this sense, the study of the water wave case could shed some light into more fundamental aspects of the quantum interaction that are not always abordable experimentally.

As we have stated before, the study of the diverse mechanisms of mutual interaction between surface waves is another prominent field that has renewed the interest of the scientific community in free surface flows. In the framework of this general problem, wave turbulence is perhaps the area in which most significant advances have been made in the last few years.

Wave turbulence is a non-equilibrium state of waves in non-linear interaction; the case of gravity waves at the surface of the ocean being the archetypal example. Many other systems belong to this class and wave turbulence have been observed in a variety of contexts including capillary waves, atmospheric waves, superfluids, elasting bending waves in plates, non linear optical waves and Alfvén waves in solar winds.

In a manner that is similar to the phenomenological theory of hydrodynamic turbulence, the so-called weak-turbulence theory for wave turbulence predicts a Kolmogorov-Zakharov energy cascade. This analytical theory assumes the persistence of the space-time structure of the linear waves through the dispersion relation. In spite of the large amount of theoretical advances, very few experimental studies have taken place and available results only show partial agreement with the theoretical predictions. This is related to the fact that almost none of these experiments look beyond the analysis of measurements at a single point, which also implies the use of a 'wave turbulence equivalent' for the Taylor hypothesis in hydrodynamic turbulence in order to relate space scales to time scales (and viceversa).

Beyond the framework of surface wave interaction, the study of the interaction of isolated coherent structures, such as jets, vortices and vortex rings with a free surface is of particular interest to free-surface turbulence, as it constitutes a very valuable departure point in illustrating the connection between columnar vortices in the fluid and the surface dimples above their low-pressure cores.

Free-surface turbulence is primarily concerned with the state of a free surface above a turbulent flow. In this area, the driving question is how the statistical properties of the turbulent crispations of the surface are linked to those of the turbulent velocity field beneath it. This is a matter of particular importance, for example, in understanding the exchange of heat and mass between the atmosphere and the ocean, which is determined by the small-scale roughness of the ocean's surface. These transport processes are crucial for the global distribution of momentum, heat and chemical species.

One of the most stricking recent experimental results regarding this problem is related to the validity of Taylor's frozen turbulence hypothesis, *i.e.*, that the eddies are essentially fixed and do not change considerably as they are advected by the flow. This hypothesis, applicable to the measurement of the turbulent velocity field with a relatively large mean velocity, allows measured time



Figure 1.1: Photograph of the free surface deformation generated by a pinned vertical vortex in fast rotation as observed in our experiments (zoom). The vortex core is clearly discernible, and a spiral wave originating at its center can be observed as well. The smallest yet most interesting details of the free surface deformation, such as those connected to the interaction between emitted waves, are hardly visible to the naked eye, and have been enhanced for this particular visualization by the use of grazing light. [In this image, the vortex core is of about 3 cm in diameter.]

series recorded at a fixed point to be interpreted as fluctuations along a line in the mean flow direction. It has been shown that, while Taylor's hypothesis works for a turbulent velocity field, the same statement does not hold for its free surface due to the emergence of relatively fast capillary–gravity waves.

Moreover, although homogeneous and isotropic turbulence is well documented and its interaction with a free surface has been explored numerically, there are still some basic yet highly non-trivial questions that need to be addressed. For instance, one of such questions is how the spatial energy spectrum of the subsurface turbulent velocity field is reflected in the surface. It is worth noting that the answer to this question is still unknown even for the case in which surface deformations are not very strong, not to mention much more spectacular manifestations of free-surface turbulence, such as breaking and frothing of the surface.

1.2 The need for an experimental technique

Further progress in the understanding of the problems previously discussed strongly depends on the availability of experimental results, from which theories could be built and predictions compared, and to which numerical models could be validated. Indeed, due to the complexity of the phenomena involved, theoretical tractability is not always assured (*e.g.*, the condition at the line of contact between the free surface and any surface-piercing body when surface tension effects

are not negligible) or is limited to some particular regime or approximation (*e.g.*, trapped modes within the linear theory of waves, sound–vortex interaction in the low-Mach-number regime). In the case of numerical studies, the application of realistic boundary conditions on the free surface makes simulating the free surface a daunting task. In addition, such studies are further constrained by often prohibitely high computational costs (notably in the cases of wave or free-surface turbulence).

In that sense, almost every open question in these areas seems to bring to our attention the need for an appropriate experimental technique, capable of performing whole-field fully resolved space-time measurements of the free surface deformation and evolution.

In light of this, many novel techniques have been developed in the last years for the measurement of the free surface deformation. Laser surface scanning, diffusing light photography, stereoscopic topography, free-surface gradient detection and digital image correlation constitute examples of such endeavours. Unfortunately, most of the available techniques are problem-specific, and rapidly face difficulties to adapt to other slightly different physical systems. Moreover, some of them are restricted to the measurement of stationary or periodic processes, or limited to thin layers of fluid. In any case, these and other deficiencies and limitations render them rather inadequate for studying the free surface phenomena of interest to the present work.

This concise description (which will be discussed in further detail in Chapter 2) represents a snapshot of the state-of-the-art of the measurement techniques available for the topography and time-tracking of the free surface as it was at the beginning of this thesis. In the aim of overcoming this lack, our primary efforts during the course of this work were pointed towards the development of a novel experimental technique that would allow for space-time resolved measurements of the free surface.

1.3 Topography of the free surface: a not so superficial study

In addition to the intrinsic value that all topographic studies hold, the measurement of the detailed state and time-evolution *of a free surface* offers another profitable aspect that is worth mentioning. Indeed, and although the study of the free surface deformation is of interest *per se*, under certain conditions, such a characterization could also lead to valuable information regarding *other* hydrodynamical variables of the flow *beneath* the surface.

For instance, in the case of stationary, planar and inviscid flow with negligible surface tension, it could be shown that the surface gradient field, $\nabla h(\mathbf{x})$, equals the normalized convective acceleration, *i.e.*, $\nabla h = -(\mathbf{u}\cdot\nabla)\,\mathbf{u}/g$; $\mathbf{u}$ being the velocity field and g the acceleration of gravity.

Another example regards the study of the interaction between underlying coherent structures and the free surface, and is of particular relevance to free-surface turbulence. For low Froude numbers[1], Dommermuth et al. [19] showed that the equations of motion for the fluid can be reduced to a form in which, in the absence of atmospheric pressure, surface elevation is hydrostatically balanced by the vortically induced pressure. This allows the indirect determination of the pressure field near the surface through the measurement of the free surface deformation.

[1] The Froude number (named after William Froude (1810-1879), english engineer and hydrodynamicist), is a dimensionless number comparing the potential energy due to gravity to the kinetic energy in the flow.

Connections between the deformation of the free surface and other subsurfacic hydrodynamical variables of the flow are of particular interest in those cases for which theoretical results regard only in-flow quantities. Whenever such links can be established, the measurement of the free surface deformation allows the contrast of existing theoretical predictions without resorting to direct bulk measurements which are not always accessible to the experimenter.

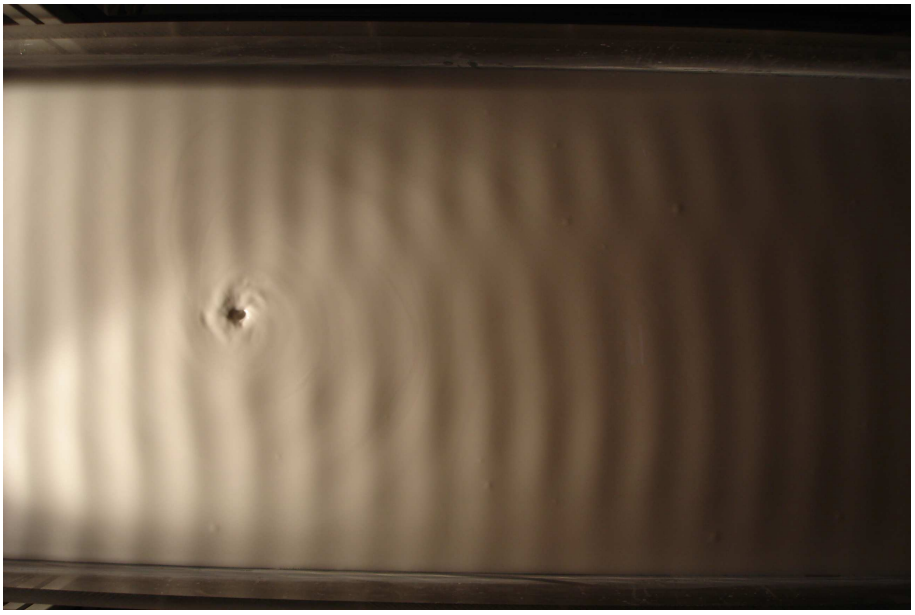
1.4 Organization of this thesis

The first two chapters of this thesis are devoted to the detailed description of our profilometric measurement technique. The first chapter presents the technique as well as the measuring system, along with an experimental validation and numerical tests. Finally, some illustrative examples of the application of this measuring system are presented, depicting its potentialities over a variety of fluid dynamics' scenarios.

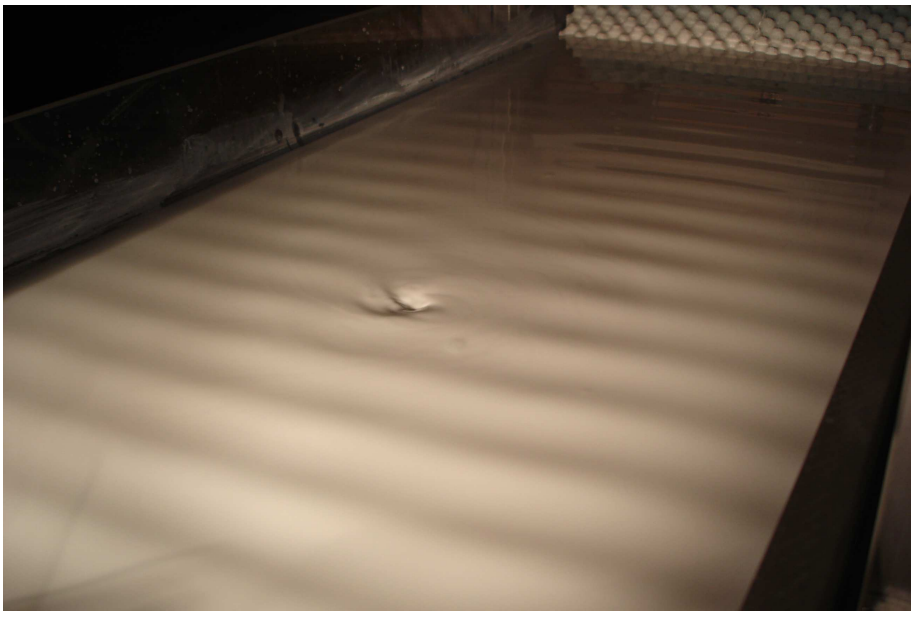
The second chapter introduces the exact theoretical derivation of the techniques' reconstruction formulas, together with corrections to errors found in the existing literature regarding fringe projection profilometry. These theoretical results extend beyond a particular experimental setup to include all the possible configurations and geometries of the profilometric system introduced in the first chapter. These derivations are sucessfully validated by means of a joint experimental study.

One of the most important experimental results obtained during the course of this thesis concerns an extensive experimental study on water-wave trapped modes, which is the subject of Chapter 4. We present there the first experimental evidence for the existence of trapped modes around an obstacle in a water wave channel. This extensive study, made possible by the development of our profilometric measuring technique, includes the detailed characterization of the spatial structure and eigenfrequencies of the observed trapped modes, which are successfully compared to the theoretical predictions available in the literature.

Chapter 5 deals with the experimental study of wave turbulence in a slightly different physical system: bending waves in a thin elastic plate. In this case, our optical profilometric technique is employed to measure the dynamics of the plate's deformation in a large portion of its surface, leading to the first experimental observation of a full space-time spectrum. Experimental results are discussed and compared to the predictions of weak turbulence theory.

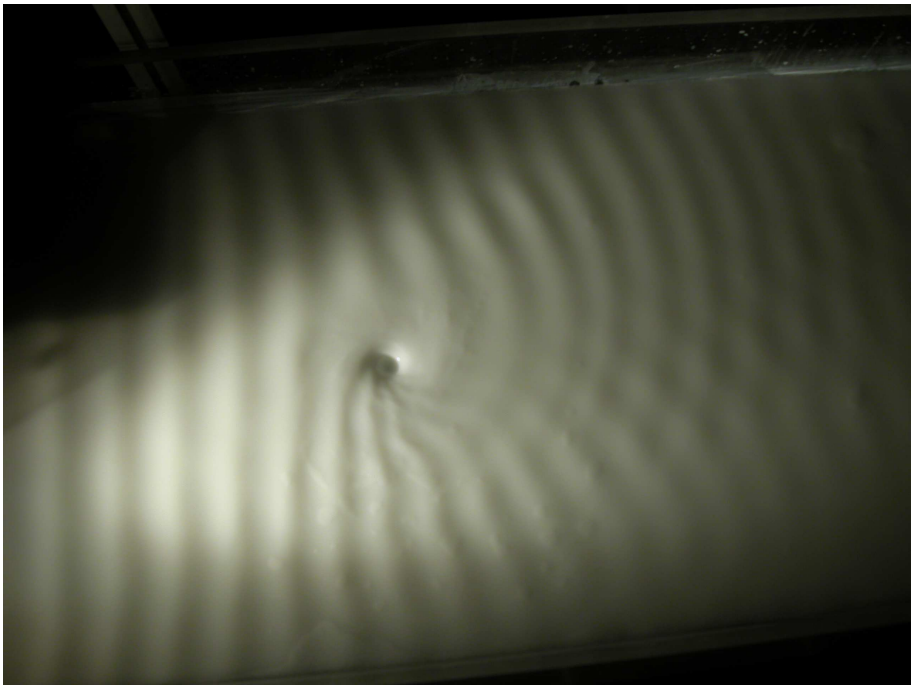


(a) top view



(b) perspective view

Figure 1.2: Photographs of the free surface deformation resulting from the interaction of plane surface waves with a pinned vertical vortex as observed in our experiments. In this visualization, plane waves travel from left to right, and the vortex rotates counterclockwise. Both photographs reveal the presence of a dislocation line in the wavefront past the vortex position. [In this image, the vortex core is of about 2 cm in diameter.]

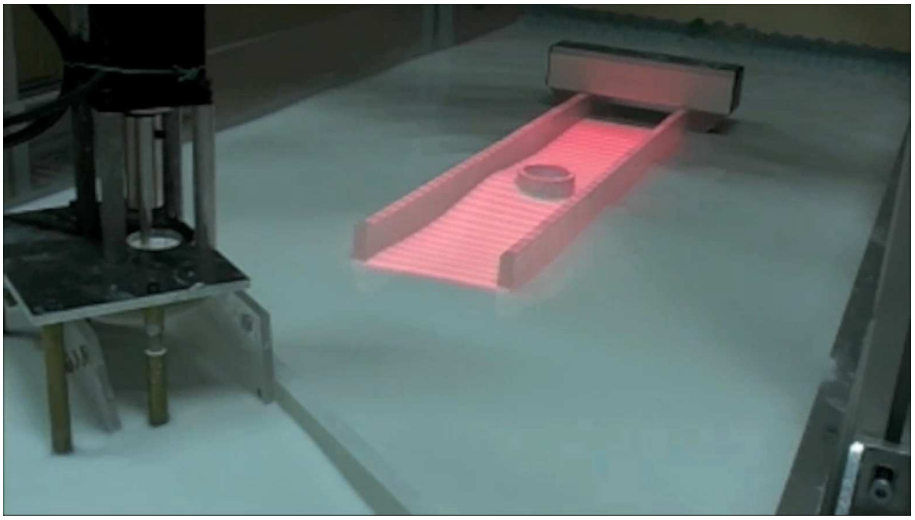


(a) top view

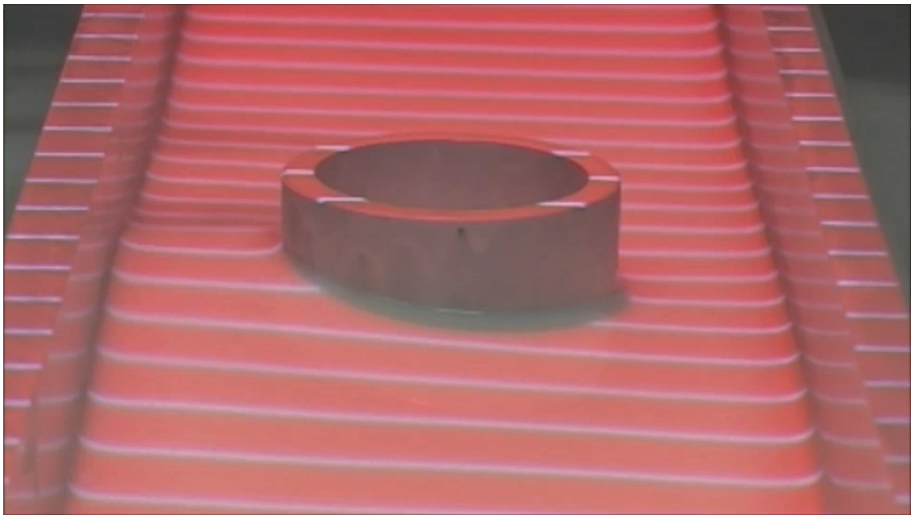


(b) perspective view

Figure 1.3: Photograph of the free surface deformation resulting from the interaction of plane surface waves with a pinned vertical vortex in fast rotation as observed in our experiments. In this visualization, plane waves travel from left to right, and the vortex rotates clockwise. This visualization shows a strong interaction, evidenced by the richness of features in the free surface. [In this image, the vortex core is of about 3 cm in diameter.]



(a) perspective view



(b) close-up on the region near the obstacle

Figure 1.4: Photograph of the setup employed in this thesis for the study of trapped modes. Panel (a) shows a perspective view of the setup, depicting our wave tank, the waveguide and the surface-piercing cylinder place symmetrically between its walls. The wavemaker is visible at the left of the picture. An asymmetric perturbation is observed in the vicinity of the obstacle, indicative of the presence of a trapped mode. Panel (b) illustrates such asymmetric perturbation with a close-up on the region of interest. In this photographs, a pattern of parallel red and white lines is projected onto the surface of interest in order to enhance the visualization of its deformation. [Water height at rest: 5 cm; waveguide's width: 100 mm; obstacle's diameter: 50 mm. Photograph taken at the experimentally determined trapped mode (eigen)frequency for this configuration.]

CHAPTER 2

GLOBAL MEASUREMENT OF WATER WAVES BY FOURIER TRANSFORM PROFILOMETRY

This chapter is composed by an article published in *Experiments and Fluids* [10]. It describes in detail the optical profilometric technique that I have set up during the first year of my thesis and subsequently employed for the measurement of free-surface deformation fields. The development of this technique, which allows for single-shot, global and non-intrusive measurement of free surface deformations over large areas, represents the foundations onto which the subsequent experimental studies performed during the course of this thesis are built.

Standard fluid measuring techniques for free-surface deformations are usually limited to a few point measurements, employing either one or an array of synchronized sensors. Furthermore, many of those methods involve the use of surface-piercing elements (such as resistive- or capacitive- probes) which are intrinsically intrusive. In any case, such methods only allow for a small number of discrete localized measurements, so that the information on the detailed spatial aspects of the free-surface deformation and the propagation of disturbances is incomplete. These limitations have led us to develop a novel technical technique for the accurate measurement and tracking of the three-dimensional topography of free-surface deformations.

The optical profilometric technique that we developed is based on the principle employed in fringe projection profilometry. A fringe pattern of known spatial frequency is projected onto the free surface and its image is recorded by a camera. The topography of the surface introduces a frequency modulation in the observed pattern, which is also modified by the perspective due to the relative positioning and orientation of the projection–recording system. The deformed fringe pattern is later compared to the undeformed (reference) one, leading to a phase map from which the free surface can be reconstructed.

In order to be able to project images onto the liquid surface, its light diffusivity is enhanced by the addition of a white liquid dye. Although the use of dye renders the liquid opaque, precluding the simultaneous use of introspective optical techniques (*e.g.*, Particle Image Velocimetry and Laser Doppler Velocimetry), bulk measurements are still possible using acoustic techniques (such as Ultrasonic Doppler Velocimetry).

Fringe projection onto the surface is achieved by the use of a high-resolution videoprojector,

allowing for the projection of wavelength-controlled sinusoidal-profile fringe patterns, which considerably increases the overall performance of the technique and the quality of the reconstruction. Moreover, as the technique poses no restrictions on the time-tracking of the free-surface deformation (other than that arising from the exposure time), the obtention of time-resolved measurements of the surface's evolution is only limited by the capturing system's acquisition rate.

Among the examples of the application of this measuring technique to fluid dynamics problems presented in this chapter, the measurement of small-amplitude surface waves emitted by a pinned vortex is perhaps the most eloquent. In this case, we studied the non-stationary emission of weak amplitude spiral surface waves from the core of a vortex in fast rotation. Although the wave amplitude is weak in comparison to the vortex core even near the source (the waves ware barely noticeable to the naked eye even in grazing light) we show that the technique is able to detect and reconstruct remarkably well the smallest structures, discerning perturbations of amplitudes throughout more than two orders of magnitude in a single-shot measurement.

Finally, the system has the additional advantage of being easily scalable, so that it can be adapted for any specific application, ranging from small or medium scale laboratory experiments to large applications such as those considered in hydraulic engineering.

Exp Fluids (2009) 46:1037–1047
DOI 10.1007/s00348-009-0611-z

RESEARCH ARTICLE

Global measurement of water waves by Fourier transform profilometry

Pablo Javier Cobelli · Agnès Maurel · Vincent Pagneux · Philippe Petitjeans

Received: 29 May 2008 / Revised: 8 December 2008 / Accepted: 5 January 2009 / Published online: 24 January 2009
© Springer-Verlag 2009

Abstract In this paper, we present an optical profilometric technique that allows for single-shot global measurement of free-surface deformations. This system consists of a high-resolution system composed of a videoprojector and a digital camera. A fringe pattern of known characteristics is projected onto the free surface and its image is registered by the camera. The deformed fringe pattern arising from the surface deformations is later compared to the undeformed (reference) one, leading to a phase map from which the free surface can be reconstructed. Particularly, we are able to project wavelength-controlled sinusoidal fringe patterns, which considerably increase the overall performance of the technique and the quality of the reconstruction compared to that obtained with a Ronchi grating. In comparison to other profilometric techniques, it allows for single-shot non-intrusive measurement of surface deformations over large areas. In particular, our measurement system and analysis technique is able to measure free surface deformations with sharp slopes up to 10 with a 0.2 mm vertical resolution over an interrogation window of size 450×300 mm^2 sampled on approximately 6.1×10^6 measurement points. Some illustrative examples of the application of this measuring system to fluid dynamics problems are presented.

P. J. Cobelli (✉) · P. Petitjeans
Laboratoire de Physique et Mécanique des Milieux Hétérogènes, UMR CNRS 7636, École Supérieure de Physique et de Chimie Industrielles, 10 rue Vauquelin, 75231 Paris Cedex 05, France
e-mail: cobelli@pmmh.espci.fr

A. Maurel
Laboratoire Ondes et Acoustique, UMR CNRS 7587, École Supérieure de Physique et de Chimie Industrielles, 10 rue Vauquelin, 75231 Paris Cedex 05, France

V. Pagneux
Laboratoire d'Acoustique de l'Université du Maine, UMR CNRS 6613, Avenue Olivier Messiaen, 72085 Le Mans Cedex 9, France

1 Introduction

Free-surface water waves phenomena enjoys an unceasing interest from both the fluid scientists and engineering communities. In general, the defining characteristic of free-surface flows is the presence of a deformable interface, which by itself provides for an interaction mechanism between the base flow and the external environment. For a vast variety of cases, this interaction is far from being negligible, and often its effects can lead to a drastic change in the hydrodynamical characteristics and time evolution of the flow. In such flows, the interaction between the interface and the underlying flow is made evident in the form of deformations of the free surface. The detailed shape of these deformations is determined by a delicate balance between the local pressure below the surface and its vertical acceleration, on one hand, and gravity and interfacial tension (associated with the surface's local curvature), on the other.

Therefore, the experimental study of free-surface deformation (herein referred to as FSD) in free-surface flows constitutes the keystone to understanding the complex mechanisms that govern its interaction with the underlying near-surface flow. In recent years, many theoretical, numerical and experimental studies on free surface deformation were conducted to understand its interaction with a vast variety of basic flows, such as vortices and vortex rings (Ruban 2000; Gharib 1994; Gharib and Weigand 1996), as well as jets (see, e.g., Walker et al. 2006), as well as with

turbulent flows (Savelsberg et al. 2006; Savelsberg and van de Water 2008).

Although much work has been done to aid our understanding of FSD, it is clear that both theoretical predictions and numerical results still need detailed experimental validation through a suitable measuring technique.

Standard measuring techniques for FSD in fluid flows are usually to a few point measurements, employing either one or an array of gauges. These methods only allow for discrete localized measurements, so that the information on the 2D aspects of FSD and disturbances' propagation is incomplete. These limitations and deficiencies led fluid experimentalists to the development of novel optical techniques for the accurate measurement and tracking of the 3D-topography of FSDs.

Cox (1958) determined the surface elevation by the refraction of light through the free-surface. A light source of spatially linearly-varying intensity was placed at the bottom of a water tunnel and a telescope imaged one point on the water surface into a photocell. The intensity of the light recorded by the photocell is related to one component of the slope of the free-surface. This technique is commonly known as "refractive mode" since the light rays are refracted through the surface. Likewise, a technique known as "reflective mode" permits observation of the free surface by illumination of the liquid surface from above. Zhang and Cox (1994) and Zhang et al. (1994) devised a technique for measuring the FSD by using a free-surface gradient detector (FSGD). The principle behind this method is to color-code the surface slopes (for further details on the technique, see Zhang et al. 1996; Zhang 1996). This technique was later combined with digital particle image velocimetry (Dabiri and Gharib 2001; Dabiri 2003) to study near-surface flows by constructing correlations between small-sloped FSDs and near-surface velocities.

Diffusing light photography was employed by Wright et al. (1996) to study FSD under fully developed isotropic ripple turbulence, and later on for the imaging of intermittency (Wright et al. 1997). In their technique, the fluid is illuminated from below with a 10-μm light flash that diffuses through the liquid as a result of multiple scattering from a diluted suspension of 1-μm-polystyrene spheres. Light intensity reaching the air–liquid interface depends on the local depth, so that less light penetrates deeper regions. Calibrating the transmission of light as a function of fluid depth leads to the instantaneous height of the fluid surface, even when it presents large variations in height and curvature. This technique works for light transport mean free paths (i.e., the distance over which a ray scatters through a large angle) larger than the surface displacement but smaller than the fluid depth. Although precise, this technique is very delicate to implement particularly due to the constraints imposed on particle concentration control. For measuring the global FSD caused by the interaction of surface waves impinging on a single fixed vortex, Vivanco and Melo (2004) scanned the whole surface measuring at each point the deflection of a reflected laser beam. Although the method provides for a measure of the amplitude and phase of the surface deflection, its range of application is limited to stationary or periodic processes. Tsubaki and Fujita (2005) and Benetazzo (2006) presented two different stereoscopic methods for measuring 2D water surface configurations. Their method consists on using a pair of sequential images captured by two cameras arranged in stereo position. This method is suitable for the accurate measurement of both small-amplitude waves and surface discontinuities. Recently, Moisy et al. (2008) proposed an optical technique based on digital image correlation. A set of random points printed at the bottom of a channel is observed through the deformed surface. The apparent displacement field observed between the refracted and the reference images allows for the determination of the local surface slope. Being a refractive technique, the main limitation of the method is due to caustics generated by strong curvature or large surface-pattern distance.

Fringe projection profilometry was first employed by Grant et al. (1990) to measure the FSD associated to water waves using the projection moiré method (see e.g. Patorski 1993). However, wave probes had to be used to resolve the ambiguity associated to the polarity of the fringes (i.e., which fringes represent peaks and which represent throughs) and to obtain an absolute measure of elevation above the mean water level. Zhang and Su (2002) proposed a particular fringe projection profilometric technique commonly known as Fourier transform profilometry (FTP) (see Takeda et al. 1982; Takeda and Mutoh 1983; Su and Chen 2001) for the measurement of FSDs and presented experimental results on a vortex' shape at a free surface. Recently, Cochard and Ancey (2008) developed a measuring system based on Phase Shifting and FTP applied to the dam-break problem (i.e., the sudden release of a volume of liquid down a slope) and measured the time-evolution of the flow.

In order to further our understanding of FSD mechanisms, this paper presents an optical profilometry technique that allows for high-resolution 3D whole-field reconstruction of time-dependent FSD fields. Our technique is based on fringe projection profilometry, which has been successfully employed for the topography of solid surfaces in a wide variety of fields, such as 3D sensing systems, mechanical engineering, machine vision, robotic control, industry monitoring and quality assesment, biomedicine, etc. In this work, we propose both the liquid surface extension of this technique along with several significant

improvements in the optical setup as well as in the signal processing algorithm.

Our presentation is organized in five sections as follows. Section 2 briefly summarizes the principle of FTP, upon which our measuring technique is based. In Sect. 3, we describe both the complete experimental system, measurement protocol and data processing algorithm developed to measure the liquid's free-surface deformation. Limitations of the method, such as maximum range of measurement, system's resolution and accuracy are discussed as well. Section 4 is divided into three sections providing diverse illustrative applications of our measuring technique. Finally, the last section presents concluding remarks.

2 Principle of the method

Although there exists a vast variety of implementations of fringe projection profilometry, the underlying principle common to all of them is very simple. In its more elementary form, a typical fringe projection profilometry setup consists of a projection device and an image recording system. A fringe pattern of known characteristics is projected onto the test object and the resulting image is observed from a different direction. Since projection and observation directions are different, the registered fringe pattern is distorted according to the object's profile and perspective. From the point of view of information theory, we could say that the object's depth information is encoded into a deformed fringe pattern recorded by the acquisition sensor, allowing it to be measured by comparison to the original (undeformed) grating image. It is therefore the phase shift between the reference and deformed images which contains all the information of the deformed object.

In this paper, we present an improvement of both the measuring system and the analysis algorithm based on a particular fringe projection profilometry known as FTP, first introduced by Takeda et al. (1982).

In its simplest formulation, and without entering into the details of the associated experimental setups (which we will address in Sect. 3), the principle of the method can be explained as follows, where we distinguish the optical principle from the signal processing algorithm.

2.1 Optical principle

Figure 1 shows the optical setup: the camera and the projector are chosen to be arranged in the parallel–optical-axes geometry, i.e., their optical axis are parallel to each other and separated by a length D. They are perpendicular to the reference plane (Oy), which corresponds to the undeformed surface. In addition, their entrance pupils are located at the same height L[1].

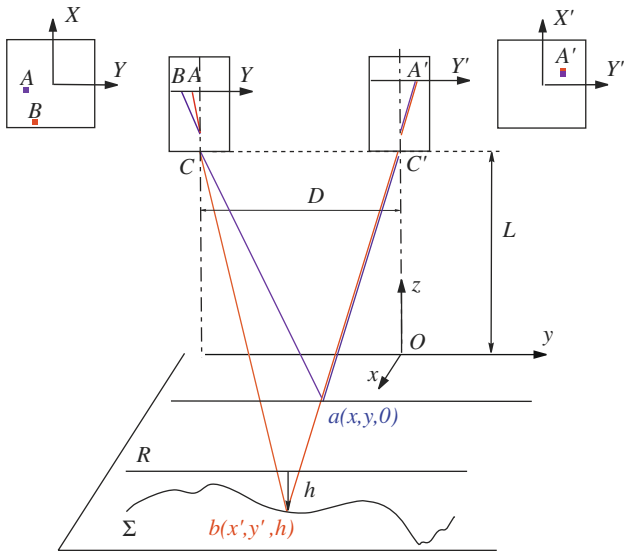


Fig. 1 Optical configuration scheme and ray tracing for the projection and imaging system. Parallel–optical-axes geometry is adopted: both optical axes are coplanar and parallel to each other, separated by a distance D, while the entrance pupils are positioned at the same height, L over the undeformed reference surface. [The point of coordinates (x', y', h) in the figure corresponds to $(x + \delta x, y + \delta y, h)$ in the notation used for the text]

We start from the simple configuration where (Oy) is a reflecting surface. From a periodic pattern with p_p-period on (Y), the projector forms[2] a p-periodic pattern on (Oy), with a magnification $\alpha(p = \alpha p_p, \alpha > 1)$. Then, the pattern on (Oy) is seen by the camera that restitutes a $p_c$periodic pattern on (Y'), with a magnification $\beta(p_c = \beta_p, \beta < 1)$. This two-step process can be described using rays: the ray coming from A on (Y) [with some intensity level, or "phase" $\varphi(A)$] goes to a on (Oy), afterwards it enters the camera reaching (Y') at a point A'. Since the intensity level is conserved along the ray path, the phase at A on the projector, the phase on the undeformed surface at a, and the phase at A' on the camera are equal, i.e., $\varphi_0(A) = \varphi_0(a) = \varphi_0(A')$. The phase on the camera is called φ_0 when the reflecting surface is undeformed (Oy) and φ when the reflective surface is deformed (S). In the latter case, although the reflecting surface does not coincide with (Oy), the same analysis holds but $\varphi(A') \neq \varphi_0(A')$. Indeed, A' is now the image formed by the ray that enters the camera coming from b: $\varphi(A') = \varphi(b)$. The phase at b is the same as the phase of point B on (Y) that differs from A, thus $\varphi(A') = \varphi(b) = \varphi(B)$.

[1] As a matter of fact, these conditions are not necessary but strongly simplify the equations. Moreover, Chan et al. (1994) have showned that the parallel–optical-axes geometry provides a wider range of measurement.

[2] In the case of a transparent liquid, projection onto its free surface is attained by the addition of dye. See Sect. 3.1. for further details.

Measuring the deformed surface implies not only to calculate the height $h(b)$, as usually only done, but also calculating the corresponding position $(x + \delta x, y + \delta y)$ where it is indeed measured (Fig. 1).

Elementary geometrical optics can be used to get (see Takeda and Mutoh 1983; Rajoub et al. 2007; Maurel et al. 2009)

$$h = \frac{\Delta\varphi L}{\Delta\varphi - 2\pi/p\, D}, \tag{1}$$

$$\delta y = \frac{D - y}{L} h, \tag{2}$$

$$\delta x = \frac{x}{L} h, \tag{3}$$

where $\Delta\varphi(Y) \equiv \varphi(Y) - \varphi_0(Y)$. Then the measurement of the height distribution h and the corresponding positions $(x + \delta x, y + \delta y)$ of the deformed surface consists of determining this phase-shift.

Intermediate, but useful relations are the intensities (gray scales) recorded by the camera I_0 and I when the reflecting surfaces are, respectively, (Oy) and (S) and for a sinusoidal fringe pattern (see also Sects. 3.1, 3.4).

$$\begin{aligned} I_0(X,Y) &= \cos(2\pi/p_c Y + \varphi_0(Y)), \quad \varphi_0 = -\frac{2\pi}{p} D \\ I(X,Y) &= \cos(2\pi/p_c Y + \varphi(Y)), \quad \varphi = -\frac{2\pi}{p}\frac{D}{L-h}, \end{aligned} \tag{4}$$

These four last relations are the ones proposed by Takeda et al. (1982) using $f_0 \equiv 2\pi/p$.

2.2 Signal processing

The camera records the intensity signals $I(X, Y)$ and $I_0(X, Y)$. These signals differ from the simplified form given by Eq. 5 mainly because of two sources of unwanted intensity variations. The first consists of illumination inhomogeneities or background variations over the field of view $\mathcal{B}$, and is made evident when no grating pattern is used. In that case, the intensity registered by the camera can therefore be expressed as

$$I^{\text{ref}}(X,Y) = \mathcal{B}(X,Y). \tag{5}$$

These inhomogeneities remain present when the fringe pattern is projected, as well as when the reflecting surface is deformed, as an additive variation. The second source of unwanted intensity variation is typically due to a modulation on the intensity of the projected pattern of fringes. This modulation, corresponding to a local surface reflectively, is denoted $\mathcal{A}$, and remains the same (or almost the same) whatever being the height of the reflecting surface. These result in the general form of the recorded intensities as

$$\begin{aligned} I_0(X,Y) &= \mathcal{A}(X,Y)\cos(2\pi/p_c Y + \varphi_0(Y)) + \mathcal{B}(X,Y), \\ I(X,Y) &= \mathcal{A}(X,Y)\cos(2\pi/p_c Y + \varphi(Y)) + \mathcal{B}(X,Y), \end{aligned} \tag{6}$$

Basically, the signal treatment can be divided in two steps.

Step 1 mainly consists in the suppression of the additive background in both the reference and deformed image, and is given by the following equations:

$$\mathcal{H}(I_0 - I^{\text{ref}}) = \mathcal{A}(X,Y)\exp\{\mathrm{i}(2\pi/p_c Y + \varphi_0(Y))\}, \tag{7}$$

$$\mathcal{H}(I - I^{\text{ref}}) = \mathcal{A}(X,Y)\exp\{\mathrm{i}(2\pi/p_c Y + \varphi(Y))\}, \tag{8}$$

where $\mathcal{H}(F)$ denotes the Hilbert transform of F and i stands for the imaginary unit. It has been assumed that the typical length of variation in $\mathcal{A}$ is large compared to the wavelength p of the projected pattern (in our case, $p = 2$ mm against typical 10 cm variation length for $\mathcal{A}$).

Step 2 allows us to recover the phase shift $\Delta\varphi$ between the two images just by taking the imaginary part of

$$\log\left[\mathcal{H}(I - I^{\text{ref}}) \cdot \mathcal{H}^*(I_0 - I^{\text{ref}})\right] = \log|\mathcal{A}|^2 + \mathrm{i}\Delta\varphi. \tag{9}$$

Hence, these two steps allow to extract $\Delta\varphi(X,Y)$ completely isolated from the background variation $\mathcal{A}(X, Y)$ and the reflectivity $\mathcal{B}(X, Y)$. Then the height distribution h and the associated positions $(y + \delta y)$ are calculated by means of the Eqs. (1) and (2).

3 Experimental setup

In this section, we describe both the experimental setup and the data processing technique employed in the experiments shown in Sect. 4. A discussion on the limitations of the method in terms of maximum range of measurement and resolution is presented as well.

3.1 Optical set-up

The complete experimental setup devised for our high-resolution surface deformation mapping technique is shown schematically in Fig. 2.

A Plexiglas channel with a test section of 1.5 m long, 0.5 m wide and 0.15 m high was built to hold the liquid whose free surface is to be studied.

In our experiments, water is employed as working liquid. In order to be able to project images onto the water surface the liquid's light diffusivity is enhanced by the addition of a white liquid dye (an standard, highly concentrated titanium dioxide pigment paste, commonly used for tinting water-based paints) which does not affect water's hydrodynamical properties. The optimum concentration level was established experimentally as a compromise between diluteness and high fringe contrast.

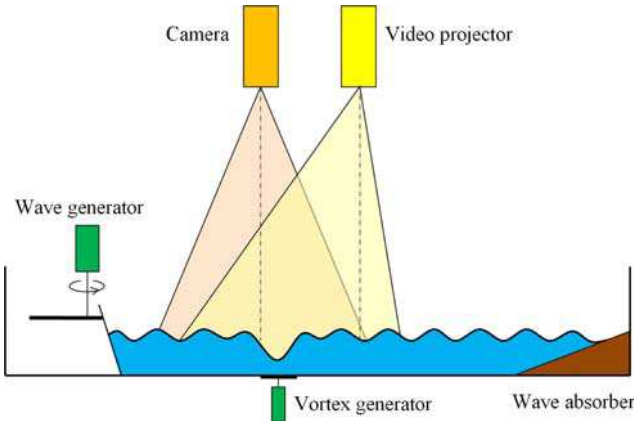


Fig. 2 Complete experimental setup

A concentration of 0.5% v/v, associated with a Michelson luminance contrast exceeding the threshold value of 0.85 was used in our experiments. It should be noted that this concentration value is well below the saturation point of 10% v/v, which assures that phase separation (either in the form of coexisting phases or suspension) cannot occur. Note that dye makes the liquid opaque, thus bulk measurements are possible using acoustical techniques (such as Ultrasonic Doppler Velocimetry) but not optical techniques (Particle Image Velocimetry, Laser Doppler Velocimetry).

Fringe pattern projection onto the free-surface is achieved by means of a computer-controlled digital videoprojector with a high resolution of 1,920 × 1,080 px^2, and 12-bit-depth per color. An important improvement arising from the use of a digital videoprojector is that we are able to project sinusoidal fringe patterns with a controlled wavelength (see Fig. 3). Usually, the projected pattern is a square profile (Ronchi grating), extremely unadapted for Fourier analysis. Indeed, the use of a sinusoidal grating strongly increases the quality of the filtering process as well as the phase recovering. Another important improvement with a videoprojector compared to a slide-projector usually employed is that a videoprojector can project an image on a surface shifted with respect to its axis (see Fig. 2) and hence more centered to the camera axis. The videoprojector allows a correction of the projected image so that the image is not distorted and keeps the fringes' wavelength constant all over the image and maintains the original sharpness. However, due to the fact that the projected pattern varies discretely in space and is digitized in intensity, the video projector's resolution is lower than that of a slide projector.

For a given projection distance, the size of the projected optical field can be adjusted (by means of the projector zoom optics) to cover either a small or a relatively large area of the liquid's surface. In particular, we employed a projection distance of $L = 1$ m, which allowed us to work with projection windows of sizes ranging from approximately 36 × 20 to 80 × 45 cm^2 (covering roughly the channel's width).

The fringe patterns projected onto the liquid's free surface were recorded by a Fujifilm Finepix S2 Pro SRL-type digital still camera, with a 3,024 × 2,016 px^2 CCD and a color depth of 16-bits per color. In order to avoid any artifact from the camera's preprocessing algorithm (such as those coming from quantization, compression, color depth reduction, etc.) we worked with raw images which were later developed into portable pixmap (PPM) format at full color depth.

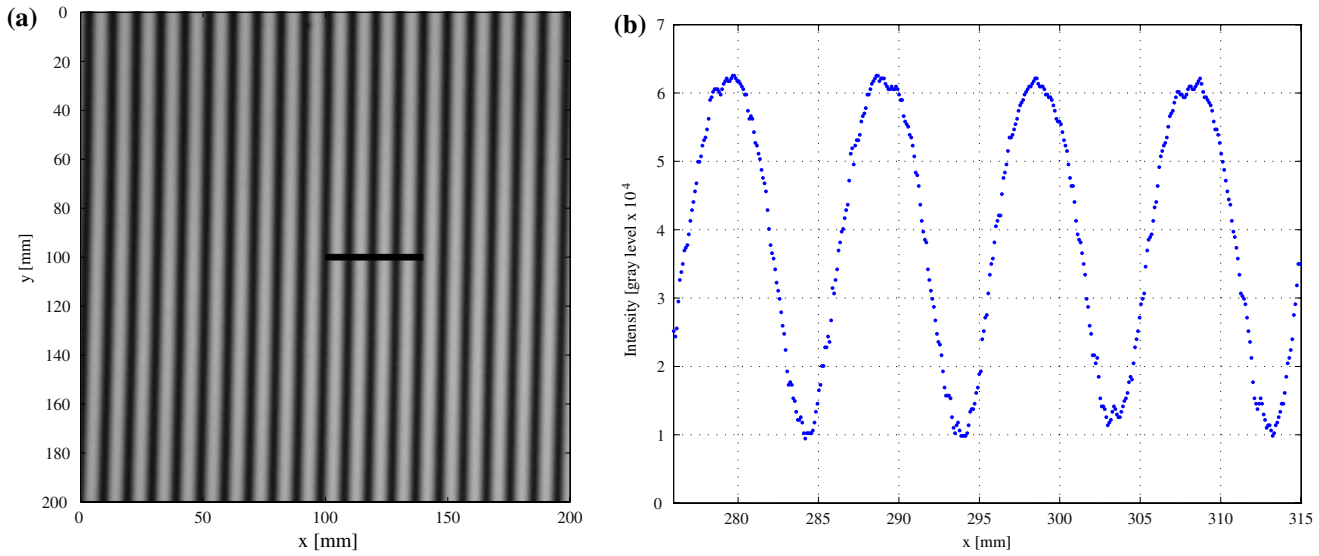


Fig. 3 **a** Sample image of the fringes projected onto an undeformed liquid surface as registered by the camera. **b** Intensity profile along the horizontal segment shown in *black* over the image *a*

The whole fringe projection and image capturing system is held over the channel supported by a mobile structure that allows for precise alignement and repositioning of the optical devices.

3.2 Wave and vortex generators

The channel is further equipped with two mechanisms to produce both global and localized controlled deformation of the liquid's surface (Fig. 2). On one end of the channel, a wave paddle system driven by a motor is employed to create plane sinusoidal surface waves with frequencies and amplitudes ranging from 1–500 Hz to 0.1 to 2 cm, respectively. At the opposite side of the channel, an inclined styrofoam beach of 1:3 slope acts as an absorber, avoiding unwanted surface wave reflections. Localized surface deformation is introduced in the form of a pinned vortex created by a 3 cm diameter rotating disk placed at the bottom of the basin, along the channel's longitudinal centerline. The disk, equipped with four plastic curved blades, is driven by a computer controlled servomotor in direction and speed up to 3,500 rpm.

An example of the free surface deformations that can be introduced by these two mechanisms is illustrated in Fig. 4. In the figure, plane surface waves coming from the left are deformed by the presence of the vortex (located in the center of each figure) and the occurrence of dislocations (Zhang et al. 1994; Vivanco and Melo 2004) on the wavefront is observed. In Sect. 4.2, a sample measurement of the FSD associated with this interaction obtained with the proposed technique is shown and discussed.

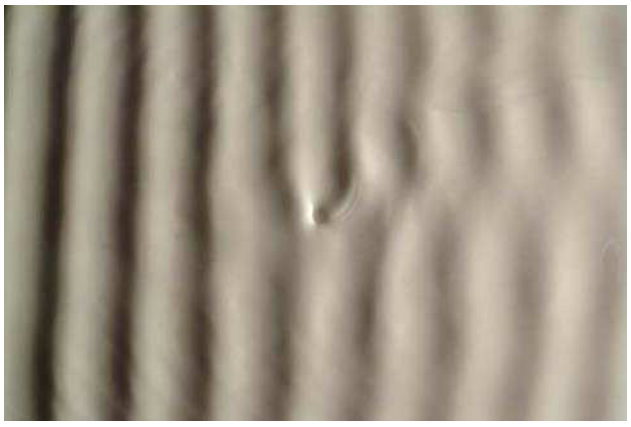


Fig. 4 FSD due to the interaction of the surface waves created by the paddle and the vortex generated by the rotating disk. This visualization has been created using grazing light in order to emphasize the texture of the surface. For reference, the field of view is approximately 50 × 30 cm^2 (Shutter speed 1/4,000 s)

3.3 Signal processing details

We describe in this section the signal processing details employed to accomplish the two steps described in the set of Eqs. (7–9). Step 1 is performed to eliminate the additive deviation $\mathcal{B}$ from I and I_0. Step 2 is then carried out in a procedure that slightly differs from the Hilbert transform described in Sect. 2.2, because the intensity of the projected fringes is not perfectly sinusoidal. Instead, a Fourier transform of $(I_0 - I_{\text{ref}})$ and $(I - I_{\text{ref}})$ is performed. Then each Fourier spectrum is filtered out to extract the ω_c neighbourhood of the frequency $2\pi/p_c$ which contains the height information. For the filtering, a gaussian window of adjustable size centered at that frequency is employed. The phases of the inverse Fourier transforms are then calculated to get $\varphi_0(Y)$ and $\varphi(Y)$. Finally, as the phases are determined modulo 2π, phase unwrapping is needed to obtain the continuous phase-shift over the image. For a comparison of several unwrapping algorithms applied to FTP, the reader is referred to Ghiglia and Pritt (1998) and to the recent reviews by Su and Chen (2004) and Zappa and Busca (2008) and references therein.

It is worth noting that, although FTP theory is based on continuous signals and a continuous Fourier transform, their experimental counterparts are inherently discrete. This induces an error in the recovered phase, particularly relevant for surface deformations of the highest spatial frequencies (e.g., high-frequency waves). However, Chen et al. (1999) have shown that this error can be minimized (as compared to the other experimental uncertainties) by an appropriate choice of the sampling frequency.

3.4 Error and limitations

In this section, we discuss (1) the error on the measured heights and (2) the maximum local slope measurable by this technique.

3.4.1 Uncertainties in the reconstructed height profiles

The relative error on the measured height can be written from Eq. (1)

$$\frac{\Delta h}{h} = \frac{\Delta(\Delta\varphi)}{\Delta\varphi} + \frac{\Delta L}{L} + \frac{\Delta D}{D} + \frac{\Delta p}{p}, \tag{10}$$

where we have used $\Delta\varphi \ll \pi D/p$. The uncertainty on h is therefore determined by the errors in the measured phase as well as those associated with the determination of the geometrical parameters (L, D, p) of the experimental setup. These two sources of uncertainty contribute differently to the final error on Δh, according to their nature. On the one hand, the contribution due to $\Delta\varphi$ is mainly associated with statistical fluctuations such as electronic noise and signal

processing (Fourier transform, filtering). Therefore, it produces a zero mean contribution whose standard deviation is responsible for an irreducible contribution to the uncertainty in h. On the other hand, the systematic errors associated with the determination of the geometrical parameters can be eliminated by calibrating the optical setup.

Calibration prior to laboratory testing can be carried out using any two points of known height. In our case, this was achieved by vertically displacing the reference (plane) surface by a fixed height, although it could also be done using a calibrated surface. Then, the geometrical parameters L and D are adjusted to obtain an optimum agreement between the original and the reconstructed profile.

Once calibrated, the system was tested in laboratory using a triangular prism of known characteristics. Figure 5 shows a superposition of several height profiles measured for the test object (corresponding to different positions on the perpendicular direction), as well as a zoomed view over a 1 mm region of those reconstructed profiles. In the figure, the profiles obtained with our measurement system are also compared to those given by a standard point laser displacement sensor (OptoNCDT 1401-50 by Micro-Epsilon), capable of measuring distances up to 50 mm with a (dynamic) resolution of 25 μm at a 1 kHz sampling rate. The residual fluctuations in this figure, with an amplitude of $\Delta h \sim 0.2$ mm, give the precision of our method, i.e., the minimum height difference the method is able to detect for this interrogation area. Note that the 0.2 mm corresponds as well to the size of the projected pixel and thus appears as a reasonable technical limitation.

3.4.2 *Typical length of variation of the measured height*

There exists a limitation in the maximum slope this method is able to measure. This is because a sharper profile gives a larger Fourier spectrum (a limit being a delta function in the physical space that gives a constant Fourier transform). Thus, the error coming from the filtering increases when the slope of the profile increases. Although the filtering algorithm could be improved, a limitation exists given by the physical size of the projected pixels.

In order to estimate the error associated with the filtering process, we have conducted a numerical test on our data processing algorithm. For that, a gaussian-shaped height profile given by $h(y) = \exp\{y^2/s^2\}$ was chosen, which physically represents a localized deformation of width s on the surface under study. A projected fringe pattern of wavelength p was assumed and, using Eqs. (1–4), two synthetical images I_0 and I, corresponding respectively to the reference (plane) and deformed surfaces, were generated. It is worth noting that electronic noise present in the experiments was not considered in this study.

These two images were then processed by our algorithm (as described in Sect. 3.3), using a unitary gaussian filter of size σ_f centered at the projection (spatial) frequency $k_c = 2\pi/p_c$, ultimately leading to a reconstructed height profile h_r. Finally, the relative error in the reconstruction imposed by the filtering process, defined as $\varepsilon \equiv \sum |h_r - h| / \sum |h|$, was calculated. This process was then repeated for different widths of the filter window σ_f/k_c, and for varying s/p ratios.

Figure 6a illustrates the dependence of ε on the ratio s/p, for three particular values of σ_f/k_c, namely: 1/6, 1/3 and

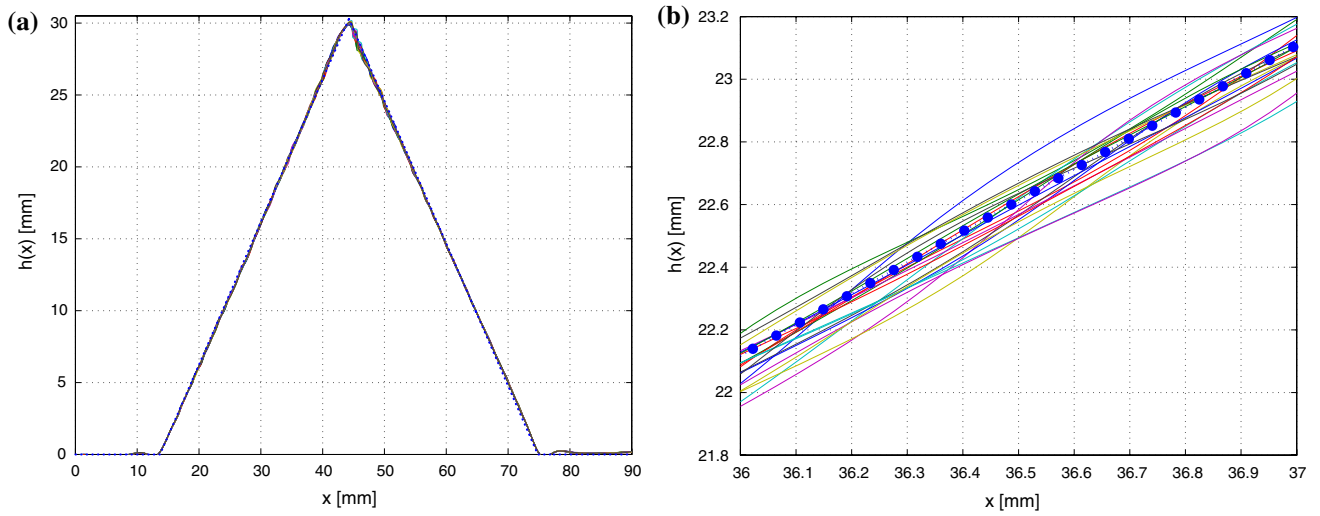


Fig. 5 **a** Several height profiles measured for the triangular prism used for laboratory testing. **b** Zoom over a portion of the reconstructed profiles showing the precision of the method. In both cases, *dots* indicate the object's profile measured by a 25-μm resolution (point) laser displacement sensor, whereas continuous lines denote reconstructed profiles. Note that the weak fluctuations (of peak amplitude lower than 0.2 mm) observable at the flat regions next to the triangular profile are due to the abrupt change in slope, a feature which is not present in the case of most liquid surfaces

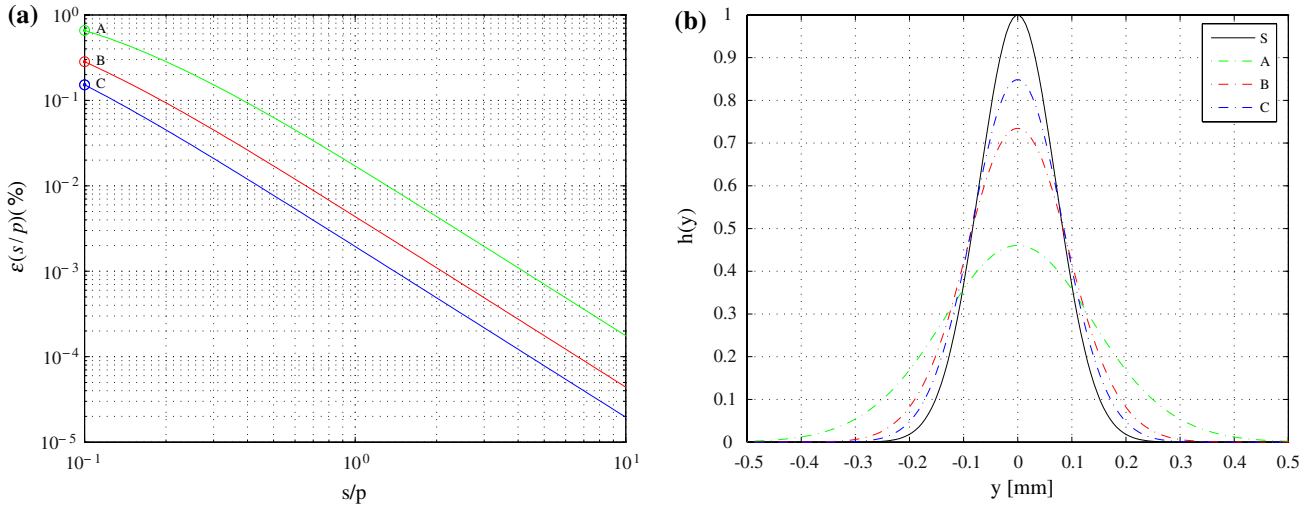


Fig. 6 Error associated to the data filtering and processing algorithm. **a** shows the error ε (as defined in the text) as a function of the dimensionless space variable defined as the ratio of the filter size to the period of the projected pattern. Each of the three curves shown corresponds to a particular value of the filter width (1/6, 1/3 and $1/2 \times 2\pi/p_c$ for the upper, middle and lower curves, respectively). **b** Shows three reconstructed profiles corresponding to the same value $s/p = 10^{-1}$ over each curve in the **a**, compared to the original gaussian profile (shown in *black*). *Color* correspondence between curves in both panels has been conserved for reference purposes. Note that **b** shows a bad-case scenario to illustrate the influence of the filter width on the quality of the reconstruction; however, in practice, a set of parameters ensuring an error less than 10^{-4} % was used

1/2 (upper, middle and lower curves, respectively). This figure shows that the relative error effectively depends on the size of the filter window, assuming values lower than 10^{-2} for $s/p > 1$ and $\sigma_f/k_c > 1/6$ (typically, $1/3 \times 2\pi/p_c$ is used for the illustrative examples shown in Sect. 4). For a fixed value of the ratio $s/p = 0.1$, Fig. 6b shows three reconstructed profiles corresponding to points A, B and C in Fig. 6a, compared to the original gaussian-shaped profile S. Note that in this case, we have chosen a bad-case scenario (in which the characteristic width of the deformation is ten times smaller than the projected pattern's wavelength) in order to be able to show differences between the original and the reconstructed profiles. For $s/p \leq 1$, however, these deviations from the original profile S are not discernible at the figure's resolution ($\varepsilon \leq 10^{-2}\%$).

4 Some illustrative applications

In this section, the performance of the developed measuring system and analysis technique is illustrated with two experimental examples, showing its potential applicability to a vast variety of free-surface flows.

All the examples shown in this section have been measured using a projection distance $L = 1$ m, a projector–camera distance $D = 0.1$ m (thus, $L/D = 10$) and a fringe pattern of wavelength $p = 2$ mm. The shutter speed value employed in all cases is 1/4,000 s.

4.1 Spiral surface waves emitted by a vortex

The first example of application of this technique to free-surface flow measurements in our experimental set-up is devoted to the non-stationary emission of spiral surface waves from a vortex core. For a 3.5-cm depth liquid layer and a relatively high rotating speed (400 rpm) of the disk, a strong and fixed vertical vortex is created which, in addition, ocassionally emits weak amplitude spiral surface waves. These surface waves are barely noticeable to the naked eye. We present what is, to our knowledge, the first reported measurement of spiral waves emitted by a vortex available in the literature.

Figure 7 shows a sample free-surface reconstruction for the case of spiral waves emitted by a vortex obtained using the proposed technique. Note that this technique allows for the measurement of both the deep vortex core and the weak spiral waves over an interrogation area of size 30×45 cm^2. Although the wave amplitude is weak even near the source in comparison to the vortex core (25 mm in depth), the figure shows that the technique is able to detect and reconstruct remarkably well waves of amplitudes down to 0.2 mm. It is worth noting that this technique can discern perturbations of amplitudes throughout more than two orders of magnitude in a single shot measurement.

Qualitatively, similar spiral waves were theoretically predicted by Umeki and Lund (1997) in the shallow water regime and for penetrable boundary conditions at the vortex core. Moreover, Vivanco and Melo (2000) has

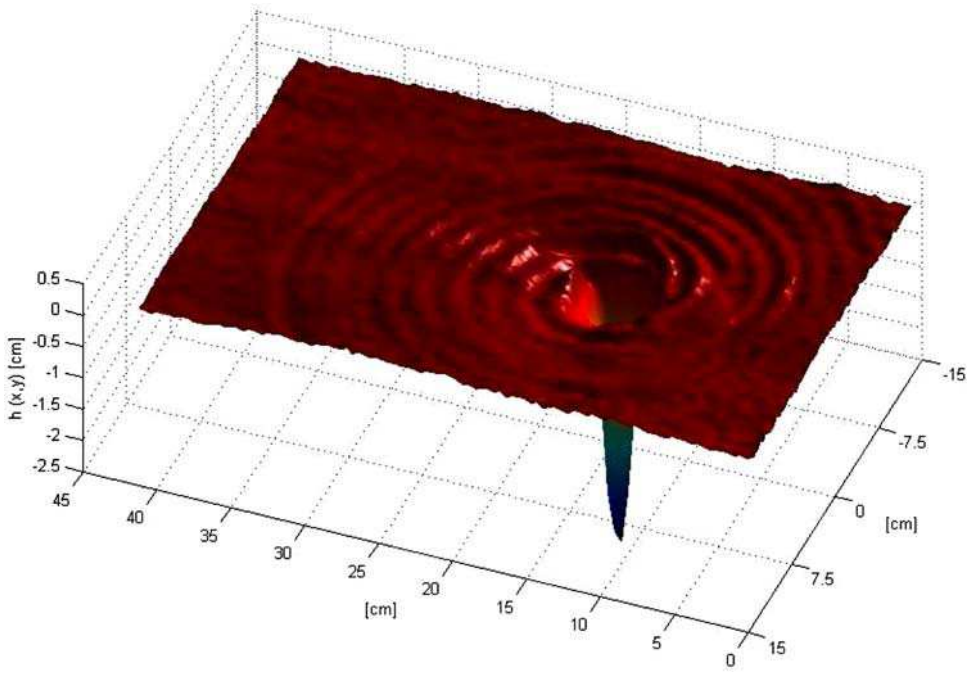


Fig. 7 Free surface deformations measured with the proposed technique, showing a set of spiral waves emitted by a vortex. Note the different height scales the method is able to discern: the vortex core is 25 mm in depth while the detectable amplitude for the spiral waves on the surface goes down to 0.2 mm. The overall interrogation area is 30×45 cm^2 in size

visualised spiral waves in an comparable experimental situation where they appear to be the natural solutions for a plane surface waves background flow in the presence of a vortex. An experimental study on these spiral waves is currently progress.

4.2 Vortex–surface–wave interaction

Free surface deformation due to water waves–vortex interaction is the subject of the second example of application shown in this section. The interest on the experimental study of such interactions is many fold. For instance, and from a fundamental point of view, Berry et al. (1980) have shown that wave–vortex interactions constitute an analogue in the frame of classical mechanics of the Aharonov–Bohm effect (Aharonov and Bohm 1959), in which the dynamics of a charged quantum particle is affected by the vector potential even in regions where the associated field vanishes. As opposed to the quantum case, the wavefront dislocations arising from the interaction are physically measurable. A detailed theoretical and numerical study of the scattering of dislocated wavefronts by vorticity structures and its relation with the Aharonov–Bohm effect was presented by Coste et al. (1999) and Coste and Lund (1999) for shallow water and dispersive waves, respectively.

Figure 8a shows a typical FSD field produced by the strong interaction between plane surface waves and a vortex as measured with the present technique. As in Fig. 4, incident waves propagate from left to right, impinging on the counterclockwise-rotating vortex and giving rise to strong deformations in the wavefronts. In this case, the depth of the liquid layer was set to 3 cm, and the disk rotates at 200 rpm. The associated vortex core is approximately 5 mm in depth, and the incident waves are characterized by a wavelength $\lambda \approx 6$ cm. The interrogation area over the surface is roughly 30×40 cm^2.

Both Fig. 8a and b show the same reconstructed FSD, only the range of the color palette is dilated in the latter to heights in the region [1.3] mm to emphasize the difference between hills and valleys, demonstrating the occurrence of dislocations in the wavefront.

A detailed study on the free surface deformations due to the interaction of water waves and a vertical vortex using this topographic technique is already underway and will be the subject of a following publication.

5 Concluding remarks

In order to accurately measure global time-evolving free-surface deformations we have adapted and strongly improved a measuring system and data processing technique based on FTP to the case of a liquid surface. The overall performance of the technique and the quality of the reconstruction have been greatly enhanced by the ability to project high-resolution sinusoidal fringe patterns (instead of using a Ronchi grating) controlled in wavelength. Careful reconstruction of the free-surface deformations was attained by considering the set of equations for h, δy and δx (corrections due to the last two equations being rarely taken into account in the literature).

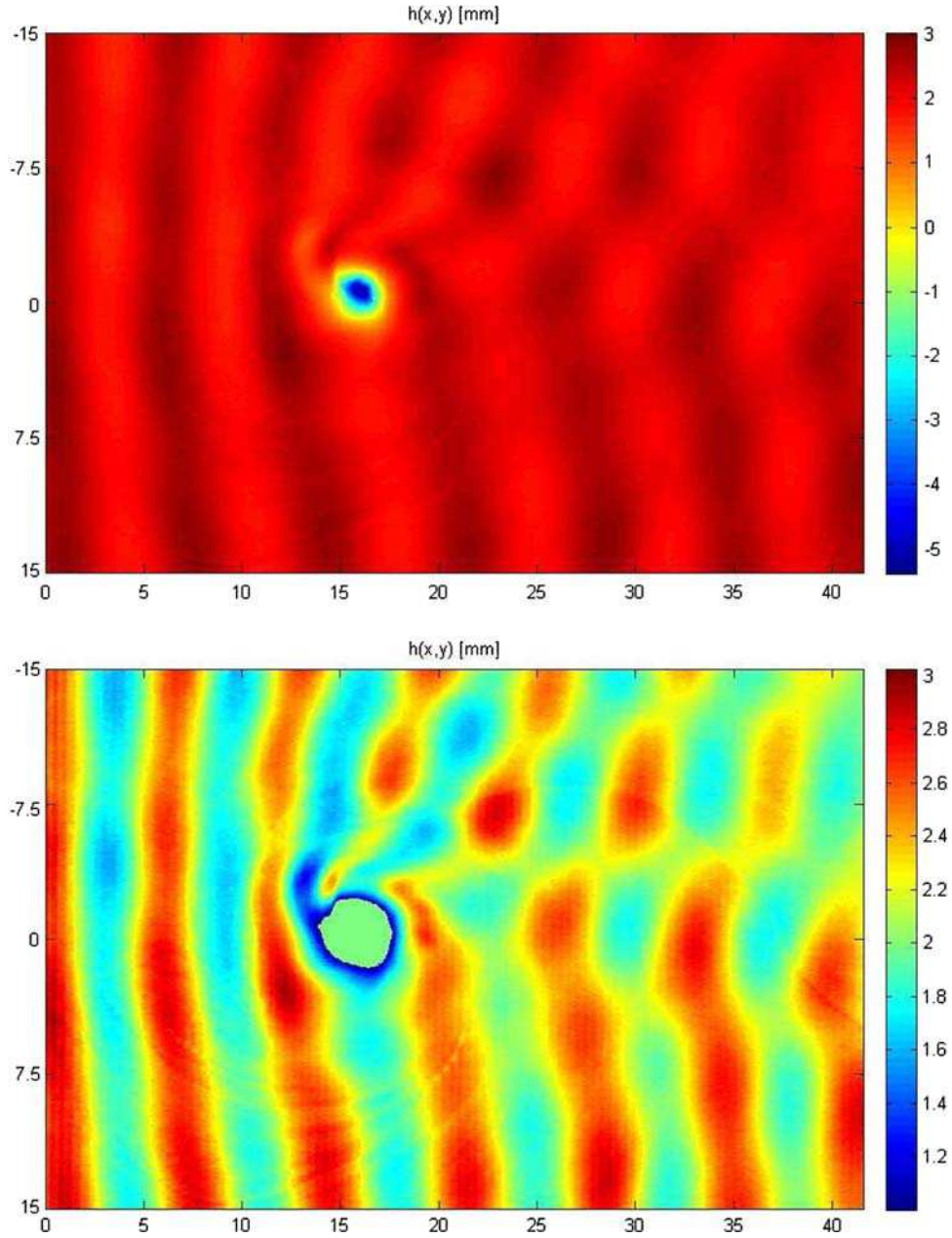


Fig. 8 FSD measured for the water wave–vortex interaction

This experimental system is capable of measuring small perturbations over a large area; e.g., heights in the range from 0.2 to 100 mm, with a 0.2 mm vertical resolution over an interrogation window of 450 × 300 mm^2 sampled with an spatial resolution of 0.1 mm. As mentioned in Sect. 3.4, this absolute vertical resolution corresponds to the size of the projected pixel and thus depends, for a given projector's resolution, on the size of the sampled window over the surface under study.

It has the additional advantage of being easily scalable, so that it can be adapted for a specific application, ranging from small or medium scale laboratory experiments to large applications such as those considered in hydraulic engineering.

Finally, the application examples presented in this work demonstrate the large scope of applicability of this technique, which we believe constitutes a very useful and efficient tool to measure free-surface deformations on a vast variety of fluid dynamics' scenarios.

References

Aharonov Y, Bohm D (1959) Significance of electromagnetic potentials in the quantum theory. Phys Rev 115:485–491. doi: 10.1103/PhysRev.115.485

Benetazzo A (2006) Measurements of short water waves using stereo matched image sequences. Coast Eng 53:1013–1032

Berry MV, Chambers RG, Large MD, Upstill C, Walmsley JC (1980) Wavefront dislocations in the Aharonov–Bohm effect and its water wave analogue. Eur J Phys 1:154–162

Chan P-H, Bryanston-Cross PJ, Judge TR (1994) Studies of Fourier transform profilometry. In: Moorhead RJ, Silver DE, Uselton SP (eds) Proceedings of SPIE, visual data exploration and analysis, vol 2178, pp 165–176

Chen W, Hu Y, Su X, Tan S (1999) Error caused by sampling in Fourier transform profilometry. Opt Eng 38:1029–1034

Cochard S, Ancey C (2008) Tracking the free surface of time-dependent flows: image processing for the dam-break problem. Exp Fluids 44:59–71

Coste C, Lund F (1999) Scattering of dislocated wave fronts by vertical vorticity and the Aharonov–Bohm effect. II. Dispersive waves. Phys Rev E 60:4917–4925. doi:10.1103/PhysRevE.60.4917

Coste C, Lund F, Umeki M (1999) Scattering of dislocated wave fronts by vertical vorticity and the Aharonov–Bohm effect. I. Shallow water. Phys Rev E 60:4908–4916. doi:10.1103/PhysRevE.60.4908

Cox CS (1958) Measurement of slopes of high-frequency wind waves. J Mar Res 16(9):199–225

Dabiri D (2003) On the interaction of a vertical shear layer with a free surface. J Fluid Mech 480:217–232

Dabiri D, Gharib M (2001) Simultaneous free-surface deformation and near-surface velocity measurements. Exp Fluids 30:381–390

Gharib M (1994) Some aspects of near surface vortices. Appl Mech Rev 47:157–162

Gharib M, Weigand A (1996) Experimental studies of vortex disconnection and connection at a free surface. J Fluid Mech 321:59–86

Ghiglia DC, Pritt MD (1998) Two-dimensional phase unwrapping: theory, algorithms and software. Wiley, New York

Grant I, Stewart N, Padilla-Perez IA (1990) Topographical measurements of water waves using the projection moire method. Appl Opt 29:3981–3983

Maurel A, Cobelli P, Pagneux V, Petitjeans P (2009) Experimental and theoretical inspection of the phase-to-height relation in Fourier transform profilometry. Appl Opt 48(2):380–392. doi:10.1364/AO.48.000380

Moisy F, Rabaud M, Salsac K (2008) Measurement by digital image correlation of the topography of a liquid surface. Exp Fluids (submitted)

Patorski K (1993) Handbook of the Moire fringe technique. Elsevier, Amsterdam

Rajoub BA, Lalor MJ, Burton DR, Karout SA (2007) A new model for measuring object shape using non-collimated fringe-pattern projections. J Opt A Pure Appl Opt 9:66. doi:10.1088/1464-4258/9/6/S10

Ruban VP (2000) Interaction of a vortex ring with the free surface of an ideal fluid. Phys Rev E 62:4950–4958. doi:10.1103/PhysRevE.62.4950

Savelsberg R, van de Water W (2008) Turbulence of a free surface. Phys Rev Lett 100(3):034501. doi:10.1103/PhysRevLett.100.034501

Savelsberg R, Holten A, van de Water W (2006) Measurement of the gradient field of a turbulent free surface. Exp Fluids 41:629–640. doi:10.1007/s00348-006-0186-x

Su X, Chen W (2001) Fourier transform profilometry: a review. Opt Lasers Eng 35:263–284

Su X, Chen W (2004) Reliability-guided phase unwrapping algorithm: a review. Opt Lasers Eng 42:245–261

Takeda M, Mutoh K (1983) Fourier transform profilometry for the automatic measurement of 3-D object shapes. Appl Opt 22:3977–3982

Takeda M, Ina H, Kobayashi S (1982) Fourier-transform method of fringe-pattern analysis for computer-based topography and interferometry. J Opt Soc Am (1917–1983) 72:156

Tsubaki R, Fujita I (2005) Stereoscopic measurement of a fluctuating free surface with discontinuities. Meas Sci Technol 16:1894–1902. doi:10.1088/0957-0233/16/10/003

Umeki M, Lund F (1997) Spirals and dislocations in wave–vortex systems. Fluid Dyn Res 21:201–210

Vivanco F, Melo F (2000) Surface spiral waves in a filamentary vortex. Phys Rev Lett 85:2116–2119. doi:10.1103/PhysRevLett.85.2116

Vivanco F, Melo F (2004) Experimental study of surface waves scattering by a single vortex and a vortex dipole. Phys Rev E 69(2):026307. doi:10.1103/PhysRevE.69.026307

Walker DT, Chen C-Y, Willmarth WW (2006) Turbulent structure in free-surface jet flows. J Fluid Mech 91:223. doi:10.1017/S0022112095002680

Wright WB, Budakian R, Putterman SJ (1996) Diffusing light photography of fully developed isotropic ripple turbulence. Phys Rev Lett 76:4528–4531. doi:10.1103/PhysRevLett.76.4528

Wright WB, Budakian R, Pine DJ, Putterman SJ (1997) Imaging of Intermittency in ripple-wave turbulence. Science 278:1609

Zappa E, Busca G (2008) Comparison of eight unwrapping algorithms applied to Fourier-transform profilometry. Opt Lasers Eng 46:106–116

Zhang X (1996) An algorithm for calculating water surface elevations from surface gradient image data. Exp Fluids 21:43–48

Zhang X, Cox CS (1994) Measuring the two-dimensional structure of a wavy water surface optically: a surface gradient detector. Exp Fluids 17:225–237. doi:10.1007/BF00203041

Zhang Q-C, Su X-Y (2002) An optical measurement of vortex shape at a free surface. Opt Laser Technol 34:107–113

Zhang X, Dabiri D, Gharib M (1994) A novel technique for free-surface elevation mapping. Phys Fluids 6(9):S11–S11

Zhang X, Dabiri D, Gharib M (1996) Optical mapping of fluid density interfaces: concepts and implementations. Rev Sci Instrum 67:1858–1868

CHAPTER 3

EXPERIMENTAL AND THEORETICAL INSPECTION OF THE PHASE-TO-HEIGHT RELATION IN FOURIER TRANSFORM PROFILOMETRY

This chapter is composed by an article published in *Applied Optics* [64]. This article is of a more technical nature than the one described in the precedent chapter, although they both serve the common purpose of describing the details of our optical profilometric technique.

In general, the procedure by which profilometric techniques based on fringe projection achieve the reconstruction of the surface topography can be divided in four steps. The first one regards the projection of a structured light pattern (using either collimated or non-collimated projections) onto the surface under study and the capture of the light intensity variations of the projected pattern by a camera. The topography of the surface introduces a frequency modulation in the observed pattern, which is also modified by the perspective due to the relative positioning and orientation of the projection–recording system. The second step consists in demodulating the registered pattern in order to obtain a phase map of the surface depicting, at every sampled point, the relative phase between deformed and reference patterns. The level of complexity involved in the determination of this phase map strongly depends on the type of fringe projection technique employed. For instance, in the case of the phase-shifting methods (such as the phase-stepping or integrating-bucket techniques), where the fringe pattern is phase stepped a known amount between intensity measurements, the phase map is simply obtained by an algebraic combination of several deformed patterns taken at the same surface state (see, for example, Ref. [81]). Unfortunately, from an experimental standpoint, the price paid to take profit from this computational advantage is prohibitively high, as the projection–recording system has to be able to precisely shift the projected pattern and capture the corresponding deformed images before the surface state changes significantly, rendering it almost impracticable for the measurement of time-dependent free-surface deformation fields. In contrast, our profilometric technique requires only one image to be taken (besides the reference image, of course) in order to obtain the surface phase map, which is demodulated from each deformed fringe pattern by filtering in Fourier space. However, a common point to all fringe projection techniques, arising from the fact that they are intrinsically demodulating tech-

niques, is that the resulting phase map is calculated modulo π (the phase is said to be 'wrapped around'). As a consequence, the phase map often presents spurious discontinuities corresponding to phase jumps and other ambiguities. Therefore, the third step in the surface reconstruction process involves the so-called 'phase unwrapping', a complex problem whose study has evolved and grown to become a domain of its own. Once unwrapped, the last remaining step consists in relating the phase map to the surface height, through an equation often termed 'phase-to-height relation', derived by considering the particular geometry employed for the projection–capturing system (collimated or non-collimated projection, parallel- or crossed-optical-axes).

This chapter focuses on the last link in this chain of processes, particularly in the derivation of the phase-to-height conversion relation. The usually cited relation for the case of non-collimated projection is due to Takeda and Mutoh [97]. Recently, in a very didactic paper, Rajoub et al. [85] showed that this reference relation given by Takeda and Mutoh is erroneous. The experimental and theoretical studies presented in this chapter follow from Rajoub's study. The results obtained for the phase concern both collimated and non-collimated projectios for both parallel- and crossed-optical-axes geometries, and agree with Rajoub's findings. Moreover, experimental evidence of the error in Takeda and Mutoh's formula is shown and the origin of the error in Takeda and Mutoh's derivation is explained. Incidentally, it is shown that Rajoub et al.'s argument regarding Takeda and Mutoh's error is not correct.

Two additional results arising from this work concern the derivation of the varying fringe spacing in the crossed-optical-axes configuration and the derivation of the phase-to-height relation for collimated projection in the parallel-optical-axes geometry. Both derivations have also been successfully validated experimentally within the framework of this study.

In the past ten years, the need for performing accurate non-contact measurements has motivated studies on signal processing, such as phase unwrapping algorithms and filtering techniques, in the aim of enhancing the quality of the reconstruction provided by fringe projection profilometry methods. Among these efforts, the contribution made in this study provides for an exact (within the paraxial approximation of geometrical optics) and experimentally validated phase-to-height relation which constitutes a solid departure point to any further improvement and refinement of the technique.

Experimental and theoretical inspection of the phase-to-height relation in Fourier transform profilometry

Agnès Maurel,[1,*] Pablo Cobelli,[2] Vincent Pagneux,[3] and Philippe Petitjeans[2]

[1]Laboratoire Ondes et Acoustique, UMR CNRS 7587, Ecole Supérieure de Physique et Chimie Industrielles, 10 rue Vauquelin, 75005 Paris, France

[2]Laboratoire de Physique et Mécanique des Milieux Hétérogènes, UMR CNRS 7636, Ecole Supérieure de Physique et Chimie Industrielles, 10 rue Vauquelin, 75005 Paris, France

[3]Laboratoire d'Acoustique de l'Université du Maine, UMR CNRS 6613, Avenue Olivier Messiaen, 72085 Le Mans Cedex 9, France

*Corresponding author: agnes.maurel@espci.fr

Received 11 September 2008; revised 28 October 2008; accepted 29 October 2008; posted 18 November 2008 (Doc. ID 100987); published 8 January 2009

The measurement of an object's shape using projected fringe patterns needs a relation between the measured phase and the object's height. Among various methods, the Fourier transform profilometry proposed by Takeda and Mutoh [Appl. Opt. **22**, 3977–3982 (1983)] is widely used in the literature. Rajoub *et al.* have shown that the reference relation given by Takeda is erroneous [J. Opt. A. Pure Appl. Opt. **9**, 66–75 (2007)]. This paper follows from Rajoub's study. Our results for the phase agree with Rajoub's results for both parallel- and crossed-optical-axes geometries and for either collimated or noncollimated projection. Our two main results are: (i) we show experimental evidence of the error in Takeda's formula and (ii) we explain the error in Takeda's derivation and we show that Rajoub's argument concerning Takeda's error is not correct. © 2009 Optical Society of America

OCIS codes: 080.0080, 120.2650.

1. Introduction

The Fourier transform profilometry proposed by Takeda *et al.* in the 80s [1,2] has achieved great success and is now one of the reference techniques for three-dimensional (3D) shape measurement [3–14] (see also a review in [15]). This method uses noncollimated projections of a structured light pattern onto an object (for a review on structured lighting techniques, see [16,17]). The intensity variations of the projected pattern are captured by a camera; afterward, a conversion of the measured phase to the object height is needed. The usually cited phase-to-height relation for noncollimated projection is from Takeda and Mutoh [2] (both in the parallel- and in the crossed-optical-axes geometries):

$$h(y) = \frac{L\Delta\varphi(y)}{\Delta\varphi(y) - \omega_0 D}, \tag{1.1}$$

where y is the coordinate in the field of view of the camera (see Fig. 1). In that relation, $\Delta\varphi(y)$ is the phase difference when the camera captures the intensity variations over a reference plane and over the surface of a two-dimensional (2D) object (the x direction is not considered) whose height h has to be determined. D is the distance between the projector and the camera and $\omega_0 \equiv \omega_p \cos\theta/G_p$, with ω_p as the frequency of the fringes on the projector's grating and G_p as the magnification factor of the projector (ω_0 is the frequency of the fringes on the projector

0003-6935/09/020380-13$15.00/0
© 2009 Optical Society of America

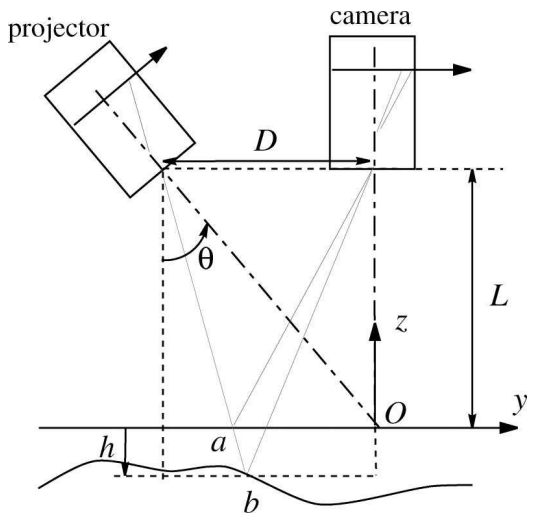


Fig. 1. Reproduction of Takeda's representation in crossed-optical-axes geometry. A fringe pattern is projected onto a reference surface (as point a) and on a deformed surface (point b). The corresponding phase variation in the intensity recorded by the camera is $\Delta\varphi(y)$ (2D object analysis is presented in Takeda's paper [2]).

image plane). Also, the derivation is performed assuming the camera and the projector that produces the intensity variations are at the same distance L from the reference plane.

In a very didactic paper, Rajoub *et al.* [17] have shown that this relation is incorrect. These authors propose a complete calculation relaxing the hypothesis that the camera and the projector are at the same distance from the reference plane. They propose an explanation of the error in Takeda's formula, which they attribute to an unjustified hypothesis of collimated projection. Also, in a previous paper [16], the same authors have derived the phase-to-height relation for collimated projection. Incidentally, note that these authors propose a relation between the height of the object h and the phase φ stored by the camera when capturing the intensity variations over the object surface, instead of using the usual phase difference $\Delta\varphi$.

Our paper follows from Rajoub's study. Our derivations concern both collimated and noncollimated projection for parallel- and crossed-optical-axes geometries. When we assume that the camera and the projector are at the same distance L from the reference plane, we find,

– for noncollimated projection in parallel-optical-axes geometry,

$$h(x',y') = \frac{L\Delta\varphi}{\Delta\varphi - \omega_0 D}, \tag{1.2}$$

where

$$x' = x - \frac{h}{L}x, \qquad y' = y - \frac{h}{L}y; \tag{1.3}$$

– for noncollimated projection in crossed-optical-axes geometry,

$$h(x',y') = \frac{L\Delta\varphi(1+\sin^2\theta y/D)^2}{\Delta\varphi(1+\sin^2\theta y/D)[1-\sin^2\theta(1-y/D)] - \omega_0 D}; \tag{1.4}$$

– for collimated projection in parallel-optical-axes geometry,

$$h(x',y') = -\frac{L\Delta\varphi}{\omega_0 y}; \tag{1.5}$$

– for collimated projection in crossed-optical-axes geometry,

$$h(x',y') = \frac{L\Delta\varphi}{\omega\sin\theta(L-\cot\theta y)}. \tag{1.6}$$

In the above expressions, $\Delta\varphi$ stands for $\Delta\varphi(X',Y')$ or $\Delta\varphi(x,y)$, with (X',Y') and (x,y) being, respectively, the coordinates in the image plane of the camera and the coordinates in the field of view of the camera (thus $X' = -G_c x$ and $Y' = -G_c y$, with G_c the magnification factor of the camera).

Throughout this paper, we will compare our expressions in Eqs. (1.2), (1.3), (1.4), (1.5), and (1.6) with the expressions existing in the literature.

In this paper, we show experimental measurements performed using a calibrated object only in the case of noncollimated projection (Section 3). Our phase-to-height relations in Eqs. (1.2) and (1.4), together with Eq. (1.3), are shown to give a good determination of the object shape and the errors due to the use of Takeda's relation [Eq. (1.1)] are exemplified and discussed (Section 4).

The main contribution of our paper concerns noncollimated projection (as a consequence, the calculations concerning collimated projection are collected in Appendix B). On the one hand, we give a more tractable phase-to-height relation than that in [17], useful for direct application to real experiments. Notably, our Eqs. (1.2), (1.3), and (1.4) concern the phase difference $\Delta\varphi$ (instead of the absolute phase φ in [16,17]) that is known to compensate unwanted defects in the projection process [2]. In addition, we give experimental evidence of the validity of our expressions. On the other hand, we show that the error in Takeda's result is due to an erroneous manipulation of the phases φ (for projection on to the object) and φ_0 (for projection on to the reference plane). Otherwise, Takeda's calculations are correct. Our conclusion differs from Rajoub's argument, which implies an erroneous use of collimated projection.

Incidentally, some new results in our paper concern: the derivation of the varying fringe spacing in the crossed-optical-axes configuration and the derivation of the phase-to-height relation for collimated projection in the parallel-optical-axes geometry.

The paper is organized as follows: in Section 2, the phase-to-height relations are derived for

noncollimated projection. The cases of the parallel- and the crossed-optical-axes geometries are then considered as particular cases of this general result. The comparison with Takeda's relation is presented. Section 3 exemplifies our results with experimental data collected both in the parallel- and crossed-optical-axes configurations. A discussion on the obtained phases φ_0 and φ is presented, notably, the change in the fringe spacing in the crossed-optical-axes geometry (see also Appendix A). In Section 4, the derivation performed in Ref. [2] is analyzed and the error that leads to Eq. (1.1) is demonstrated. Finally, we collect in two appendices the derivation of the fringe spacing in the crossed-optical-axes geometry for noncollimated projection (Appendix A) and the derivation of the phase-to-height relations for collimated projection (Appendix B).

2. Derivation of the Phase-to-Height Relations

We consider the configuration of Fig. 2. With the only exception of this section, all the results presented in this paper concern the usual configuration, where the projector and the camera are at the same distance from the reference plane R (thus $L_p = L_c$).

In the following, we define the magnification factors for the projector G_p and for the camera G_c as for simple lenses with respective focal lengths f_p and f_c (positive magnification factors are considered, it being known that images through lenses are inverted): $G_p = L_p/(\cos\theta f_p)$ and $G_c = f_c/L_c$.

We also define ω_p as the fringe frequency in projector's grating (XY plane), $\omega = \omega_p/G_p$ as the fringe frequency in the image plane of the projector (I plane), and $\omega_c \equiv \omega/G_c$. We denote Σ as the surface whose height $h(x,y)$ with respect to the reference surface R is measured.

The image captured by the camera on the $(X'Y')$ plane is a pattern of gray levels corresponding to intensity variation $I(X',Y')$:

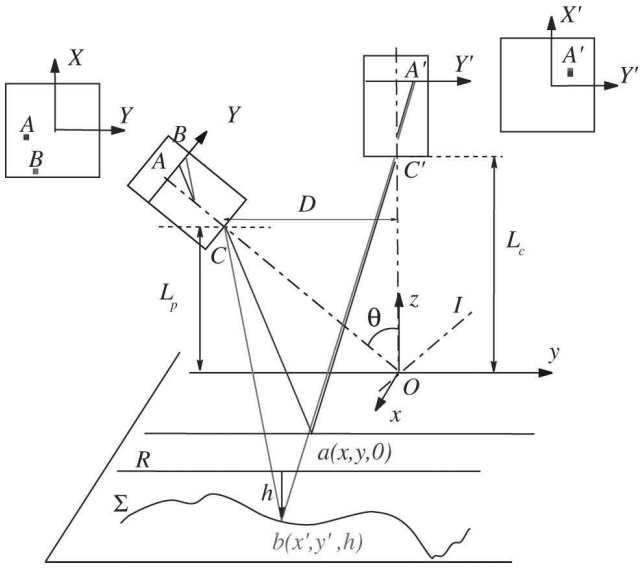


Fig. 2. Optical setup.

$$I(X',Y') = 1 + \cos\varphi(X',Y'). \tag{2.1}$$

When the fringes are projected onto the reference plane R, the intensity, or gray level, observed at point $A'(X',Y')$ is due to the ray $A\alpha A'$, whose intensity is imposed by the intensity at the point A on the projector grating. Assuming a sinusoidal fringe projection (with the fringes oriented along the X axis), we have

$$\varphi_0(X',Y') = \omega_p Y_A. \tag{2.2}$$

For any reflecting surface Σ different from R, the intensity observed at point A' changes, because the ray arriving at A' is now the ray BbA'. This ray holds the intensity of the point B on the projector grating. Thus,

$$\varphi(X',Y') = \omega_p Y_B. \tag{2.3}$$

By definition, the phase difference $\Delta\varphi(X',Y') \equiv \varphi(X',Y') - \varphi_0(X',Y')$ is a measure of the change in intensity observed on A'.

Thus, the task is to determine the geometric relations between (X',Y') on the camera grating and Y_A or Y_B on the projector grating. The derivation is performed in the case of the ray BbA', propagating from $B(X,Y)$ to $b(x',y',h)$ on any surface Σ and arriving at $A'(X',Y')$ to produce the phase $\varphi(X',Y')$. Then, $\varphi_0(X',Y')$ is deduced for R, being the reflecting surface (thus, $h = 0$).

To do that, we use the following geometric relations. On Fig. 3, we project, along the Ox axis in the plane $x = 0$, the rays Cb and bC' to produce Cb_0 and b_0C' with $b_0 = (0,y',h)$. The angles α and β measure, respectively, the angles $(\widehat{OCb_0})$ and $(\widehat{OC'b_0})$ in the plane $x = 0$. The angle $\theta = (\widehat{cCO})$ measures the inclination of the projector's axis with respect to the camera's axis.

Then, the angle α measures the position of the point B on the projector grating: $\tan\alpha = -Y_B/f_p$. On the other hand, in the triangle Ccb_0, we have $\tan(\theta+\alpha) = (D+y')/(L_p - h)$. We get

$$\tan\alpha = -\frac{Y_B}{f_p} = \frac{(D+y') - \tan\theta(L_p - h)}{\tan\theta(D+y') + L_p - h}, \tag{2.4}$$

which is the first relation $Y_B(y')$. Then, the angle β is a measure of the position A' on the camera grating: $\tan\beta = -Y'/f_c$. In the triangle $C'c'b_0$, the angle β is involved as well and we get

$$\tan\beta = -\frac{Y'}{f_c} = \frac{y'}{L_c - h}. \tag{2.5}$$

This gives us the second relation, namely $y'(Y')$. Eliminating y' from the relations in Eqs. (2.4) and (2.5), we deduce $Y_B(Y')$:

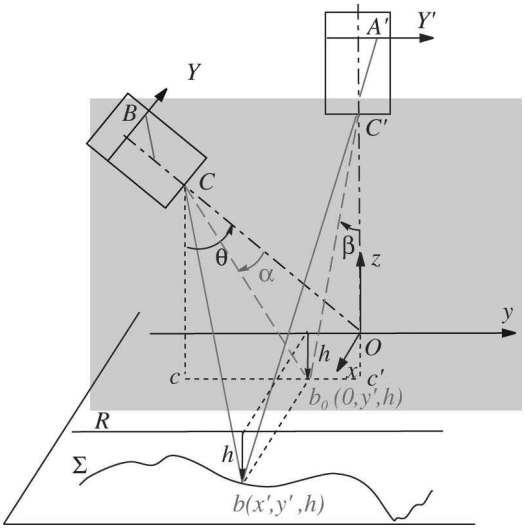


Fig. 3. In general, the rays Cb and bC' are not in a vertical plane. We define $b_0(0,y',h)$ as the projection of $b(x',y',h)$ in the plane $x=0$ (which contains O, C, and C'). In this vertical plane $x=0$, the angles α and β, respectively, measure $(\widehat{OCb_0})$ and $(\widehat{OC'b_0})$. These angles measure also the positions of B and A' on the projector and on the camera grating. The angle $\theta=(\widehat{cCO})$ measures the inclination of the projector's axis with respect to the camera's axis.

$$Y_B=-f_p\frac{D-(L_c-h)Y'/f_c-\tan\theta(L_p-h)}{L_p-h+\tan\theta[D-(L_c-h)Y'/f_c]}, \qquad (2.6)$$

and finally, the Eqs. (2.2) and (2.3) are

$$\varphi(X',Y')=\frac{\omega_c}{\cos\theta}\frac{(1-h/L_c)Y'+G_c[(L_p-h)\tan\theta-D]}{(1-h/L_p)-\tan\theta L_p^{-1}[(1-h/L_c)Y'/G_c-D]},$$
$$\varphi_0(X',Y')=\frac{\omega_c}{\cos\theta}\frac{Y'+G_c[L_p\tan\theta-D]}{1-\tan\theta L_p^{-1}[Y'/G_c-D]}. \qquad (2.7)$$

The above relation for $\varphi(X',Y')$ is in agreement with Rajoub's result, Eq. (36) in [17] (see also the note in [18]).

To conform with most of the literature, we express φ as a function of (x,y) owing to $x=-X'/G_c$, $y=-Y'/G_c$:

$$\varphi(x,y)=-\frac{\omega}{\cos\theta}\frac{y-L_p\tan\theta+D+h/L_c(L_c\tan\theta-y)}{1+\tan\theta(D+y)/L_p-h/L_p(1+\tan\theta y/L_c)},$$
$$\varphi_0(x,y)=-\frac{\omega}{\cos\theta}\frac{y-L_p\tan\theta+D}{1+\tan\theta(D+y)/L_p}. \qquad (2.8)$$

Finally, it is important to note that the shift in the position is given by $\delta x\equiv x'-x$ and $\delta y\equiv y'-y$, since the height h is measured at (x',y') and not at (x,y). The shift in y is directly obtained from $\tan\beta=y/L_c=y'/(L_c-h)$. The shift in x is easily obtained by using the property that the ray bC' coincides with the ray aC' (Fig. 3 and see the note in [19]). We get

$$x'=x-\frac{h}{L_c}x, \qquad y'=y-\frac{h}{L_c}y, \qquad (2.9)$$

with $h=h(x',y')$.

In the following, we inspect the case of the usual configurations of parallel- and crossed-optical-axes geometry. Also, we consider now $L=L_c=L_p$ (Fig. 4).

A. Parallel-Optical-Axes Geometry

This case Fig. 4(a) is deduced from the preceding relations in Eq. (2.8) with $L=L_c=L_p$ and $\theta=0$, leading to

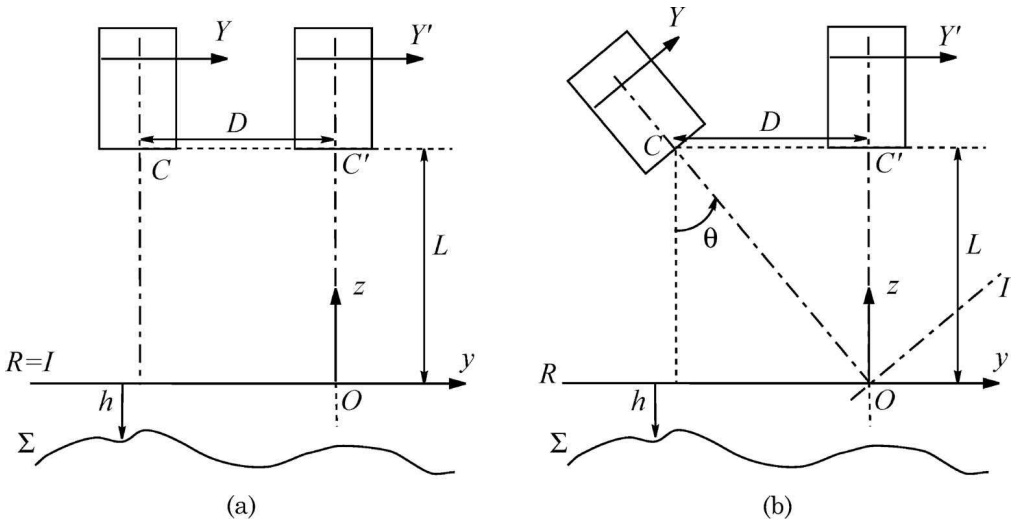


Fig. 4. Optical setup for the projector and the camera at the same distance L from the reference plane R, (a) in the parallel- and (b) in the crossed-optical-axes geometries.

$$\Delta\varphi(x,y) = -\omega_0 \frac{Dh(x',y')}{(1+\sin^2\theta y/D)[1+\sin^2\theta y/D - h(x',y')/L(1-\sin^2\theta(1-y/D))]}, \tag{2.14}$$

$$\varphi(x,y) = -\omega y - \omega D\frac{L}{L-h(x',y')}, \qquad \varphi_0(x,y) = -\omega y - \omega D. \tag{2.10}$$

Thus,

$$\Delta\varphi(x,y) = -\omega D\frac{h(x',y')}{L-h(x',y')}. \tag{2.11}$$

This relation is in agreement with the relation derived by Takeda (Eq. (1.1) with $\omega_0 = \omega$ here). However, the h value is measured at the (x',y') position, not at the (x,y) position, as assumed by Takeda. This shift in the position is $(\delta x = x' - x = -h/Lx, \delta y = y' - y = -h/Ly)$. Experimental evidence of this discrepancy is presented in Subsection 3.C.

As expected in that configuration, $\varphi_0(x,y)$ is p periodic along y $(p = 2\pi/\omega)$ since the image plane of the projector I and the object plane of the camera R coincide.

B. Crossed-Optical-Axes Geometry

In that case [Fig. 4(b)], the relations in Eq. (2.8) are used owing to $L = L_c = L_p$ and $\tan\theta = D/L$. We get

$$\varphi(x,y) = -\omega\cos\theta \times \frac{y + h(x',y')/L(D-y)}{1+\sin^2\theta y/D - h(x',y')/L[1-\sin^2\theta(1-y/D)]},$$
$$\varphi_0(x,y) = -\omega\cos\theta\frac{y}{1+\sin^2\theta y/D}. \tag{2.12}$$

As expected, $\varphi_0(x,y)$ is not periodic along y since the image plane of the projector I and the object plane of the camera R do not coincide. Note that the expression of $\varphi_0(x,y)$ in Eq. (2.12) differs from the usually cited relation for the varying frequency $f(y) \equiv \varphi_0(x,y)/(2\pi y)$ when fringe pattern is projected on the reference plane [12,13,20]:

$$\varphi_{0S}(x,y) = -\omega\cos\theta[1 - 2\sin\theta\cos\theta y/L]. \tag{2.13}$$

This error has been analyzed in [17] and it can be seen here that the expression is not valid, even in the approximation $y/L \ll 1$, as used in [20]. Experimental evidence of this error is shown in the forthcoming Fig. 8, Section 3. We get

where we have defined, following Takeda's notation, $\omega_0 \equiv \omega\cos\theta$ ($p_0 = 2\pi/\omega_0$ is the periodicity of the fringes when projected in the image plane I of the projector).

The relation between the measured unwrapped phase distribution $\Delta\varphi$ to the object height h in Eq. (2.14) clearly differs from Takeda's relation

$$\Delta\varphi_T(x,y) = -\omega_0\frac{Dh(x,y)}{L-h(x,y)}. \tag{2.15}$$

The source of the error in Takeda's derivation is discussed in Section 4 and exemplified in Subsection 3.C. However, many studies using Takeda's law have obtained good results [5,6,12,13], suggesting that the error might be negligible. It is easy to see that

$$\Delta\varphi = \Delta\varphi_T\mathcal{C}(\theta, h/L, y/D), \tag{2.16}$$

where

$$\mathcal{C}(\theta,h/L,y/D) = \left[1+\sin^2\theta\left(\frac{y}{D} - \frac{h}{L-h}\right)\right]^{-1} \times \left[1+\sin^2\theta\frac{y}{D}\right]^{-1}. \tag{2.17}$$

The function $\mathcal{C} \sim 1$ for (i) the angle $\theta \ll 1$ and (ii) $h/L \ll 1$, $y/D \ll 1$. These conditions are often fulfilled in the referenced studies: for instance, $\theta \sim 0.19$ rad, $h/L \sim 0.07$, and $y/D \sim 0.3$ in [14], or $\theta \sim 0.3$ rad., $h/L \sim 0.0045$, and $y/D \sim 0.2$ in [6]. This explains the agreement with Takeda's law presented in the literature. To summarize, the error in Takeda's law is

$$\Delta\varphi = \Delta\varphi_T[1 + O(\theta^2 h/L, \theta^2 y/D)]. \tag{2.18}$$

However, it is now evident that this error proves to be very important in the case of short-range profilometry, where $h/L \sim 1$, and in large-field profilometry, in which the object's size is comparable to the camera–projector distance.

3. Experimental Results

In this section, we inspect experimentally the reconstruction of h on the basis of Eqs. (2.11) and (2.14) together with Eq. (2.9). To do that, we carried out the following experiment. The measured object is a triangular prism with base line 6 cm and height 3 cm. The prism is placed on the reference plane R (Fig. 5) at a distance y_0 of the camera axis (the triangle is symmetric with respect to the $y = y_0$ axis).

Thus, the surface Σ differs from the reference plane R only in a region $-3\,\text{cm} < y - y_0 < 3\,\text{cm}$, hereafter referred to as the T region. The height $h(x,y)$ is invariant along the x direction, perpendicular to the plane of Fig. 5. Otherwise, $L = 105.2\,\text{cm}$, θ can vary, and, for $\theta = 0$ (parallel-optical-axes configuration), we have $D = 18\,\text{cm}$.

A sinusoidal fringe pattern is projected onto the object and a CCD camera is used to record the deformed fringe of the object. Details on the optical devices are given below; afterward, the results are presented and analyzed.

A. Optical Devices

Fringe-pattern projection is achieved by means of a computer-controlled digital videoprojector with a high resolution of 1920 pixels × 1080 pixels and 12 bit depth per color. An important improvement arising from the use of a digital video projector is that we are able to project sinusoidal fringe patterns with a controlled wavelength. Usually, the projected pattern is a square profile (Ronchi grating), extremely unadapted for Fourier analysis. Indeed, the use of a sinusoidal grating strongly increases the quality of the filtering process as well as the phase recovering. Another important improvement with a video projector compared to a slide-projector usually employed is that a video projector can project an image on a surface shifted with respect to its axis and, hence, more centered to the camera axis. The video projector allows a correction of the projected image so that the image is not distorted and keeps the fringes' wavelength constant all over the image and maintains the original sharpness. However, due to the fact that the projected pattern varies discretely in space and is digitized in intensity, the video projector's resolution is lower than that of a slide projector.

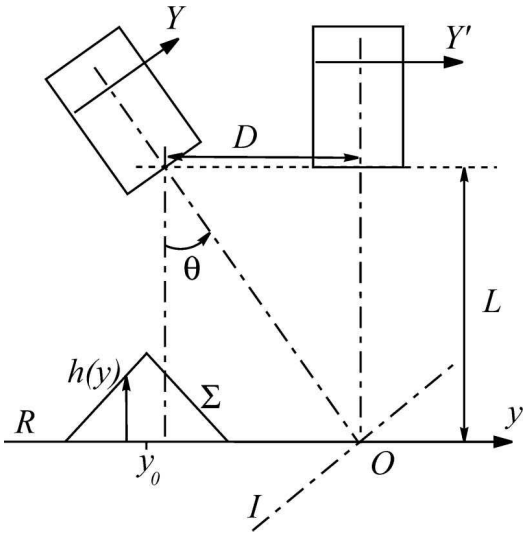


Fig. 5. Experimental configuration: Σ is at distance $h(y)$ from the reference plane R with $h(0 < y - y_0 \le -3\,\text{cm}) = y$, $h(0 < y - y_0 \le 3\,\text{cm}) = -y$ zero, otherwise. I is the image plane of the projector. In the experiments, $L = 105.2\,\text{cm}$ and θ can vary, and for $\theta = 0°$ (parallel-optical-axes geometry), $D = 18\,\text{cm}$.

For a given projection distance, the size of the projected optical field can be adjusted (by means of the projector zoom optics) to cover either a small or a relatively large area of the surface. In particular, we employed a projection distance of $L = 1\,\text{m}$, which allowed us to work with projection windows of sizes ranging from approximately 36 cm × 20 cm to 80 cm × 45 cm.

The fringe patterns projected onto the object were recorded by a Fujifilm Finepix S2 Pro SRL-type digital still camera, with a 3024 pixel × 2016 pixel CCD and a color depth of 16 bits per color. To avoid any artifact from the camera's preprocessing algorithm (such as those coming from quantization, compression, color depth reduction, etc.) we worked with raw images that were later developed into portable pixmap (PPM) format at full color depth.

The whole fringe-projection and image-capturing system is held over the channel, supported by a mobile structure that allows for precise alignment and repositioning of the optical devices. The whole setup has been tested and validated in a previous study [21].

B. Intensity Variations Captured by the Camera

Figures 6 show the intensity variations $I(x,y)$ on the surface Σ recorded by the camera (as previously said, h and thus I are invariant along the x direction). The cases of the parallel- and the crossed-optical-axes geometries (with $\theta = 33.9°$, thus $D = 70.7\,\text{cm}$ in that case) are shown. Figure 7 shows the corresponding curves $I(y)$, averaged over the x direction.

Several remarks can be made regarding these figures. In the case of parallel optical axes, the T region, where a change in height occurs, is well resolved on both sides. Outside of this region, the fringes are regularly spaced (with period $p \simeq 0.27\,\text{cm}$ invariant from left to right). In the T region, h linearly increases for $-3\,\text{cm} < y < 0$ and then linearly decreases for $0 < y < 3\,\text{cm}$. From the expression of $\varphi(x,y)$ in Eq. (2.10), it is easy to see that $h = ay$ leads to an apparent frequency $\omega_a \simeq \omega(1 + aD/L)$ and fringe spacing of $p_a \simeq p/(1 + aD/L)$. In our experiments, $a = \pm 1$ and $D/L = 0.171$ give $p_a = 0.24\,\text{cm}$ and $p_a = 0.34\,\text{cm}$ as observed in Figs. 6(a) and 7(a) (see also Appendix A.

In the crossed-optical-axes geometry (here, for $\theta = 33.9°$), the T region is badly resolved for $0 < y < 3\,\text{cm}$ because of the projected shadow. Outside of this region, the fringes are not regularly spaced because the image plane I of the projector does not coincide with the reference plane. The fringe spacing varies from roughly 0.35 to 0.4 cm from left to right. This increase in the spacing p_n ($n = 0$ at the origin O) is as expected: $p_n = p_I/\cos\theta[1 - n\sin\theta p'/L]^{-1}[1 - (n-1)\sin\theta p_I/L]^{-1}$, where p_I is the fringe spacing observed on the image plane of the projector I (see Appendix A). Here, p_I can be deduced from p owing to the invariant $p_p/f_p = p/L = p_I\cos\theta/L$; thus, $p_I \simeq 0.325\,\text{cm}$. Finally, as in the parallel-optical-axes geometry, a successive decrease and increase in the fringe spacing in observed in the T region. From Eq. (2.12), $p_a \simeq p_I/[\cos\theta(1 + a\tan\theta)]$ gives

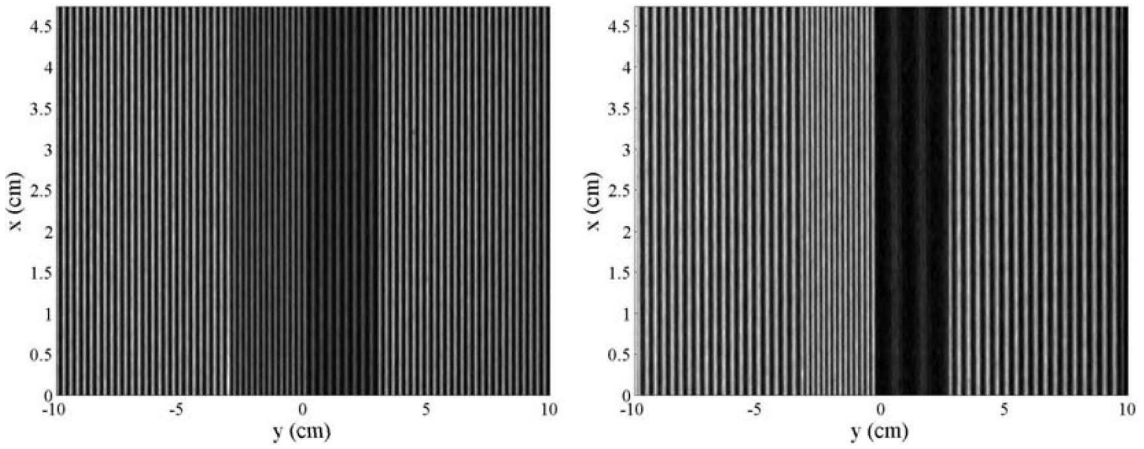


Fig. 6. Experimental intensity variations $I(x,y)$ captured by the camera (a) in the parallel-optical-axes geometry with $D = 18\,\text{cm}$ and $L = 105.2\,\text{cm}$ and (b) in the crossed-optical-axes geometry with $D = 70.7\,\text{cm}$ ($\theta = 33.9°$), $L = 105.2\,\text{cm}$, and $y_0 = 0$.

$p_a = 0.23\,\text{cm}$ and $p_a = 1.19\,\text{cm}$. The agreement is good (see the Appendix A). Finally, Fig. 8 shows the unwrapped phase $\varphi_0(y)$ (see [22]) deduced from $I_0(y)$ when projected onto the reference plane in the absence of the triangle ($I_0(y)$ corresponds to the average of $I_0(x,y)$ in the x direction). It can be seen that our expression in Eq. (2.12) accurately fits the experimental points while the expression given in [12,13,20] [see Eq. (2.13)] significantly fails to reproduce the data.

C. Phase-to-Height Inversion

In this section, from the experimental curves of $I_0(y)$ and $I(y)$, we deduced the unwrapped phase difference $\Delta\varphi(y)$. Then, we use the inversion of Eqs. (2.11) and (2.14) together with Eq. (2.9) to get the height $h(y)$. The comparison with Takeda's law is presented.

1. *Parallel-Optical-Axes Geometry*

Figures 9 illustrate the phase-to-height inversion (the additional dependence of $\Delta\varphi(y)$ on x is omitted because of the aforementioned invariance along x in our experiments): from $I(y)$ and $I_0(y)$ [Fig. 9(a)], we extract the phase difference $\Delta\varphi(y)$. This is done by filtering the 2D Fourier transform of $I(I_0)$ around the main frequency ω (in the present case, a simple Gaussian filter of width $\omega/2$ is used). The inverse Fourier transform is a complex signal whose unwrapped phase is $\varphi(y)$ (correspondingly, $\varphi_0(y)$), and then $\Delta\varphi = \varphi - \varphi_0$ [Fig. 9(b)]. In the parallel-optical-axes geometry, the inversion of $\Delta\varphi(y)$ gives, both in our approach and in Takeda's approach,

$$h(y') = \frac{L\Delta\varphi(y)}{\Delta\varphi(y) - \omega_0 D}, \tag{3.1}$$

with $y' = y + \delta y$ and $\delta y = -yh/L$. Figure 9(c) shows the reconstructed height; here the shift in position δy is visible: $\Delta\varphi$ reaches its extremum at $y \sim -25\,\text{cm}$ while h reaches its maximum at $y = y_0 = -24\,\text{cm}$. The agreement between the reconstructed shape and the real shape is good, very comparable to the results obtained in a similar experiments [10].

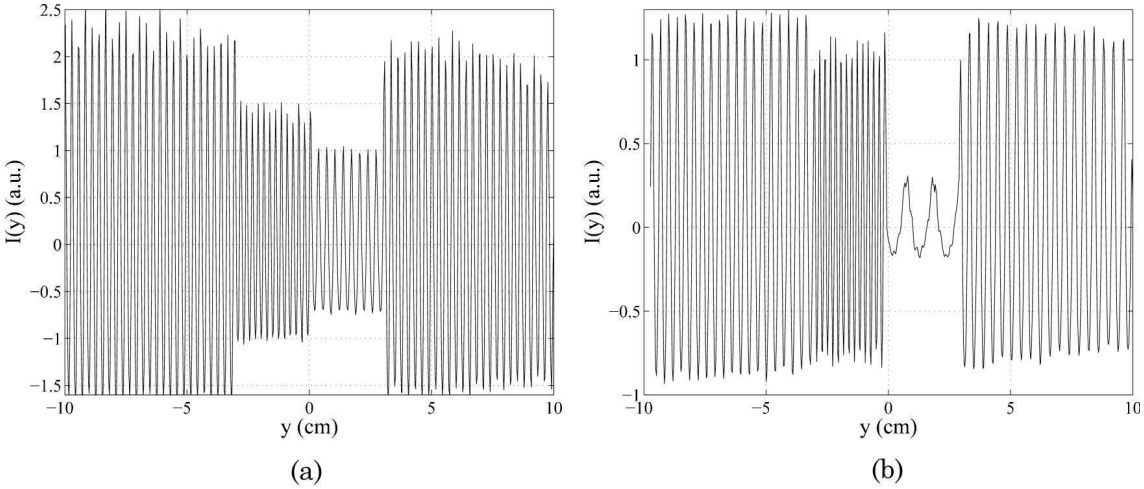


Fig. 7. Intensity variations $I(y)$ in (a) the parallel- and (b) the crossed-optical-axes geometries. The curves correspond to the averages over the x direction of the 3D plot in Fig. 6.

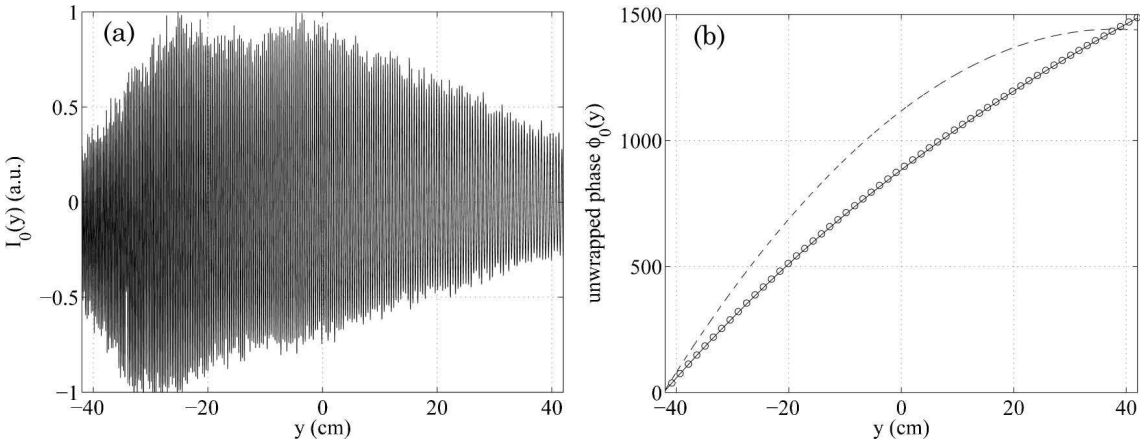


Fig. 8. (a) Intensity variations $I_0(y)$ for fringe projection onto the reference plane in the absence of the triangular prism and (b) the corresponding unwrapped phase $\varphi_0(y)$ (see [23]). Experiments correspond to $\theta = 33.9°$ with $L = 105.2\,\text{cm}$. The points are the experimental data (only one point of each 150 points is indicated for visibility), the solid curve corresponds to our Eq. (2.12) and the dashed curve corresponds to Eq. 2.13 from [12,13,20].

The error in Takeda's approach consists of neglecting the spatial shift of the sampling points introduced by the object's height profile.

Figure 10 presents a comparison between the reconstructed heights h and h_T, obtained using Eq. (3.1), including or omitting, respectively, the shift δy for various y_0 values. As expected, the error in h_T increases when y_0 increases. The maximum error in the shift is $\delta y_{\max} = y_0 h_{\max}/L$ (thus, a constant relative error $\delta y/y_0 = h_{\max}/L = 2.85\%$), which leads to, for $y_0 = -8\,\text{cm}$, $\delta y_{\max} = 0.23$ (0.2 experimentally obtained); for $y_0 = -16\,\text{cm}$, $\delta y_{\max} = 0.456$ (0.4 experimentally obtained); and, for $y_0 = -24\,\text{cm}$, $\delta y_{\max} = 0.684$ (0.66 experimentally obtained).

2. *Crossed-Optical-Axes Geometry*

The same experiments have been performed in the crossed-optical-axes geometry. In that case, the inversion is, from Eq. (2.14),

$$h(y') = \frac{L\Delta\varphi(y)(1+\sin^2\theta y)^2}{\Delta\varphi(y)(1+\sin^2\theta y/D)[1-\sin^2\theta(1-y/D)] - \omega_0 D}. \tag{3.2}$$

The position of the triangular prism y_0 and the angle between the optical axes θ have been varied. The procedure to derive $\Delta\varphi(y)$ is the same as in the parallel-optical-axes geometry, but a wider filter has been used (of width around ω) to account for the change in the frequency in the nonperiodic signal. The peak in the Fourier transform corresponds in that case to the mean fringe periodicity. Figure 11(a) shows the results obtained varying y_0 for $\theta = 33.9°$ and Fig. 11(b) shows the results obtained varying θ for $y_0 = -16\,\text{cm}$. Both figures exemplify the error due to the use of Takeda's result, while our present inversion gives a good height reconstruction. Note that Takeda's expression of the height h_T in Eq. (1.1) is given as a function of h by

$$h_T(y) = \frac{h(y')}{A^2 + (AB + h(y'))h(y')/L}, \tag{3.3}$$

with $A \equiv 1 + \sin^2\theta y/D$ and $B \equiv \cos^2\theta - \sin^2\theta y/D$.

4. On Takeda's Calculation

In [16], it is said that Takeda's approach uses an unjustified hypothesis of collimated projection. We will show that this is not the case. Actually, the expressions of the phases φ and φ_0 are correct in [2] but an erroneous subtraction of the two phases leads to an error in the phase difference.

Let us recall the meaning of the phase difference φ: it corresponds to the change in intensity at a given

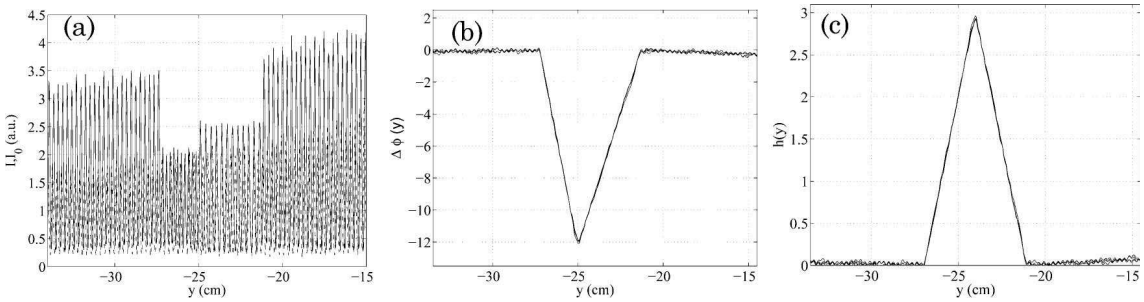


Fig. 9. (a) Signals $I_0(y)$ and $I(y)$ for fringe projections on the reference plane R and on the Σ plane. (b) Unwrapped phase difference $\Delta\varphi(y)$ and (c) reconstructed height $h(y)$ using Eqs. (2.9) and (2.11). The experiment is conducted in the parallel-optical-axes geometry with $L = 105.2\,\text{cm}$, $D = 18\,\text{cm}$, and $y_0 = -24\,\text{cm}$.

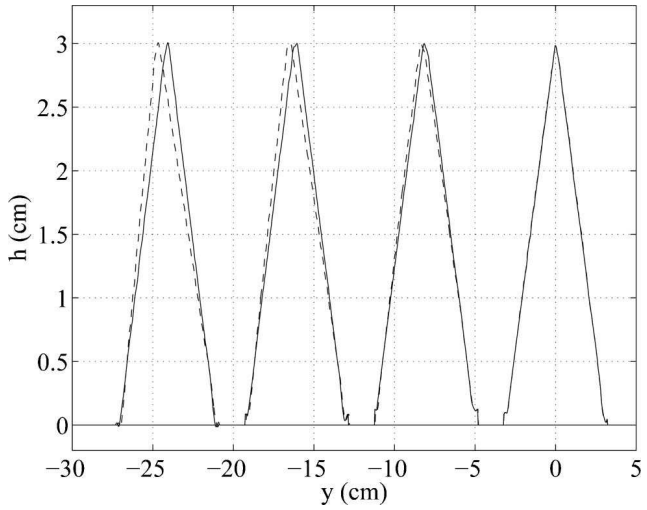


Fig. 10. Height reconstruction $h(y)$ for various y_0 values. Solid curves correspond to our phase-to-height relation and dashed curves correspond to Takeda's phase-to-height relation. The experimental configuration is the same as in Fig. 9.

pixel of the camera (A' in Fig. 2) for a change in the reflecting surface (say R and Σ). The intensity at this pixel changes because the rays arriving at A' come from two different points of the projector grating (A and B in Fig. 2).

Takeda's geometrical representation [reproduced in Fig. 12(a), for reference] is different from our Fig. 2. Two rays coming from the same point B of the projector grating are considered: the ray BaA' for a reflecting surface being R and the ray BbB' for a reflecting surface being Σ. Of course, these two rays produce the same intensity, either on A' or on B' in the camera. When R is the reflecting surface, the ray BA' is seen as coming from a on R, when Σ is the reflecting surface, the ray BB' is seen as coming from b_a on R [Fig. 12(b)]. Again, the two rays hold the same intensity:

$$\varphi = \omega_p Y_B. \tag{4.1}$$

Following Takeda, geometric considerations allow expressing the phases φ_0 and φ. First, from Figs. 12, $X_B = (f_p \cos\theta / L)\overline{Ob'}$, with b' as the point intercepting I along the ray Bb. Thus, we have $\varphi = \omega\overline{Ob'}$, where $\omega = \omega_p / G_p$ is the frequency of the fringes on the plane I (the fringes are regularly spaced on that plane). We can now define $\omega_0 = \omega\cos\theta$ as in Takeda's paper and we get, introducing b_a as the point intercepting R along the ray bB',

$$\varphi = \omega\overline{Ob'} = \omega_0\overline{Ob_a} + \omega_0\left(\frac{\overline{Ob'}}{\cos\theta} - \overline{Ob_a}\right). \tag{4.2}$$

The point b_0 is the point intercepting R with $b'b_0$ parallel to the projector's axis CO. It is sufficient to remark that $\overline{Ob_0} = \overline{Ob'}/\cos\theta$ (since the triangle Ob_0b' is a rectangle at b' by construction of the point b_0). We deduce, as Takeda,

$$\varphi(y) = \omega_0 y + \omega_0\overline{b_a b_0}, \tag{4.3}$$

where it has been implicitly defined that $y = \overline{Ob_a}$.

The following step in Takeda's approach is to consider the same ray coming from B when the reflecting surface is R (the Oy plane). In that case, the ray is reflected on R at point a. The same geometric considerations can be done: we have $a' = b'$ and $a_0 = b_0$ because the ray Ba used to define a' and a_0 is the same as the ray Bb, and we have $a_a = a$. We get

$$\varphi_0(y') = \omega_0 y' + \omega_0\overline{ab_0}, \tag{4.4}$$

but here, $y' = \overline{Oa}$.

Both expressions in Eqs. (4.3) and (4.4) are correct. The error in Takeda's approach is to build $\Delta\varphi(y)$ from the difference between both expressions, considering $y' = y$: Takeda's phase difference is $\Delta\varphi_T(y) = \varphi(y' = y) - \varphi_0(y)$. This erroneous subtraction gives

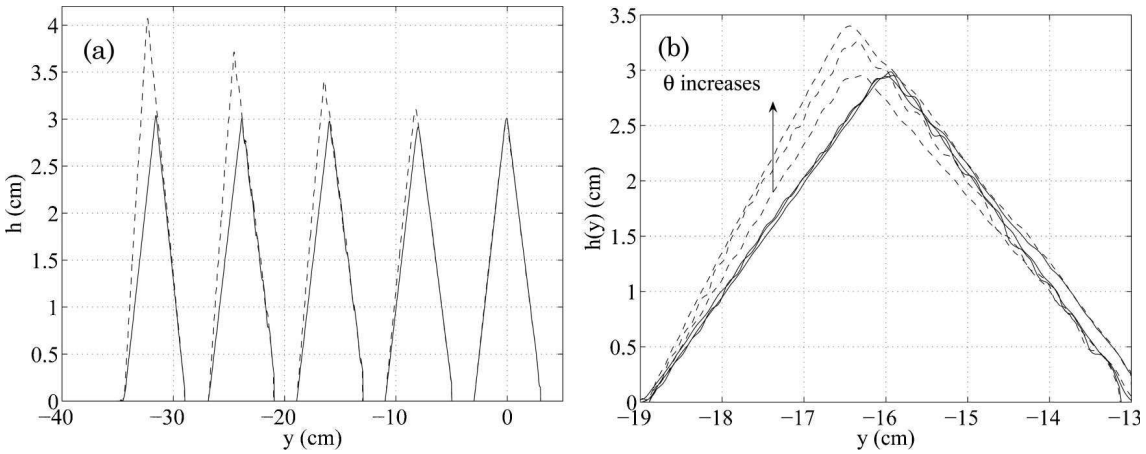
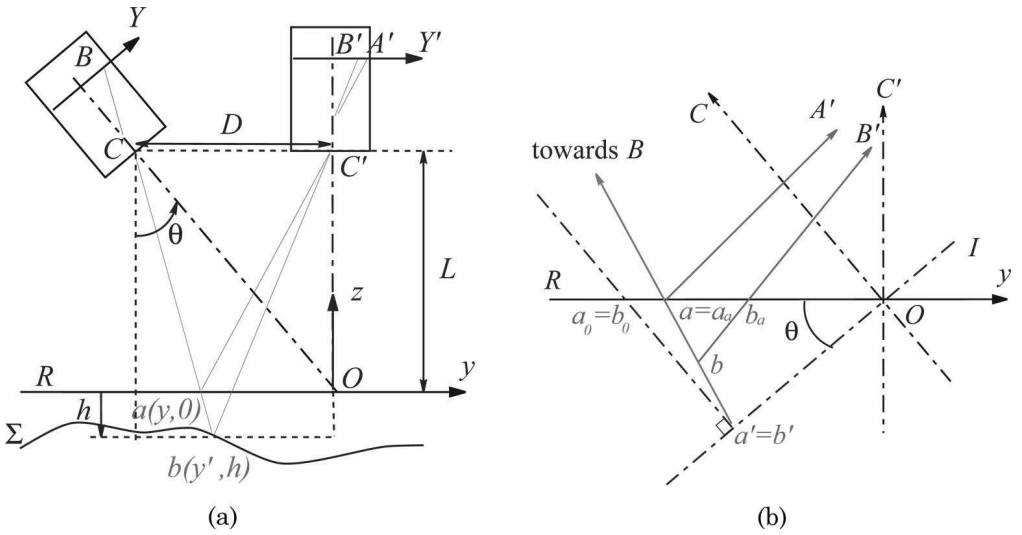


Fig. 11. Reconstructed height $h(y)$ in the crossed-optical-axes geometry (a) for $\theta = 33.9°$ and varying the y_0 position of the triangle and (b) for $y_0 = -16$ cm and varying $\theta = 0$, 18.1 and 41°. Solid curves correspond to our height reconstruction from Eq. (3.3) with Eq. (1.2). Dashed curves are the height reconstructed using Takeda's relation Eq. (1.1).



(a) (b)

Fig. 12. (a) Reproduction of Takeda's representation and (b) the same representation including useful additional points: b' is the point of the ray Bb on the plane I, b_a is the point of ray bB' on the plane $R(Oy)$, and b_0 is the point on plane R with b_0b' parallel to the projector's optical axis CO. Similar construction is used to define a_a, a_0, and a'.

$$\Delta\varphi_T(y) = \omega_0\overline{b_a a} = -\omega_0\frac{hD}{L-h}. \tag{4.5}$$

When considering the correct definitions of y and y', the terms $\omega_0(y'-y)$ remain (with $y=\overline{Ob_a}$ and $y'=\overline{Oa}$) and we get

$$\Delta\varphi = \omega_0(\overline{Ob_a}-\overline{Oa}) + \omega_0(\overline{b_a b_0}-\overline{ab_0}) = 0, \tag{4.6}$$

which is expected, since the two rays hold the same intensity !

However, with $\varphi_0(y)$ and $\varphi(y')$ being correctly derived, it is easy to correct the last erroneous operation. We keep the same expression for $\varphi(y)$ (the ray is BbB'). To derive φ_0, we consider the ray AaB', with $a=b_a$ that is seen by the camera as coming from b_a, as illustrated on Fig. 13. We have $Y_A/f_p = \overline{Oa'}\cos\theta/L$, but now, a' differs from b' (and $a_0 \neq b_0$). We have now a unique definition of $y=\overline{Ob_a}=\overline{Oa}$ and

$$\varphi(y) = \omega_0 y + \omega_0\overline{ab_0}, \tag{4.7}$$

$$\varphi_0(y) = \omega_0 y + \omega_0\overline{aa_0}, \tag{4.8}$$

from which we deduce

$$\Delta\varphi(y) = \omega_0\overline{a_0 b_0}. \tag{4.9}$$

This expression is correct and equivalent to our expression in Eq. (2.11) for $\theta=0$ and to our expression in Eq. (2.14) for $D=L\tan\theta$ (see the note in [23]).

5. Concluding Remarks

We have inspected the 3D phase-to-height relationship used in fringe-projection profilometry in the cases of collimated and noncollimated projection. In the past ten years, the need for performing accurate noncontact measurements has motivated studies on signal processing, such as unwrapping phase algorithms [5,14,15] or filtering techniques [8–11]. The goal is to enhance the quality of the height reconstruction in these methods. Thus, it is important that the basic phase-to-height relation is exact (at least in the geometric optics approximation). We have confirmed the relation first given by Rajoub *et al.* [17] and we have given experimental evidence of this analytical prediction. Also, the error due to the usually cited phase-to-height relation in Eq. (1.1) is explained and experimentally exemplified.

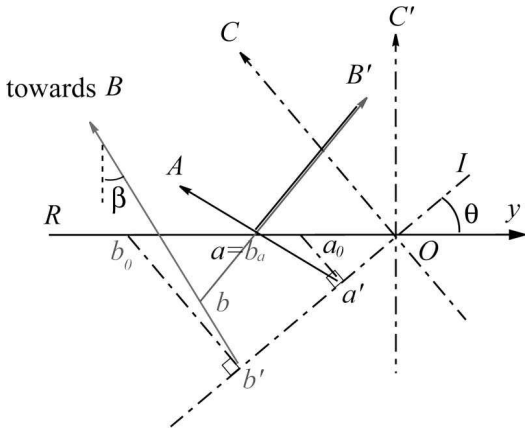


Fig. 13. Same representation as in Fig. 12(b) considering the ray AaB' instead of the ray BaA'. Now the ray AB' is seen by the camera as coming from point $a=b_a$. Otherwise, the same definitions for the points a', b' and a_0, b_0 as in Fig. 12(b) are used.

Appendix A: On the Fringe Spacing in Crossed-Optical-Axes Geometry

The object of this appendix is to derive Eq. (A5), which gives the change in the fringe spacing on the reference plane R in the crossed-optical-axes geometry.

We report in Fig. 14 the figure used in [17]. On the projector grating, we consider the rays r_n with $2n\pi$ phase difference with the ray CO. r_n forms an angle α_n with CO. The two successive rays r_n and r_{n+1} have 2π phase difference.

The conjugate image of the projector's grating is formed on the plane I, with a regular spacing p_I, and we denote w_n as the point of r_n on I.

The fringe spacing on the reference plane R varies along y and we denote $p_{n+1} \equiv y_{n+1} - y_n$ with y_n as the point of r_n on R. The aim of this appendix is to derive p_n.

On I, we have

$$\tan\alpha_n = \frac{\overline{Ow_n}}{L/\cos\theta}, \qquad \overline{Ow_n} = np_I, \tag{A1}$$

where the last relation is drawn from the fact that I is the conjugate plane of the projector image plane. On R, we have

$$\tan(\theta+\alpha_n) = \frac{\overline{C'y_n}}{L}. \tag{A2}$$

With $\overline{C'y_n} = L\tan\theta + y_n$, we get

$$p_{n+1} = L[\tan(\theta+\alpha_{n+1}) - \tan(\theta+\alpha_n)], \tag{A3}$$

which simplifies in

$$p_{n+1} = \frac{L}{\cos^2\theta}\frac{\tan\alpha_{n+1} - \tan\alpha_n}{(1-\tan\theta\tan\alpha_n)(1-\tan\theta\tan\alpha_{n+1})}. \tag{A4}$$

With $\tan\alpha_n = np_I\cos\theta/L$ from Eq. (A1), we get

$$p_{n+1} = \frac{p_I}{\cos\theta}\frac{1}{(1-n\sin\theta p_I/L)[1-(n+1)\sin\theta p_I/L]}. \tag{A5}$$

The above formula is exact and can be easily calculated in practice.

From our experimental configuration described in Subsection 3.B, we can deduce the fringe spacing p_I on I from the fringe spacing p obtained in the parallel-optical-axes configuration: $p_I = p/\cos\theta$. We have $p \simeq 0.27$ cm from Fig. 7(b) outside the T region; thus, $p_I \simeq 0.325$ cm. Then, p_n is calculated from Eq. (A5). Figure 15 shows the fringe spacing experimentally deduced from Fig. 7, both in the parallel- and in the crossed-optical-axes geometries. The apparent frequency is given as well in the T region (for a linear increase or decrease of the height $h(y)$ with slopes ± 1). In the parallel-optical-axes geometry, $p_a \simeq p/(1 \pm D/L)$ (in the referred experiments, $D = 18$ cm and $L = 105.2$ cm) and, in the crossed-optical-axes geometry, $p'_a \simeq p_I/[\cos\theta(1 \pm \tan\theta)]$ (in the referred experiments, $\theta = 33.9°$.). Note that a reasonable fit of the experimental data are obtained in the crossed-optical-axes geometry using $p_I \sim 0.313$ cm, suggesting an error of around 3% either in the angle θ or in the position of the plane I.

Rajoub *et al.* [17] show that the derivation of p_n in [20] is inexact and propose the approximate expression (Eq. (20) in [17]). Unfortunately, their derivation contains a mistake from his Eq. (15) to Eq. (16), where they have used $w_n = y_{w_n}\cos\theta$ instead of using $w_n = y_{w_n}/\cos\theta$. Owing to this correction, we get a modified version of his Eq. (20) (replacing simply y_{w_n} by $y_{w_n}/\cos^2\theta$):

$$p_n \simeq \frac{p_0}{\cos\theta}\frac{1+\sin\theta\cos\theta y_{n+1}/L}{1-\tan\theta y_{w_n}/L}, \tag{A6}$$

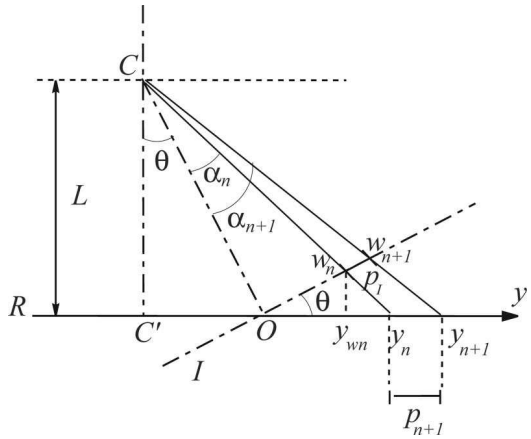


Fig. 14. System geometry used to calculate the fringe spacing p_n in the crossed-optical-axes geometry.

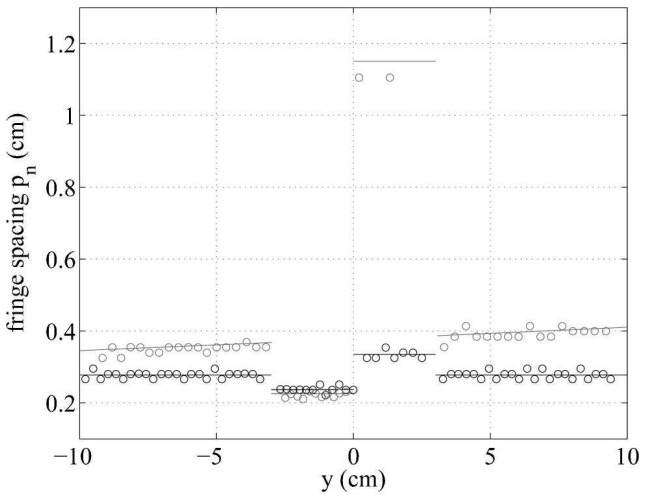


Fig. 15. Open circles, experimental fringe spacing deduced from Fig. 7 in the parallel- and the crossed-optical-axes geometries (the crossed-axes geometry gives higher fringe spacing). The solid curves correspond to our expression in Eq. (A5) and in the body of the text.

where it has been assumed that the linear dimension of the illuminated area, Ow_{n+1}, is small compared to the projection distance $L/\cos\theta$, thus, α_n is small. Rajoub concludes, however, that the above expression contains two unknowns y_{n+1} and y_{w_n}. They are actually known; owing to $y_{n+1} = L[\tan(\theta + \alpha_{n+1}) - \tan\theta]$ and $y_{w_n} = np_0\cos\theta$ (the triangle $Ow_n y_{w_n}$ is rectangle at y_{w_n}), we get

$$p_n \simeq \frac{p_0}{\cos\theta}\frac{1+\sin\theta\cos\theta[\tan(\theta+\alpha_{n+1})-\tan\theta]}{1-\sin\theta\cos\theta np_0/L}, \quad \text{(A7)}$$

which simplifies exactly in the same expression as our Eq. (A1) (suggesting that the assumption of small α_n angles is not necessary in [17]).

Appendix B: The Case of Collimated Projection

In this appendix, we derive the expression of the phase difference $\Delta\varphi$ for collimated projection (incidentally, it will be seen that Takeda's result does not correspond to that case). The corresponding configuration is in Fig. 16. For collimated projection, the fringes are regularly spaced on any plane because the beam coming from the projector is a parallel beam.

We give here a 2D construction. The 3D construction is deduced from the 2D one owing to $X_B = -G_p x$, $X = -G_c x$.

As previously, the calculation of the phase $\varphi(x,y)$ is performed considering the surface Σ as reflecting surface; afterward, $\varphi_0(x,y)$ is deduced for the surface R ($h = 0$ in this case). The ray BbA' is considered, with

$$\varphi(x,y) = \omega_p Y_B, \quad \text{(B1)}$$

where $Y_B = \overline{O_c B}$ on the projector grating.

In the crossed-optical-axes geometry [Fig. 16(a)], we define b_0 as the point of the ray Bb intercepting the plane R and b_1 as the vertical projection of b onto R. It is easy to see that $\overline{Ob_0}\cos\theta = \overline{O_c B}$ and $\overline{b_1 b_0} = h\tan\theta$ (also, $\overline{Ob_1} \equiv y'$). We deduce that $\varphi(x,y) = \omega_p\cos\theta\overline{Ob_0} = \omega_p\cos\theta(y' + h\tan\theta)$, and thus

$$\varphi(x,y) = \omega_p\cos\theta y + \omega_p\sin\theta h(1 - \cot\theta y/L). \quad \text{(B2)}$$

It follows that

$$\varphi_0(x,y) = \omega_p\cos\theta y \quad \text{(B3)}$$

and the phase difference is

$$\Delta\varphi(x,y) = \omega\sin\theta h(1 - \cot\theta y/L), \quad \text{(B4)}$$

where $\omega = \omega_p\cos\theta$ is the frequency of the regularly spaced fringes on R. On a point A' of the camera grating, the intensity is given by the intensity of the point A on the projector grating with $y/L = -Y_A/f_c$. We still have $h = h(x',y')$ with $x' = x - xh/L$ and $y' = y - yh/L$.

Note that our expression of the phase $\varphi(x,y)$ in Eq. (B2) agrees with that of Rajoub (Eq. (9) in [16]) and with [24,25]. In these references, the phase difference $\Delta\varphi$ is not considered. Also, in [24,25], additional hypothesis are considered ($\varphi(x,y) \gg \omega_p y$ and $y/L \ll 1$). Finally, our Eq. (B4) agrees with [26].

In the case of parallel-optical-axes geometry [Fig. 16(b)], the relation between Y_B and y' is $Y_B = D + y'$ ($Y_A = D + y$); thus, the phases are

$$\varphi_0(x,y) = \omega_p(D+y), \qquad \varphi(x,y) = \omega_p(D+y'), \quad \text{(B5)}$$

from which we deduce (with $x' = x - xh/L$ and $y' = y - yh/L$)

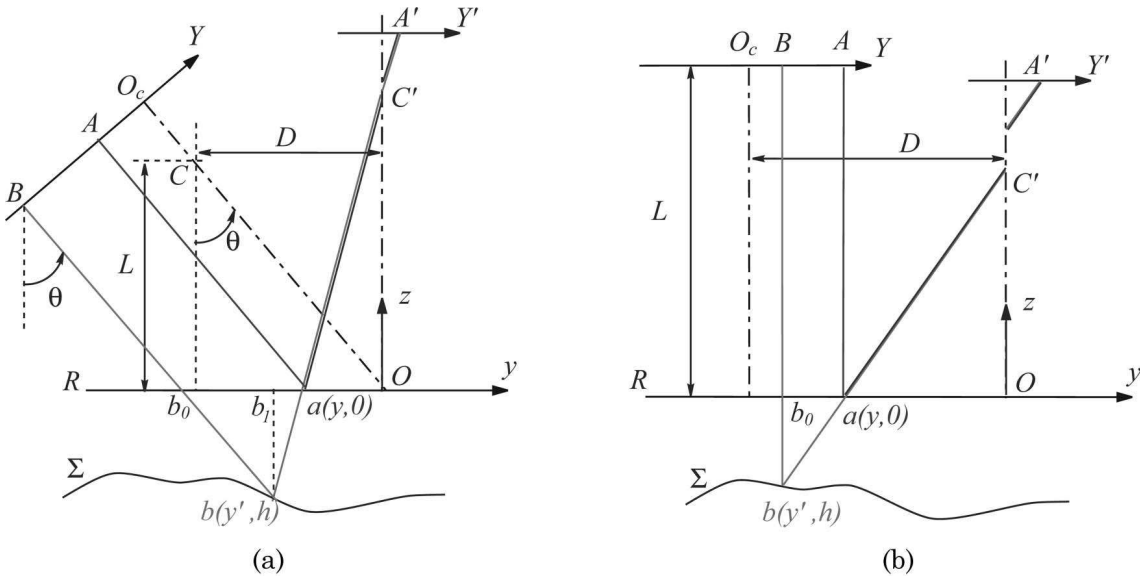


Fig. 16. Collimated projection in the (a) crossed- and (b) parallel-optical-axes geometries.

$$\Delta\varphi(x,y) = -\omega\frac{h(x',y')}{L}y. \tag{B6}$$

Note that the case of parallel-optical-axes geometry cannot be deduced from the calculations in [16].

References and Notes

1. M. Takeda, H. Ina, and S. Kobayashi, "Fourier-transform method of fringe-pattern analysis for computer-based topography and interferometry," J. Opt. Soc. Am. **72**, 156–160 (1982).
2. M. Takeda and K. Mutoh, "Fourier transform profilometry for the automatic measurement of 3-D object shapes," Appl. Opt. **22**, 3977–3982 (1983).
3. J. Yi and S. Huang, "Modified Fourier transform profilometry for the measurement of 3-D steep shapes," Opt. Lasers Eng. **27**, 493–505 (1997).
4. B. Zhao and A. Asundi, "Discussion on spatial resolution and sensitivity of Fourier transform fringe detection," Opt. Eng. **39**, 2715–2719 (2000).
5. X. Su, W. Chen, Q. Zhang, and Y. Chao, "Dynamic 3-D shape measurement method based on FTP," Opt. Lasers Eng. **36**, 49–64 (2001).
6. Q.-C. Zhang and X.-Y. Su, "An optical measurement of vortex shape at the free surface," Opt. Laser Technol. **34**, 107–113 (2002).
7. F. Berryman, P. Pynsent, and J. Cubillo, "A theoretical comparison of three fringe analysis methods for determining the three-dimensional shape of an object in the presence of noise," Opt. Lasers Eng. **39**, 35–50 (2003).
8. F. Berryman, P. Pynsent, and J. Cubillo, "The effect of windowing in Fourier transform profilometry applied to noisy images," Opt. Lasers Eng. **41**, 815–825 (2004).
9. J. Zhong and J. Weng Spatial carrier-fringe pattern analysis by means of wavelet transform," Appl. Opt. **43**, 4993–4998 (2004).
10. W. Chen, X. Su, Y. Cao, Q. Zhang, and L. Xiang, "Method for eliminating zero spectrum in Fourier transform profilometry," Opt. Lasers Eng. **43**, 1267–1276 (2005).
11. M. A. Gdeisat, D. R. Burton, and M. J. Lalor, "Eliminating the zero spectrum in Fourier transform profilometry using a two-dimensional continuous wavelet transform," Opt. Commun. **266**, 482–489 (2006).
12. X. Mao, W. Chen, and X. Su, "Improved Fourier transform profilometry," Appl. Opt. **46**, 664–668 (2007).
13. X. Mao, W. Chen, X. Su, G. Xu, and X. Bian, "Fourier transform profilometry based on a projecting-imaging model," J. Opt. Soc. Am. A **24**, 3735–3740 (2007).
14. E. Zappa and G. Busca, "Comparison of eight unwrapping algorithms applied to Fourier transform profilometry," Opt. Lasers Eng. **46**, 106–116 (2008).
15. X. Su and W. Chen, "Fourier transform profilometry: a review," Opt. Lasers Eng. **35**, 263–284 (2001).
16. B. A. Rajoub and M. J. Lalor, "A new phase-to-height model for measuring object shape using collimated projections of structured light," J. Opt. A Pure Appl. Opt. **7**, S368–S375 (2005).
17. B. A. Rajoub, M. J. Lalor, D. R. Burton, and S. A. Karout, "A new model for measuring object shape using non-collimated fringe-pattern projections," J. Opt. A Pure Appl. Opt. **9**, S66–S75 (2007).
18. Eq. (36) in [17] is rather intricate. For the sake of clarity, it is worth mentioning that our expression for $\varphi(Y)$ gives the same result as their Eq. (36) owing to the correspondences between Rajoub's notations and our notations: $y_{fp} = -D$, $z_{fp} = L_p$, $y_{op} = -D - f_p \sin\theta$, $z_{op} = L_p + f_p \cos\theta$, $z_{fc} = L_c$, $y_{oc} = 0$, $z_{oc} = L_c + f_c$, $Y_i - y_{oc} = Y$, $z_i = h$, and $\omega' = \omega_p/\cos\theta$.
19. The ray bC' has the direction of the vector $(x', y', h - L_c)$ and the ray aC' has the direction of the vector $(x, y, -L_c)$. The cross product of both vectors has to vanish and the first component of the cross product is $xh + (x' - x)L_c$. We get $\delta x \equiv x' - x = -xh/L$
20. G. S. Spagnolo, G. Guattari, C. Sapia, D. Ambrosini, D. Paoletti, and G. Accardo, "Contouring of artwork surface by fringe projection and FFT analysis," Opt. Lasers Eng. **33**, 141–156 (2000).
21. P. Cobelli, A. Maurel, V. Pagneux, and P. Petitjeans, "Fast global measurement of water waves by Fourier transform profilometry," submitted to Exp. in Fluids.
22. We have used the unwrapping algorithm *unwrap* from MATLAB (The MathWorks, 2007).
23. The useful relations are $\tan(\theta - \beta) = \overline{Ob'}\cos\theta/L$ and $\tan\beta = (D + y')/(L - h)$, with $y'/(L - h) = y/L$. β is defined in Fig. 13.
24. C. Quan, C. J. Tay, H. M. Shang, and P. J. Bryanston-Cross "Contour measurement by fibre optic fringe projection and Fourier transform analysis," Opt. Commun. **118**, 47983 (1995).
25. F. Lilley, "An optical 3-D body surface measurement system to improve radiotherapy treatment of cancer," Ph.D. thesis, Faculty of General Engineering (Liverpool John Moores University, 1999).
26. L. C. Fang and L. Yang "A new approach to high precision 3-D measuring system," Image Vis. Comput. **17**, 80514 (1999).

CHAPTER 4

EXPERIMENTAL STUDY ON WATER-WAVE TRAPPED MODES

This chapter presents the results arising from an experimental study on water wave trapped modes around an obstacle placed symmetrically between the walls of a water-wave channel. It is composed by a brief article published in *Europhysics Letters* [11] and a second, more detailed article currently under consideration for publication in the *Journal of Fluid Mechanics*.

The first section of this chapter is mainly concerned with the most important and striking results of this study, namely the occurrence of the trapped modes and their eigenfrequency dependence with the geometrical parameters of the problem. Complementarily, a more extensive thorough exposition of the results obtained in this study is carried out in the following sections, where the detailed spatial structure of these modes is discussed and a comparison is established between our experimental results and the available theoretical predictions of linear theory.

Trapped modes correspond to localized oscillations in unbounded media, and have been observed and studied in many domains of physics, such as acoustic waves, electromagnetic waves, elastic waves and water waves. According to the context in which trapped modes are studied, they are often termed differently, receiving names such as acoustic resonances, Rayleigh–Bloch waves, edge waves and bound states. In any case, they can be mathematically defined as finite energy solutions to the appropriate wave equation in an infinite domain with discrete eigenvalues embedded in the continuous spectrum of the problem. In this sense, trapped modes have to be distinguished from scattering states whose eigenvalues are located in the continuous spectrum and have infinite energy. From a physical standpoint, trapped modes consist on non-propagative localized oscillation modes of finite energy occurring at some well-defined frequency and which, in the absence of dissipation, would persist in time even in the absence of external forcing.

Experimentally, trapped modes turn into 'quasi-trapped' modes that can be evidenced by scattering resonances. The difference between the two is due to the ever-present deviations in the experiments with respect to the theoretical configuration for which predictions have been made. In this case, those deviations are linked mainly to two factors: the finite-size effect producing non-negligible radiation towards infinity and energy leaking due to the presence of dissipative mecha-

nisms.

Nevertheless, these practical limitations do not cloud the growing interest of the scientific community in trapped modes, mainly driven by their potential for technological applications. For instance, the high quality factors associated to trapped mode resonances are decisive for the effective design of metamaterials whose defining properties, such as negative refraction and cloacking, rely on the resonant nature of their response.

The case of water waves treated in this chapter is, amongst the many physical situations giving rise to trapped modes, of particular relevance for a variety of reasons. In the first place, water wave resonances are naturally important to practical applications in naval and coastal engineering. Moreover, as water waves exhibit properties similar to electromagnetic and microwaves, effects such as negative refraction and cloacking are also observable within their framework. In light of this similarity, water waves are attractive since the wave field is the free surface deformation, already qualitatively accessible to the naked eye.

In marked contrast to the large number of theoretical studies concerned with existence proofs and numerical algorithms for the computation of trapped modes for different geometries, little attention apears to have been paid to their experimental observation, characterisation and analysis. More precisely, only one experimental study was reported for the present problem [86], but due to the single-point nature of the employed measuring technique, no information was available on the spatial structure of these modes, therefore no measure of the degree of localization of the modes could be derived.

In this experimental study, we consider water wave trapped modes occurring in the vicinity of a vertical surface-piercing circular cylinder of radius a placed symmetrically between the parallel walls of a long water wave channel of width $2d$ and constant depth h. Within this physical system, a trapped mode is evidenced by the presence of a non-propagative local oscillation of the free surface confined to the vicinity of the cylinder. The frequency of this oscillation, termed trapped mode frequency, depends on the geometry of the system.

It is worth noting that the trapped modes associated with this configuration (and therefore, the results of the subsequent study) are also of interest to acoustics resonances in waveguides or bound states in quantum wires, as they also describe resonances associated with a two-dimensional waveguide governed by the Helmholtz equation, after the depth dependence has been separated.

One of the caracteristic properties of waveguides is the occurrence of cut-off frequencies. In particular, for motions that are antisymmetric about the longitudinal centreline of the guide, the waveguide presents a cut-off for propagation, *i.e.*, a threshold frequency (corresponding to $kd = \pi/2$) beneath which no wave *propagation* is possible. As a consequence, inside the waveguide, antisymmetric[1] perturbations characterized by values of $kd < \pi/2$ can only exist in the form of *evanescent* waves. This is the key feature that enables the existence of trapped modes. Indeed, if (in the absence of dissipation) an antisymmetric perturbation with a frequency below the cut-off is excited inside the waveguide, such oscillation will remain 'trapped' inside, its escape being forbidden by the impossibility to propagate down the guide. Moreover, the presence of a finite obstacle inside the guide introduces a change in the geometry of the waveguide, drastically affecting the propagation conditions in its vicinity. In that region, even though its amplitude is weak, the evanescent wave is able to interact with the obstacle.

[1] Herein, and unless explicitly stated otherwise, symmetry statements are to be understood with respect to the longitudinal centerline of the waveguide.

The ideas presented in the last paragraph hold the principle to the experimental strategy employed in this study to excite and observe the associated trapped modes. Acording to this scheme, the whole waveguide–obstacle system is placed inside a larger wave tank. A monochromatic wavemaker, inclined with respect to the channel's centerline, is employed to send an harmonic perturbation of a definite frequency (below the cut-off) containing both a symmetric (propagative) an antisymmetric (evanescent) component into the waveguide. When excited at the appropriate frequency, the antisymmetric perturbation will be amplified in the vicinity of the obstacle leading to a large amplitude oscillation of the free surface in that region. This is essentially equivalent to a resonance study, in which the system's response to an external driving is characterized within a given range of frequencies.

There exists, however, a qualitative difference between this case and the usual resonance analysis that is worth highlighting. In the framework of this problem, the perturbation of interest (giving rise to trapped modes) is instrinsically an *evanescent* water wave, often considered in theoretical studies but for the most part discarded in experimental investigations due to the difficulties associated with their measurement. Accurately measuring this low-amplitude evanescent wave is particularly demanding on the experimental technique, specially when considering far-off-resonance states of the system, in which wave amplitudes are smallest.

The relevant quantities in the characterisation of the trapped mode resonances for the problem under study are the aspect ratio a/d and the dimensionless frequency parameter kd, where k is the positive real root of the dispersion relation given by $\omega^2 = gk\tanh kh$, and ω denotes the modal wave angular (driving) frequency. In this configuration, a significative number of values of the geometrical control parameter a/d were examined. For each of the aspect ratios considered, a wide range of frequencies around the theoretical trapped mode eigenfrequency was explored.

For a given driving frequency, space-time resolved measurements of the free surface deformation inside the waveguide were obtained by means of our optical profilometry technique, employing a high-speed camera to record high-resolution images at an acquisition rate 100 times larger than the driving frequency. In our measurements, the free surface region inside the waveguide, of size 10×40 cm^2, was sampled at over 680 000 points. This allowed us to properly quantify the total deformation field, composed of both symmetric (propagative) and antisymmetric (evanescent) contributions.

Analysis of the total deformation fields led us to the observation of an *asymmetric* oscillation well localized in the region near the cylinder, with amplitudes that largely exceed that at the waveguide's entrance, indicating an amplification of the perturbation. Far from the cylinder, to the contrary, our results show only the propagation of a plane, slightly attenuated wave. The rapid recovery of symmetry observed in this region is consistent with the occurrence of a trapped mode of high degree of localisation. Nevertheless, the pure antisymmetric form which is characteristic of the trapped mode is still concealed by the plane wave propagating down the guide.

Taking advantage of the space-time resolved nature of our measurements, we were able to perform a decomposition of the free surface deformation in harmonics of the driving frequency for every (sampled) point over the surface. This allowed the separate analysis of the linear (at the driving frequency) and non-linear components of the total free-surface deformation. A comparison showed that the dynamics of the free surface is dominated by the linear contribution, validating the use of theoretical models based on classical linear wave theory. This also allowed us to concentrate on the linear part of the deformation field, to which existing theoretical results can be contrasted.

One of the most significant results of this study came from the subsequent separation of the linear deformation field in terms of the symmetries of the problem. Such separation allowed us to obtain the full trapped modes' spatial structure, isolated from any other contribution. This constitutes, to our knowledge, the first time that the existence of trapped modes in water waves is experimentally evidenced through the spatial pattern of the purely antisymmetric free-surface deformation.

The spatial structure of the trapped mode was studied in detail and succesfully compared to theoretical predictions arising from a multipole expansion method. Moreover, the analysis of the spatial structure led us to the identification of two different types of trapped modes: one that is antisymmetric about the longitudinal axis of the channel but symmetric with respect to the other axis (termed 'Neumann-symmetric' or NS-trapped mode in the literature) and another that is antisymmetric with respect to both axis (called 'Neumann-antisymmetric or NA-trapped mode). The occurrence of both NS- and NA- trapped modes (at, of course, two different frequencies) was numerically predicted only for aspect ratios satisfying $a/d \gtrsim 0.81$; lower values of this parameter being only associated with a NS-type trapped mode. The range of values of the aspect ratio a/d for which this second type of trapped mode was observed in our experiences confirms those predictions.

Precise determination of the trapped modes eigenfrequencies is achieved by treating the system as a scattering problem in the far field. To this end, one-dimensional reflection and transmission coefficients are defined, allowing for the construction of resonance curves which characterize the frequency behaviour of the modes. In these curves, the presence of a trapped mode is evidenced by the presence of a peak. Only for the largest aspect ratios a/d these curves show two peaks, the second one corresponding to NA-type trapped modes. This is consistent with the previously discussed observation of NA-type trapped modes when analysing the spatial structure of the modes.

The marked asymmetry of the resonant curves, which cannot be adequately described by the classical Breit-Wigner formula, constitutes an interesting feature. Having checked numerically this behaviour, we propose a model for the frequency dependence of the scattering data, influenced by the proximity of the threshold for propagation of the waveguide. This model allowed us to theoretically reproduce the asymmetry of the resonance curves, and was successfully validated with the experimental results.

Finally, all the results of the present study are summarized in a master curve showing the dependence of the trapped mode frequency parameter kd with the aspect ratio a/d. This curve is, as expected, composed by two branches, corresponding to NS- and NA- type trapped modes. Comparison to theoretical predictions available within the frame of the linear theory show excellent agreement for both branches.

Incidentally, the case for which the cylinder's diameter coincides with the waveguide's width, namely $a/d = 1$, is of particular interest as no theoretical predictions are available. In this case, our results show that the trapped mode becomes and edge mode, corresponding to the degeneracy of the symmetric and antisymmetric trapped modes and thus to the intersection of the two branches of resonance.

The experimental study presented in this chapter constitutes a significative advance in the understanding trapped modes in water waves. It is the first one to provide a complete characterization of both NS- and NA-type trapped modes in frequency space, as well as to present a detailed analysis of their spatial structure.

Experimental observation of trapped modes in a water wave channel

P. J. Cobelli[1], V. Pagneux[2], A. Maurel[3] and P. Petitjeans[1]

[1] *Laboratoire de Physique et Mécanique des Milieux Hétérogènes, UMR CNRS 7636, Ecole Supérieure de Physique et Chimie Industrielles, Paris – France.*
[2] *Laboratoire d'Acoustique de l'Université du Maine, UMR CNRS 6613, Université du Maine, Le Mans – France.*
[3] *Laboratoire Ondes et Acoustique, Institut Langevin, UMR CNRS 7587, Ecole Supérieure de Physique et Chimie Industrielles, Paris – France.*

PACS 03.65.Ge – Solutions of wave equations: bound states
PACS 43.20.Ks – Standing waves, resonance, normal modes
PACS 47.35.Lf – Wave-structure interactions

Abstract. - The fluid around a free surface piercing circular cylinder in a long narrow wave tank can exhibit a local oscillation that does not propagate down the channel but is confined to the vicinity of the cylinder. This is a manifestation of the so-called trapped modes, bound states in the continuum occurring in many situations in physics. In this Letter, using Fourier Transform Profilometry, fully space time resolved measurements for the free surface deformation are obtained. The scattering characteristics of the cylinder and consequently the behavior of the trapped mode frequency are determined.

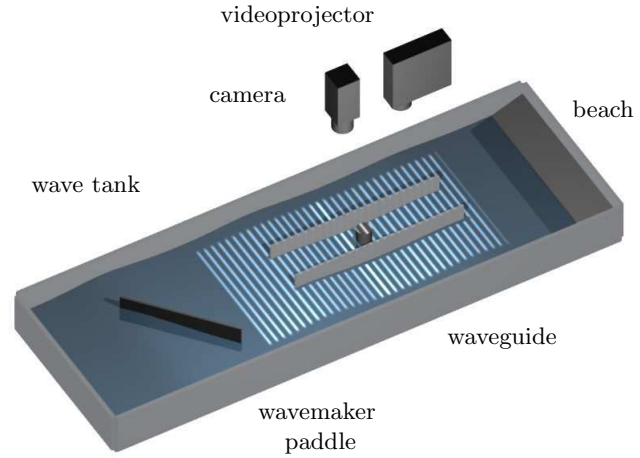
Trapped modes have been studied in many domains of physics (for a review, see [1]), elastic waves [2, 3], water waves [4–8] or electromagnetic waves [9, 10]. They are finite energy solutions to the wave equation in infinite domain with discrete eigenvalues embedded in the continuous spectrum. Trapped modes have to be distinguished from scattering states whose eigenvalues are in the continuous spectrum and that have infinite energy. Experimentally, trapped modes turn into quasi trapped modes that can be evidenced by scattering resonances. This is due to deviations in the experiments with respect to the theoretical configuration: finite size effect producing radiation toward infinity or leaking due to dissipative mechanisms. However, the study of quality factors of the trapped mode resonances is of interest. Indeed, high quality factors in trapped mode resonances are decisive for the design of metamaterials, whose remarkable properties, such as negative index or cloaking, are underpinned by the resonant nature of their response.

Among the physical situations giving rise to trapped mode resonances, the case of water waves is of particular interest. Firstly, water wave resonances have many practical applications in naval and coastal engineering [11, 12]. In addition to their own interest, water waves exhibit similar properties as electromagnetic and microwaves, *e.g.* negative refraction or cloaking [13–15]. From that point of view, water waves are attractive since the wave field is the free surface deformation, that is already qualitatively accessible to the naked eye.

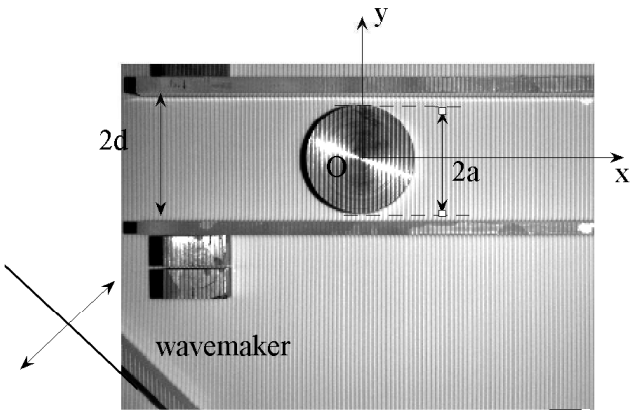
In this Letter, we study experimentally the trapped mode resonances of water waves interacting with a cylindrical obstacle in a waveguide. This configuration has been studied in linearized water wave theory by [4–7] and very few experimental results are available [16]. Also, it corresponds to the problem of an infinite set of cylinders where strong resonances have been numerically observed [12].

Owing to Fourier Transform Profilometry [17–19], we get a resolution of the surface elevation in time and in space able to quantitatively describe the trapped mode resonances, by means of their patterns and by means of the reflection and transmission coefficients. A model for the frequency dependance of the scattering data, influenced by the proximity of the threshold for propagation, is proposed and compared favorably with the experimental results.

Our experimental set-up consists of a water tank with constant water level at rest which is chosen to be fixed at $h_0 = 5$ cm. The system of interest is placed inside the



(a) scheme of the complete experimental setup



(b) camera's view

Fig. 1: Experimental setup (a). Symmetric and antisymmetric modes are generated at the entrance of the waveguide by the wavemaker. A free surface piercing circular cylinder of diameter $2a \in [2, 10]$ cm lies in the center of the waveguide of width $2d = 10$ cm. The measurement is performed using an optical method (Fourier Transform Profilometry). A videoprojector projects fringes onto the free surface and the image is collected by a camera. Analysis of the fringe displacements allows for the reconstruction of the surface deformation at each pixel. Panel (b) presents a sample of the camera's view showing the free surface and the projected fringes, the waveguide, the cylinder, and a portion of the wavemaker paddle.

tank: a waveguide formed by two parallel vertical walls, 60 cm long, a distance $2d = 10$ cm apart, has a free surface piercing vertical circular cylinder of diameter $2a$ ($a = 1$ to 5 cm) located symmetrically between the two walls (Fig. 1). Water waves are generated by a wave maker forming an angle of around 45° with the waveguide axis Ox (so symmetric and antisymmetric modes are generated at the entrance of the waveguide) at a frequency $f \in [2, 3]$ Hz.

An important specificity in our experiment is the measurement of the surface elevation. This optical method, termed Fourier Transform Profilometry, is originally due to [17] and has been described in [18, 19] for application to water wave measurements. By projecting fringes onto the free surface and by analyzing the fringe displacement, we are able to deduce the surface elevation in the working window. In the present experiment, the window is 40×10 cm^2 corresponding to 1623×421 pixels^2. The width of the pixel, 0.23 mm, sets the spatial resolution and the resolution on the surface elevation. The temporal resolution is only limited by the acquisition rate of the camera since a single picture is needed to get the measurement. In our experiment, a high speed camera is used with an acquisition rate close to 300 Hz.

Typical free surface deformation fields $h_T(x, y, t)$ near resonance are shown in Fig. 2. The acquisition rate of the camera is synchronized with the wavemaker in order to get 200 acquisitions $h_T(x, y, t)$ over two periods of the water wave oscillation. For a perfect fluid, in absence of dissipation, the dispersion relation for the water waves is given by $\omega^2 = gk \tanh kh_0$ where ω is the driving pulsation, k the wavenumber and $g = 9.81$ m.s^{-2}. For the purposes of this study, the effects of surface tension will be neglected.

A first direct qualitative evidence of the resonance phenomenon can already be obtained from these instantaneous fields. The symmetry of the geometry decouples the fields into two families, even and odd with respect to y. The wave is always propagative for the first family while it has a non zero cut on frequency for the second family. This latter gap property enables the existence of the trapped mode [20]. Fig. 3 shows the odd family, $[h_T(x, y, t) - h_T(x, -y, t)]/2$, for some given y and t as a function of x and ω. Typical spots are visible that are indicative of the presence of resonances.

In order to obtain quantitative characterics of the resonance, we extract, at each position, the coefficient $h_1(x, y)$ of the Fourier series

$$h_T(x, y, t) = \sum_n h_n(x, y) e^{in\omega t}. \qquad (1)$$

This is achieved owing to the large sampling rate offered by the camera. In our experiment, the weight of the non linearities $|h_T - h_1|/|h_T|$ is less than 15 %. h_1 is then separated into an even part h^e and an odd part h^o. Fig. 4 depicts the typical situation near resonance: the trapped mode is isolated in the odd part of the field and is localized in the vicinity of the cylinder. Depending on the geometry, it is either symmetric with respect to the vertical axis, as predicted in Ref. [20] or antisymmetric with respect to the vertical axis as predicted in Ref. [21]. This latter trapped mode is expected to exist only for $a/d \gtrsim 0.81$ [21], what we experimentally confirm. The even field h^e makes the propagative plane mode to appear. This field is used to get a direct measurement of the wavenumber k. The agreement with the theoretical dispersion relation is of about 2 %.

To go further, we want to get a 1D model. With a constant water level at rest h_0, the free surface el-

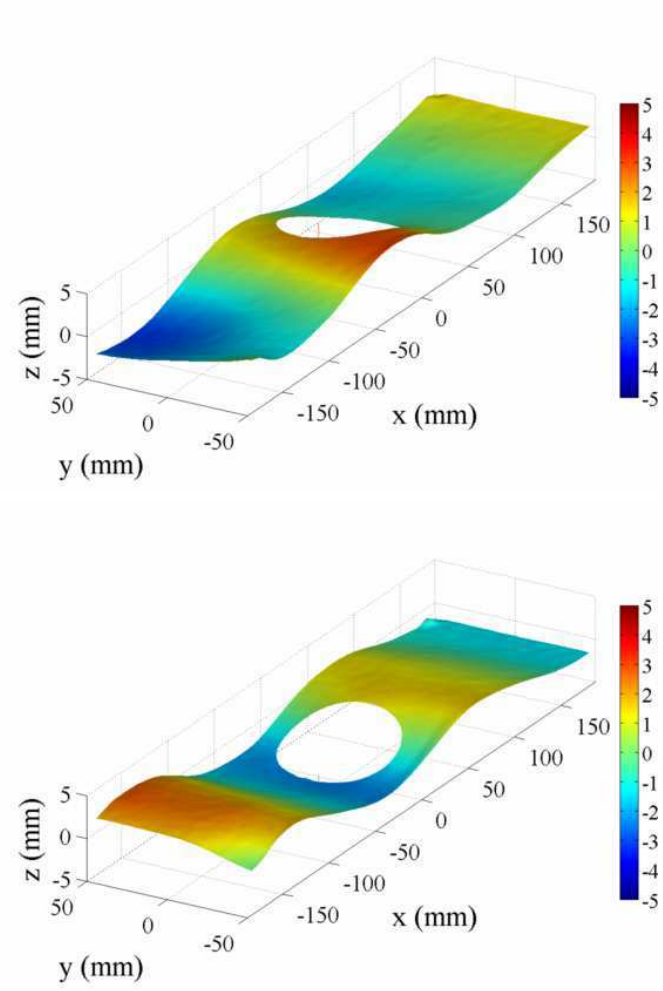


Fig. 2: Typical instantaneous fields of the surface elevation $h_T(x, y, t)$, here for $a/d = 0.50$, $kd = 1.32$. The scale of the colorbar is in mm.

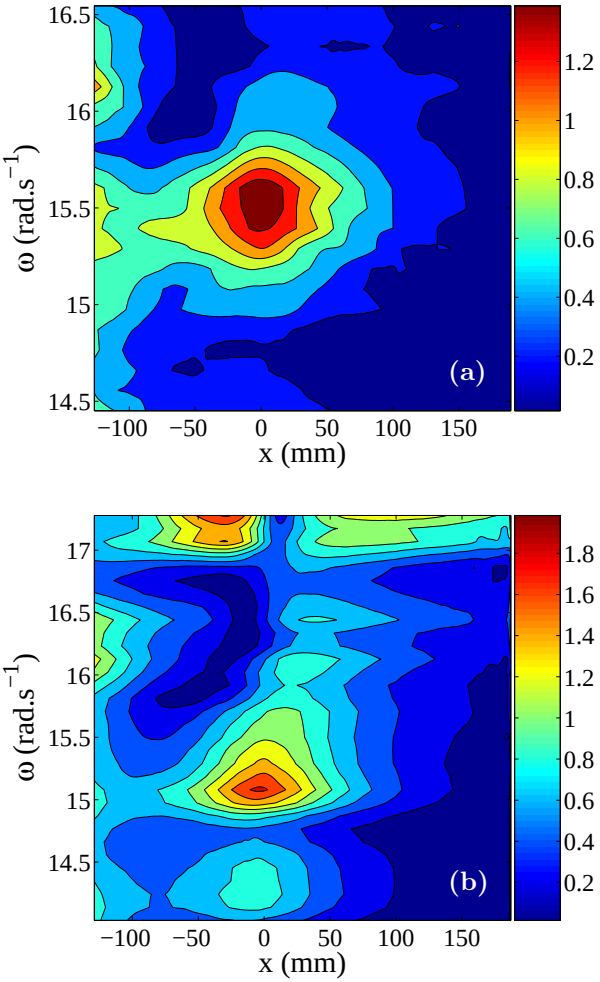


Fig. 3: Evidence of the trapped mode resonances: $(h_T(x, y, t) - h_T(x, -y, t))/2$ for some fixed y is displayed in colorscale as a function of x and ω. (a) for $a/d = 0.50$, one resonance is visible near the cylinder and (b) for $a/d = 0.85$, in addition to the first resonance, a second maximum near the cutoff frequency can be seen (the cylinder lies at $x = 0$). The scale of the colorbar is in mm.

evation $h_1(x, y)$ is governed by the Helmholtz equation $(\Delta + k^2)h_1(x, y) = 0$, with Neumann boundary condition at the walls, where k is given by the aforementioned dispersion relation [22]. Then, in our analysis, the odd part $h^o(x, y)$ of the field $h_1(x, y)$ is modelized in a 1D problem by projecting the 2D field onto the first transverse mode:

$$h^o(x, y) \simeq h(x) \sin \pi y/2d, \tag{2}$$

outside of the near field of the cylinder (Fig. 5(a)). In the near field, the higher transverse modes are expected to contribute to the 2D solution. However, the contribution of the higher order modes [with $\sin(2n + 1)\pi y/2d$, $n \neq 0$ dependance] is less than 7% in our experiments. The typical behavior of $h(x)$ is shown in Fig. 5(b). Because we are working below the first cutoff frequency, at $\pi/(2d)$, for antisymmetric modes, the solution is sought as

$$\begin{aligned} h(x < 0) &= A\, e^{-\alpha x} + AR\, e^{\alpha x}, \\ h(x > 0) &= AT\, e^{-\alpha x}, \end{aligned} \tag{3}$$

with A the amplitude of the incident wave, α the wavenumber of the first evanescent mode and (R, T) the reflection and transmission coefficients. Such behavior is illustrated in Fig. 5.

The reflection and transmission coefficients (R, T) and α are fitted for each frequency outside the near field region. The resonance curves are obtained, as exemplified in Fig. 6 for $a/d = 0.50$ (the single resonance corresponds to a trapped mode as in Fig. 4(b)) and for $a/d = 0.85$ (the two resonances correspond to the two types of trapped modes in Fig. 4(b)(d)).

As is evident from these curves, the classical Breit-Wigner resonance shape is not well suited as it would be unable to reproduce their clear asymmetry. We have checked that this asymmetry is not an experimental artifact by computing the transmission and reflection coefficients numerically (numerical calculations have been per-

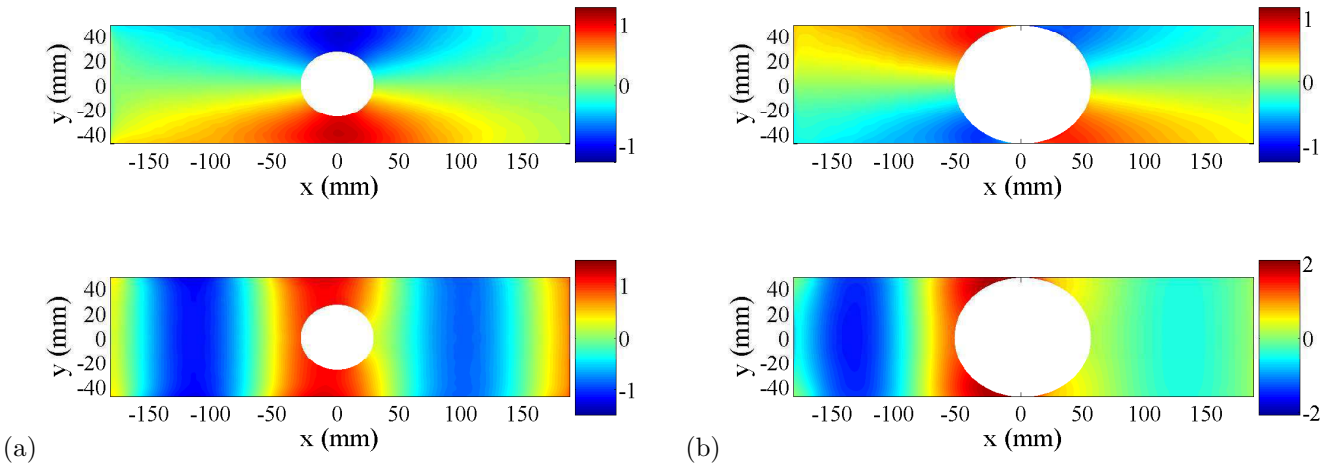


Fig. 4: Experimental patterns of the two trapped modes, and the associated even parts. (a) even and odd fields of the linear field $h_1(x, y)$, for $a/d = 0.40$ and $kd = 1.46$. The even part exhibits the form of the trapped mode localized in the vicinity of the cylinder. (b) Same representation for $a/d = 0.95$ and $kd = 1.51$. The scale of the colorbar is in mm.

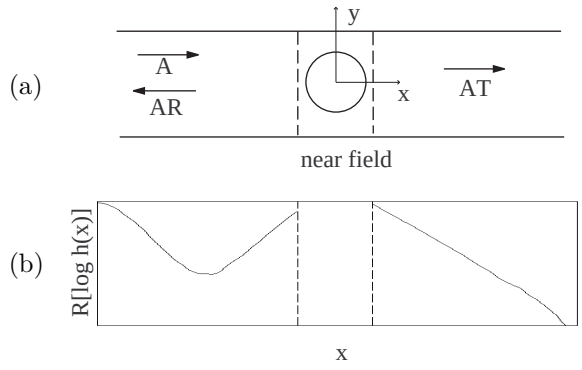


Fig. 5: Top: The problem reduces to a 1D problem along the x-axis, by projecting the odd field onto the first transverse mode in $\sin \pi y/2d$ outside the near field region. Bottom: Typical variation of the measured $h(x)$ along the x-axis: real part of $\log[h(x)]$ as a function of x (a.u.) (the curve has been obtained for $a/d = 0.4$, $kd = 1.47$).

formed using the toolbox PDEtool of Matlab; see [23]). The 1D transmission and reflection coefficients are actually influenced by the proximity of the cut-off frequency at $kd = \pi/2$. It has been already observed for confined states in bent waveguides in [24] that proposed the following asymmetric shape for T

$$T = \frac{B}{1 - C/(\alpha d)}, \qquad (4)$$

where $\alpha d \equiv \sqrt{(\pi/2)^2 - (kd)^2}$. This equation has to be understood in the neighbourhood of the resonance in the complex plane. The constants B and C have been numerically computed and we have checked that the Eq. (4) is valid in the complex k-plane. Note that (B, C) are functions of the geometry only. For $a/d = 0.50$, we have found $B = 1.15$ and $C = 0.73$. For $a/d = 0.85$, there are two resonances and the transmission coefficient can be written as the sum of two shapes Eq. (4) with (B_1=1.85, C_1 = 0.8325) and (B_2 = -1.2, C_2 = 0.135).

In the experiment, a small attenuation is present that is modelized by a small imaginary part of k. This attenuation can only be roughly evaluated, because of a low signal to noise ratio on the imaginary part of α. The experimental measurements of α gives, through the relation $k = \sqrt{(\pi/2d)^2 - \alpha^2}$, an estimation of $\mathrm{Im}(k)d \sim 0.03$.

As shown in Fig. 6, a good agreement is observed between the experiments and the prediction of Eq. (4). For the case $a/d = 0.50$ in Fig. 6(a), a constant attenuation $\mathrm{Im}(k)d = 0.025$ has been used, a value consistent with our rough experimental estimate. For the case $a/d = 0.85$ in Fig. 6(b), the second resonance is visible, a fact that can be reproduced only assuming a significant decrease in the attenuation from $\mathrm{Im}(k)d = 0.033$ near the first resonance to 0.003 near the second resonance.

The behavior of the resonance frequency $k_c d$ when changing the size of the cylinder is shown in Fig. 7. There are two branches: the first corresponds to trapped modes symmetric with respect to Oy-axis and the second to trapped modes antisymmetric with respect to Oy-axis.

The experimental results are compared to the theoretical predictions of Ref. [20] for the first branch and with the theoretical predictions of Ref. [21] for the second branch. The authors in [21] predicted that the resonances of the second branch exist for $a/d \gtrsim 0.81$. This prediction is confirmed here. An excellent agreement is observed with the theoretical predictions for both branches. It is worth noting that this is the case even for the largest values of

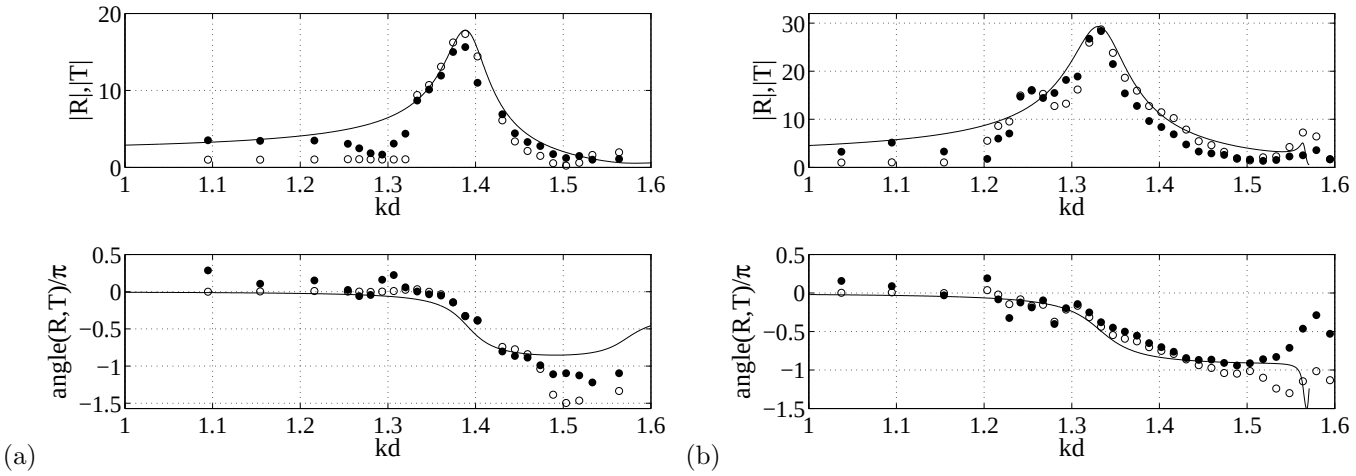


Fig. 6: Resonance curves for (a) $a/d = 0.50$ and (b) $a/d = 0.85$, upper panel $|R|$ (plain circle), $|T|$ (open circle) as a function of the wavenumber kd. Lower panels show the corresponding phases. Plain lines correspond to the results obtained from numerical calculations, indiscernible from the expression in Eq. (4).

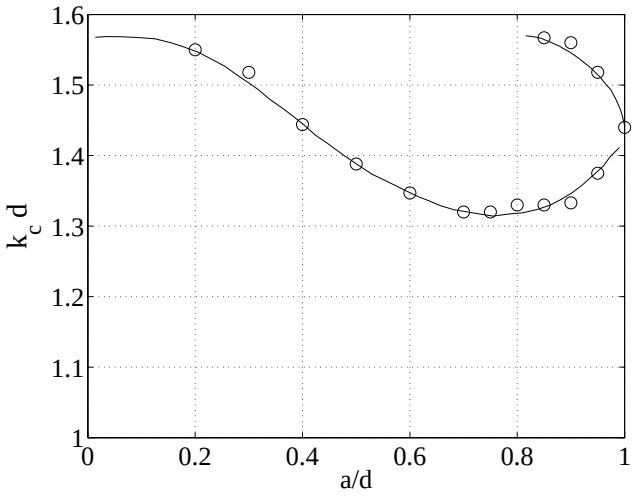


Fig. 7: Resonance frequencies $k_c d$ as a function of a/d. Open circles are the experimental values deduced from the resonance curves and plain lines are the theoretical predictions from [20, 21].

a/d, for which the effect of a meniscus in the small region between the cylinder and the waveguide walls would seem important. This validates our assumption of negligible effects due to surface tension.

The case of the totally obstructing cylinder $a/d = 1$ deserves closer inspection. In this case, the trapped mode becomes an edge mode. It corresponds to the degeneracy of the symmetric and antisymmetric trapped modes and thus to the intersection between the two branches of resonance in Fig. 7. Experimentally, the resonance frequency of the edge mode is found at $kd = 1.44$. The corresponding pattern of the edge mode is shown in Fig. 8.

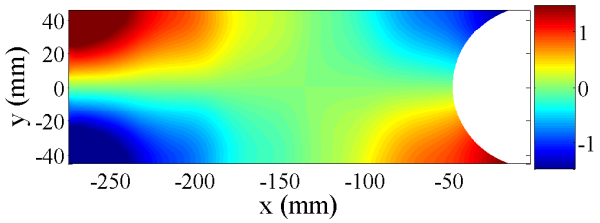


Fig. 8: Edge mode experimentally observed for $a/d = 1$ and $kd = 1.44$. The scale of the colorbar is in mm.

* * *

This work is supported by the ANR project ANR-08-BLAN-01108 Tourbillonde.

REFERENCES

[1] C. M. Linton and P. McIver, *Wave Motion* **45** 16-29 (2007).
[2] J. D. Kaplunov and S. V. Sorokin, *J. Acoust. Soc. Am.* **97** 3898-3899 (1995).
[3] V. Pagneux, *J. Acoust. Soc. Am.* **120** 649-656 (2006).
[4] D.S. Jones, *Proc. Camb. Phil. Soc.* **49** 668684 (1953).
[5] F. Ursell, *J. Fluid Mech* **183** 421-437 (1987).
[6] P. Mc Iver, *Q. J. Mechanics Appl. Math.* **44**(2) 193-208 (1991).
[7] D.V. Evans and C. M. Linton, *J. Fluid Mech.* **225** 153-175 (1991).
[8] N.F. Parsons and P.A. Martin, *J. Fluid Mech.* **284** 359-375 (1994).
[9] S.S. Kurennoy *Phys. Rev. E* **51** 2498-2509 (1995).
[10] V. A. Fedotov, M. Rose, S. L. Prosvirnin, N. Papasimakis, and N. I. Zheludev *Phys. Rev. Lett.* **99** 147401 (2007).
[11] D.V. Evans and R. Porter, *Appl. Ocean Res.* **19** 83-89 (1997).

[12] G. Duclos and A.H. Clement, *Ocean Eng.* **31** 1655-1668 (2004).
[13] X. Hu, Y. Shen, X. Liu, R. Fu and J. Zi, *Phys. Rev. E* **69** 030201 (2004).
[14] X. Hu and C.T. Chan, *Phys. Rev. Lett.* **95** 154501 (2005).
[15] M. Farhat, S. Enoch, S. Guenneau and A.B. Movchan, *Phys. Rev. Lett.* **101** 134501 (2008).
[16] C.H. Retzler, *Appl. Ocean Res.* **23** 249-250 (2001).
[17] M. Takeda and K. Mutoh, *Appl. Opt.* **22** 39773982 (1983).
[18] A. Maurel, P. Cobelli, V. Pagneux and P. Petitjeans, *Applied Optics*, **48**(2) 380-392 (2009).
[19] P. Cobelli, A. Maurel, V. Pagneux and P. Petitjeans, *Experiments in Fluids* **46** 1037-1047 (2009).
[20] M. Callan, C.M. Linton and D.V. Evans *J. Fluid Mech.* **229** 51-64 (1991).
[21] D.V. Evans and R. Porter *J. Eng. Math.* **35** 149-179 (1999).
[22] C. M. Linton and P. McIver, Handbook of Mathematical Techniques for Wave/structure Interactions, CRC Press (2001).
[23] The numerics has been performed using the toolbox PDEtool of Matlab. The equation is the Helmholtz equation $(\Delta + k^2)\phi = 0$, with vanishing normal gradient on the cylinder boundary and the lateral walls. The leading antisymmetric mode (with $\sin \pi y/2d$ transverse dependance) is imposed at the entrance. Then, the transmitted and reflected waves are collected in the far field of the cylinder.
[24] E. Granot, *Phys. Rev. B* **65** 233101 (2001).

Experimental study on water-wave trapped modes

P. J. COBELLI[1], **V. PAGNEUX**[2], **A. MAUREL**[3] **AND P. PETITJEANS**[1]

[1] Laboratoire de Physique et Mécanique des Milieux Hétérogènes, UMR CNRS 7636, Ecole Supérieure de Physique et de Chimie Industrielles, 10 rue Vauquelin, 75231 Paris Cedex 5, France

[2] Laboratoire d'Acoustique de l'Université du Maine, UMR CNRS 6613, Avenue Olivier Messiaen, 72085 Le Mans Cedex 9, France

[3] Laboratoire Ondes et Acoustique, Institut Langevin UMR CNRS 7587, Ecole Supérieure de Physique et de Chimie Industrielles, 10 rue Vauquelin, 75231 Paris Cedex 5, France

(Received 12 October 2009)

We present an experimental study on the trapped modes occurring around a vertical surface-piercing circular cylinder of radius a placed symmetrically between the parallel walls of a long but finite water waveguide of width $2d$. A wavemaker placed near the entrance of the waveguide is used to force an asymmetric perturbation into the guide, and the free-surface deformation field is measured using a global single-shot optical profilometric technique. In this configuration, several values of the aspect ratio a/d were explored for a range of driving frequencies below the waveguide's cutoff. Decomposition of the obtained fields in harmonics of the driving frequency allowed for the isolation of the linear contribution, which was subsequently separated according to the symmetries of the problem. For each of the aspect ratios considered, the spatial structure of the trapped mode was obtained and compared to the theoretical predictions given by a multipole expansion method. The waveguide–obstacle system was further characterized in terms of reflection and transmission coefficients, which led to the construction of resonance curves showing the presence of one or two trapped modes (depending on the value of a/d), a result that is consistent with the theoretical predictions available in the literature. The frequency dependency of the trapped modes with the geometrical parameter a/d was determined from these curves and successfully compared to the theoretical predictions available within the frame of linear wave theory.

1. Introduction

In the framework of the classical theory of linearized water waves in unbounded domains, trapped modes consist of non-propagative localized oscillation modes of finite energy occuring at some well-defined frequency and which, in the absence of dissipation, persist in time even in the absence of external forcing.

The first theoretical example of such trapping mode in the theory of water waves, due to Stokes (1846), consists on waves which travel in the long-shore direction over a uniformly sloping beach and decay to zero in the seaward direction. Such a trapped mode has often been referred to as an edge wave, as in this case the energy remains trapped near the shore. (Note that, in this case, finite energy is to be understood in terms of energy

per unit length along the shore). These localized modes were later generalized by Ursell (1952) to an infinite set of discrete modes, of which Stokes' edge waves represent the fundamental mode. For a recent review on edge waves, the reader is referred to Johnson (2007) and references therein. Field observations of edge waves have been reported by Huntley & Bowen (1973). For a description of edge waves in an oceanographic context, the reader is referred to the work by LeBlond & Mysak (1978).

Ursell (1951) showed that such a trapped mode could also exist in the vicinity of a long submerged horizontal circular cylinder, in the form of waves travelling along the cylinder and decaying in a direction normal to the cylinder axis. Although the original proof given by Ursell (1951) was restricted to sufficiently small cylinders (*i.e.*, of radius smaller than the wavelength), Jones (1953) showed that the nature of this restriction was not physical. Indeed, employing a general treatment based on the theory of elliptic partial differential equations in unbounded domains, this latter author proved that trapped modes exist for a submerged horizontal cylinder of symmetric but otherwise arbitrary cross-section, both in finite and infinite depth. Finally, a proof based on Kelvin's minimum-energy theorem was provided by Ursell (1987) for the existence of trapped modes in the case of a totally submerged body without any restriction on its shape and size. Moreover, in a numerical study, McIver & Evans (1985) showed that there is always at least one trapped mode above a cylinder of arbitrary size and that further modes are possible as the top of the cylinder approaches the free surface.

More importantly, Jones' work proved the existence of trapping modes for problems governed by the Helmholtz equation in semi-infinite domains, indicating that such bound states could occur (under certain conditions) in other contexts such as, *e.g.*, acoustics. Evans & Linton (1991) described a constructive method for determining trapped mode frequencies in two specific problems not covered by Jones' theory in which the two-dimensional Helmholtz equation is satisfied. One of these problems involves the free-surface fluid motion in a long waveguide containing a vertical cylinder of uniform cross-section placed symmetrically between its walls and extending throughout the water depth. In this case, separation of the depth dependance leaves out the Helmholtz equation and the dispersion relation linking the wavenumber and the wave frequency, required to satisfy the linearized free-surface condition for water waves. Neumann boundary conditions on the walls set a threshold for the propagation of perturbations which are antisymmetric with respect to the waveguide's centerplane. Below this cutoff frequency, antisymmetric waves cannot propagate, though they may still exist within the guide in the form of evanescent waves. Although trapped mode solutions, localized within the waveguide and having bounded total energy are not possible below this cutoff, Evans & Linton (op. cit.) showed that the presence of a symmetrically placed rectangular block satisfying a no-flow condition on its sides and having two sides parallel to the waveguide walls enabled the construction of such solutions, and computed their frequencies. These modes are characterized by having finite total energy, being localized in the vicinity of the obstacle and decaying rapidly to zero with distance down the waveguide. Moreover, the number of such modes increases with the length of the block; conversely, only a single mode exists for a block shorter than the channel's width. This work provided numerical evidence as well as a criterion as to when to expect such modes to occur for this class of problems and how to compute them.

McIver (1991) derived the trapped mode frequency for antisymmetric trapped modes in the vicinity of a vertical cylinder of arbitrary but small cross-section in a water channel of infinite extent. Similar results were obtained by Evans & McIver (1991) for the trapped mode frequency close to the cutoff, for the particular case of symmetric thin bodies.

Callan *et al.* (1991), employing a method due to Ursell (1951), proved the existence of

a trapped mode for a cylinder of sufficiently small radius placed symmetrically within the guide. Furthermore, an explicit relation between the cylinder radius, the waveguide width and the trapped mode frequency was found in this particular case. However, numerical computations revealed that a single trapped surface wave mode exists irrespective of the cylinder size. Moreover, it was also shown that, in the general case, the frequency of the trapped mode oscillation lies below the fundamental cutoff frequency for the channel and depends only upon the ratio of cylinder radius to waveguide width. This trapped mode, having a frequency close but below the fundamental cutoff frequency of the channel, is characterized by being antisymmetric about the centerplane of the guide and symmetric about a line perpendicular to the waveguide's walls passing through the cylinder axis (hereafter termed Neumann–symmetric, or NS-trapped modes). However, no trapped modes antisymmetric about both lines (Neumann–antisymmetric, or NA-trapped modes) were found in this study.

In relation to this problem, Linton & Evans (1992) constructed a homogeneous integral equation for the trapped modes in the case of a cylinder of fairly general cross-section and showed that the trapped mode frequencies agreed numerically with the previous results for the circular cross-sections. Finally, Evans *et al.* (1994) showed that there is at least one trapped mode antisymmetric about the centerplane of the waveguide, localized near an obstacle of symmetric but otherwise fairly general shape about the centerline of the waveguide and decaying with distance down the guide away from the obstacle.

A few years later, Evans & Porter (1999) described a method for constructing trapped modes antisymmetric about the line through the centre of the cylinder and perpendicular to the channel walls (*i.e.*, NA-trapped modes). Their numerical computations of such modes established their existence for values of the control parameter in excess of a numerically determined threshold, corresponding to cylinders of radius 0.81 times larger than the waveguide's width.

It is worth noting that the studies cited above systematically neglect surface tension, so the question arises as to whether its effects might play a relevant role in the observation of trapped modes, and to whether it is physically realistic to exclude surface tension from the linear water wave problem. For the problem under consideration here, Harter *et al.* (2007) showed (choosing a particular contact-point condition) that the qualitative nature of the streamline shape is unaffected by the addition of surface tension in the free surface condition, no matter how large this parameter becomes.

In the last fifteen years, the study of trapped modes has largely developped and diversified. McIver (1996) was the first to construct a finite structure supporting a so-called 'sloshing' trapped mode, where the fluid motion is essentially confined to the region inside the surface-piercing structure. Modifications of the construction method employed by McIver (op. cit.) have now been used to build a variety of sloshing trapping structures in two and three dimensions, both submerged (see Evans & Porter 2002; McIver 2000; McIver & Porter 2002) and surface-piercing (see McIver & McIver 1997; Kuznetsov & McIver 1997; McIver & Newman 2003). Coupled oscillations between a freely floating structure and the surrounding fluid, termed 'motion trapped modes', were recently obtained by McIver & McIver (2006). As in the case of the sloshing trapping structures, these structures have two surface-piercing elements separated by a portion of the free surface. For more information regarding recents developments in the study of trapped modes, the reader is referred to the comprehensive review given by Linton & McIver (2007).

In the framework of the present experimental study, we will focus on the measurement

and analysis of trapped modes occuring around a vertical surface-piercing circular cylinder placed symmetrically between the parallel walls of a long but finite water waveguide.

The trapped modes associated to this configuration are also of interest to acoustics, as they also describe acoustic resonances associated with a two-dimensional acoustic waveguide containing a sound–hard (cylindrical) obstacle, by virtue of the separation of the depth factor in the water-wave problem.

Another aspect of interest regarding this particular configuration arises from the consideration of the Neumann (no-flow) boundary conditions at the waveguide walls. Indeed, neglecting the effects of the boundary layer, the walls can equally well be thought of as representing lines of symmetry. Hence these trapped modes also exist in the presence of an infinite linear array of regularly spaced obstacles, generating very large forces on the elements of the array (see Maniar & Newman 1997; Evans & Porter 1997*a*,*b*). Moreover, Evans & Porter (1999) showed that 'near-trapping' could occur between adjacent elements within a large but otherwise *finite* array of cylinders. In this case, it was found that the associated near-trapping frequencies are related to the Rayleigh–Bloch trapped-wave frequencies for the infinite array. (On the existence of Rayleigh–Bloch waves, see Linton & McIver 2002). In practice, the occurrence of near-trapped modes is of particular relevance to offshore structures based on a large number of piles (such as oil rigs, very-large floating structures and breakwaters) as it implies the presence of very large loads on individual elements of the array. Recent progress in the understanding of wave interaction with arrays of offshore structures, resonant effects and their consequences for finite arrays has been discussed by McIver (2002).

In marked contrast to the large number of theoretical studies concerned with existence proofs and numerical algorithms for the computation of trapped modes for different geometries, little attention appears to have been paid to their experimental observation, characterisation and analysis.

Indeed, the only experimental results available in the literature for the problem under study are due to Retzler (2001). In this work, the observation of trapped modes around a vertical surface-piercing circular cylinder placed symmetrically within the walls of an open channel was reported. The channel was 12.8 m long and 0.427 m wide; water depth was fixed at 0.7 m. The cylinder was given a step impulse perpendicular to the channel centerplane from an arbitrary rest position then held with its axis perpendicular to the waveguide's bottom. The transient free-surface disturbance was measured by means of two single-point wave-gauges placed symmetrically at either side of the cylinder, on a line perpendicular to the guide walls. Using this setup, three values of the control parameter (ratio of cylinder radius to waveguide's width) were explored, each of which was associated with a NS mode of sharply defined frequency within 0.4% of the predicted trapped mode frequency. However, due to the nature of their measuring technique, no information was available on the spatial structure of these modes, therefore no measure of the degree of localization of the modes could be derived. Moreover, the range of geometries explored precluded the observation of NA-type trapped modes.

The aim of this study is to gain further understanding regarding the occurrence of trapped modes of both NS- and NA-types, the dependence of their eigenfrequencies with geometry, and the characterization of their detailed spatial structure.

The paper is organized as follows. In the next section we describe the complete experimental setup employed in this study, along with the optical profilometric system devised for the measurement of the free surface deformation. Section 3 presents the experimental results concerning the detailed spatial structure of the trapped modes. Finally, Section 4 comprises the analysis and comparison of our experimental results with the theoretical predictions available within the frame of the linear theory.

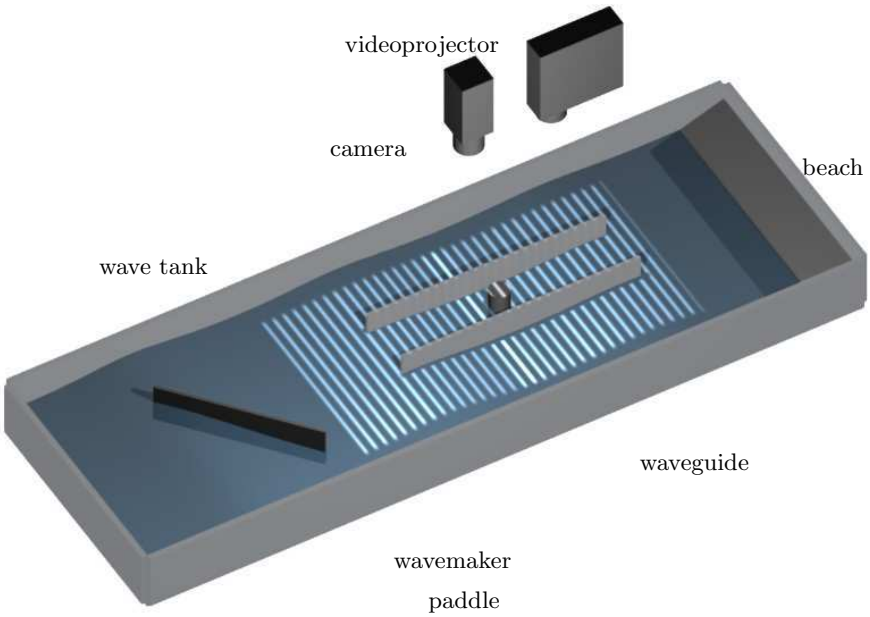


Figure 1: Scheme of the complete experimental setup, depicting both the wave tank and the optical measuring system. Inside the wave tank used for our experiments, the waveguide is placed with its walls parallel to those of the tank. The obstacle is placed symmetrically between the walls of the waveguide, equidistant from the waveguide's ends. The wavemaker is positioned near the waveguide, inclined with respect to its entrance in order to excite an asymmetric perturbation within it. At the other side of the wavetank, a sloped beach is used to avoid unwanted wave reflections. Our optical profilometric measuring system is placed over the channel, and is composed of a high-resolution videoprojector and a high-speed Phantom V9 camera. The videoprojector projects fringes onto the free surface (shown schematically in the figure) and the camera is used to capture images of the deformed fringes over the region of interest.

2. Experimental set-up

In this section we describe both the experimental set-up and protocol devised for the observation and measurement of the trapped modes' resonances.

Fig. 1 shows the whole system schematically. For the purpose of its description, the set-up can be divided into two main parts: the channel itself, in which the trapped modes excitation occurs and the measuring system.

2.1. *Channel*

The waveguide is formed by two vertical walls made of plexiglass, 60 cm long and 10 cm high, separated by a distance $2d = 10$ cm. A vertical circular cylinder of diameter $2a$ is positioned within the guide. Employing this setup, two configurations were explored. In the first configuration, the cylinder is placed symmetrically between the two walls and equidistant from the guide's ends (30 cm) (see Fig. 2(a)). The second configuration consists on the obstacle located at $3a$ from the entrance (Fig. 2(b)). For later reference, these two different obstacle configurations will be termed I and II, respectively.

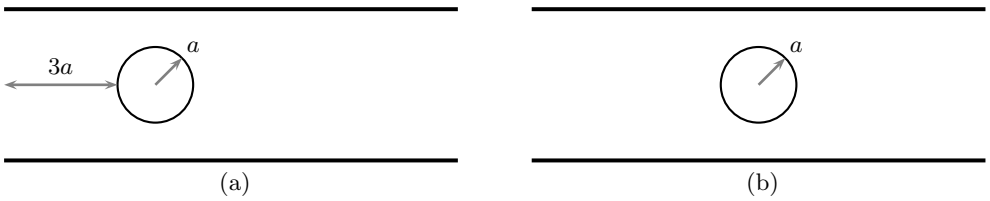


Figure 2: Two different obstacle arrangements employed in the present study, hereafter termed configuration I (a) and II (b).

For each one of these two configurations, obstacles of 12 different sizes ($2a$ = 20, 30, 40, 50, 60, 70, 75, 80, 85, 90, 95, 100 mm) were employed keeping the waveguide walls fixed at a distance of $2d = 100$ mm. In every case, the positioning of both the waveguide walls and the cylinder within them were assured to a precision of 0.1 mm. For each of these obstacles, a significative range of frequencies around the theoretical resonance was explored.

The whole waveguide–obstacle system is placed inside a larger water tank of dimensions $60 \times 180 \times 15$ cm^3. Water was employed as the working fluid, keeping a constant level of $H_0 = (5 \pm 0.05)$ cm throughout the experiments.

Special attention was taken in the design of the wavemaker mechanism so that it would provide a monochromatic sinusoidal mouvement of the paddle plate. To that end, we designed a bottom-hinged paddle-type wavemaker, with adjustable stroke amplitude and servo-controlled forcing frequency in the range of 1 to 5 Hz, adjustable in 0.02 Hz steps. The inner face of the paddle plate is put in contact with a thin circular disk placed above the water level with its axis perpendicular to the channel's bottom. In turn, the disk is attached excentrically to the axis of a rotating motor fixed to the wavemaker structure. Mechanical contact between the paddle and the disk is assured at all times by means of an auxiliary spring system. In this way, a constant-speed rotatory motion of the motor is transferred by the disk through the contact point to the paddle plate which describes a sinusoidal mouvement. Prior to this study, the monochromaticity of the wave paddle was checked measuring the spectrum of its oscillatory motion by laser triangulation. According to this study, the contribution to the first harmonics is less than -2 dB and that of the the third, less than -4 dB, which renders it an efficient monochromatic wave paddle for the purposes of this study.

The key factor for achieving the excitation of trapped modes is to send a small antisymmetric perturbation inside the guide. As theoretically predicted trapped modes are known to be antisymmetric with respect to the waveguide longitudinal centerplane, therefor to be able to excite such trapped modes inside the waveguide, one must be capable of forcing a perturbation with antisymmetric components at the entrance. From an experimental standpoint, two practical limitations are naturally imposed to the amplitude of the antisymmetric perturbation at the entrance of the waveguide. The first constraint is imposed by the presence of dissipation, which demands the perturbation to be large enough at the entrance so the amplification around the obstacle could be detected by our mesuring technique. However, it should also remain small so that the effect of nonlinearities does not become significant. These two constraints led us to a configuration in which the wavemaker is placed at an angle of around 40◦ with respect to the waveguide centreline, so that both antisymmetric as well as symmetric components are transmitted down the guide. It should be noticed, however, that these two components travel differently inside the waveguide. The symmetric part of the perturbation behaves as a propagating wave for any incident frequency, as both ends of the waveguide are open.

In contrast, any antisymmetric component with frequencies below the cut-off $kd < \pi/2$, enters the guide as an evanescent wave.

At the other end of the water tank, 60 cm away from the waveguide's exit, an inclined beach is disposed in order to mitigate unwanted wave reflections. This wave-absorbing beach is made of a styrofoam-covered rectangular plastic plate and is placed forming an angle of approximately 20° with the tank's bottom. In spite of its simplicity, preliminary tests showed that the reflected-to-incident wave amplitude ratio was slightly less than 5 %, which renders it a highly efficient absorber for the purposes of this study.

2.2. *Optical measuring system*

A complete characterization of the water-wave trapped mode resonances requires their observation and localization in frequency space, as well as a detailed study of their global spatial structure and time evolution. In order to pursue such an experimental description, the measuring technique should meet several requirements. The first requirement is that of being non-intrusive, so as not to introduce external perturbations to the system under study. To account for the spatial structure of the surface trapped modes the technique should be global, *i.e.* able to measure the free surface deformation over an extended area of the surface. In addition, a high spatial resolution within this interrogation area is demanded so that the smallest significant features of the flow are correctly detected. In our case, this amounts to wavelengths of the order of the capillary length. An additional condition arises from the consideration of the measurement range. In general, resonant states are characterised by amplitudes which considerably exceed those associated with far-off-resonance states (in the particular case of this study, as much as 30 times). Therefore, measuring the free surface deformation amplitude consistently as it approaches the resonant state requires a high vertical resolution throughout a large vertical measurement range. The last major requirement on the measuring technique focuses on its temporal resolution. Indeed, short observation times are imperative to accurately follow the dynamics of (local) perturbations in their propagation and spread along the surface. Therefore, the propagation velocity of surface waves emerges naturally as a limitating factor which, together with the spatial resolution, sets a threshold for the observation time.

These requirements have led us to the development of an optical profilometric technique that allows for high-resolution 3D whole-field reconstruction of time-dependent free-surface deformation fields. Our technique is based on a particular fringe projection profilometry method known as Fourier tranform profilometry (herein termed FTP), originally due to Takeda *et al.* (1982); Takeda & Mutoh (1983), successfully applied in the past for the topography of solid surfaces in a variety of fields such as mechanical engineering, machine vision, industry monitoring and quality assessment, etc. The adaptation and enhancement of this particular technique for the measurement of free-surface deformations were described in by Cobelli *et al.* (2009) and Maurel *et al.* (2009), where its applicability to a variety of fluid dynamics' scenari was demonstrated.

The operating principle of the FTP method is the following. A fringe pattern of controlled characteristics is projected onto the free surface and its image is registered by a camera. The deformed fringe pattern due to the surface deformations is later compared to the undeformed (reference) one, leading to a phase map. A phase-to-height relation involving the optical system parameters can be derived based on the laws of geometrical optics, from which the local free-surface height can be reconstructed.

The optical measuring system devised for high-resolution surface deformation mapping is also schematically shown in Fig. 1. In our experiments, water was employed as

the working liquid. In order to be able to project images onto the water surface its light diffusivity is enhanced by the addition of a white (titanium dioxide-based) liquid dye. Any potential variation in the surface tension is not expected to affect our results signifficatively as our experimental parameters place us in the gravity surface waves regime.

A computer-controlled digital videoprojector with a resolution of $1,920\times1,280$ px^2 and 12-bit-depth is employed for the projection of fringe patterns. This allows us to project sinusoidal fringe patterns of controlled wavelength, more adapted to Fourier analysis than the square profile (Ronchi-type) gratings commonly used. This results in an overall quality gain in both the frequency space filtering process inherent to the technique and in the phase recovering. Another advantage of this videoprojector system is the possibility to laterally shift the image with respect to its optical axis, approaching it towards the camera's field of view without introducing optical aberrations that would deform the fringes. Once the projector–free-surface working distance L is set, the size of the projection window can be adjusted to fit either a small or a relatively large area over the liquid surface. In this experimental study, we employed a projection distance $L = 100.7$ cm and a projection window covering (but not limited to) the entire free-surface (including the obstacle) within the waveguide, of size 10×40 cm^2.

The fringe patterns projected onto the liquid's free surface were recorded by a Phantom V9 monochrome high-speed camera, with a resolution of $1,632 \times 1,200$ px^2 and a color depth of 10 bits.

The relative positioning of the videoprojector and the camera is as follows. Their optical axis are perpendicular to the channel's bottom, parallel to one another, and separated by a distance $D = 35$ cm. The entrance pupils of both instruments lie on a plane parallel to that of the unperturbed surface, a distance L over it.

Data acquired by the camera were later recorded as uncompressed raw tagged image file format (TIFF) to avoid any artifact from the camera's firmware preprocessing algorithm, such as those associated to quantization, compression, color depth reduction, etc.

The whole fringe projection and image capturing system is held over the channel supported by a structure that allows for precise alignment and relative positioning of the optical devices.

This technique has a theoretical resolution in the measured surface elevation given by geometrical optics which is limited by the size of the projected pixel. In the present experiments, this latter corresponds to 0.23 mm. The attained resolution is exemplified on Fig. 3 where a comparison with a measurement by laser profilometry (5 μm precision) has been performed at a particular point in the surface. In this figure, $|h^{\mathrm{FTP}} - h^{\mathrm{laser}}| \leq$ 0.2 mm, in agreement with the estimated resolution. This validates our measurements and fixes the resolution.

2.3. *Data acquisition and treatment*

For any given values of a/d and driving frequency f, the camera sampling frequency f_S was set at $f_S = 100f$, leading to 100 frames per period. Two periods of oscillation were registered in each case. For every image in a time series, a free-surface height is obtained by means of the inversion algorithm used in FTP.

2.3.1. *Decomposition in harmonics of the driving frequency*

The global nature of our measuring technique allows us to decompose the time evolution of the free-surface deformation (herein, FSD) $h_T(x, y, t)$ in terms of the harmonics of the driving angular frequency $\omega = 2\pi f$. The latter can be represented as a complex

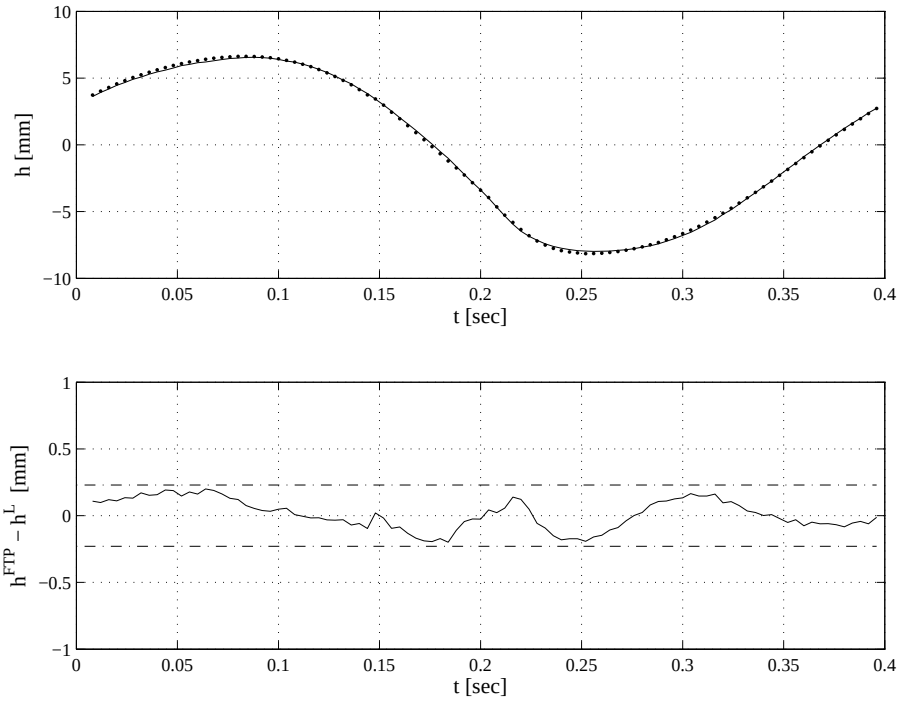


Figure 3: Comparison between two measurements made at the same point with an standard laser profilometer (plain line) and FTP at the same point (dashed line).

Fourier series expansion in the following form

$$h_T(x,y,t) = \sum_{n=-\infty}^{+\infty} h_n(x,y)\, \mathrm{e}^{in\omega t}, \tag{2.1}$$

where we have introduced the complex-valued amplitude $h_n(x,y)$ associated with the n-th harmonic. These complex amplitudes h_n are obtained from the measured fields that are, of course, real ($h_{-n} = h_n^*$, where asterisk denotes complex conjugate). To do that we derive, at each measurement point (x,y), the coefficients of the real Fourier expansion in time (100 times per period, which allows an accurate integration).

Such a decomposition scheme in terms of harmonics of the driving frequency presents many advantages for the analysis of the dynamics of the free surface deformation. On the one hand, separation of the linear part of the free surface deformation from the non-linear contributions (with frequencies corresponding to $0, 2\omega, 3\omega$, etc.). is straightforward, which enables a comparison between the two. Furthermore, when complemented by the global nature of our measuring technique this comparison serves to evaluate the relative importance of the non-linear components *locally* within the guide. In the case of this experimental study, this separation is particularly suitable as it allows us to compare our results with the predictions from the available *linear* theories (see Section 4).

2.3.2. *Decomposition in symmetric and antisymmetric parts*

Finally, we define two fields, one symmetric and another antisymmetric about the waveguide's centerline by means of the usual definitions,

$$H_n^s(x,y) = \frac{1}{2}\left[H_n(x,y) + H_n(x,-y)\right] \tag{2.2}$$

$$H_n^a(x,y) = \frac{1}{2}\left[H_n(x,y) - H_n(x,-y)\right] \tag{2.3}$$

for the symmetric and antisymmetric parts, respectively.

3. Resulting patterns

In this Section we expose the results obtained following the previously described decomposition from the instantaneous total fields to the harmonics and finally to the symmetric and antisymmetric fields. This latter antisymmetric field corresponds to the trapped mode that is the main subject of the present study.

3.1. *Instantaneous free surface deformation field*

Fig. 4 shows a sequence of instantaneous free-surface deformation fields for $a/d = 0.5$ and $f = 2.5$ Hz, close to the experimentally determined resonant frequency (see also Movie 1)†. In practice, this sequence consists on 100 frames registered at an acquisition rate of 250 Hz. Here, only one over ten fields is shown. For the present figures, the configuration II was chosen because the cylinder being closer to the entrance makes the amplitudes larger, rendering the phenomenon more evident.

† The associated video will be available for download at the Journal's site after publication of the manuscript.

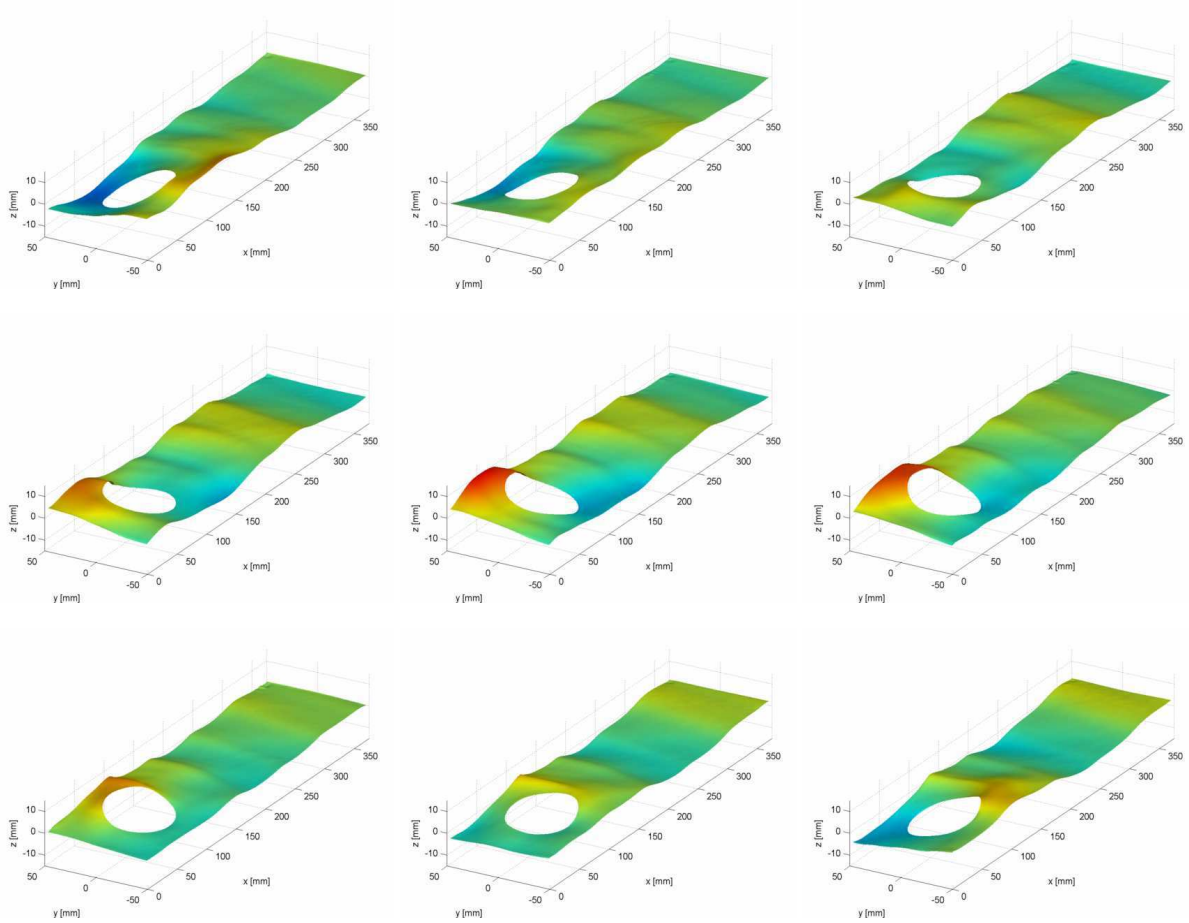
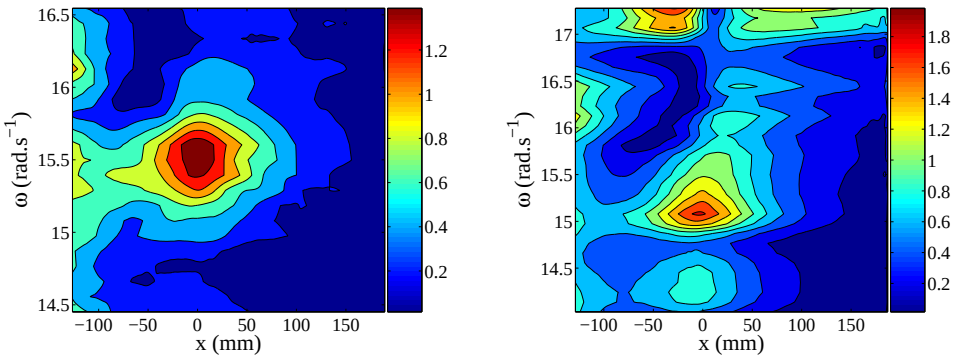


Figure 4: Experimental measurements of the instantaneous total free-surface deformation fields. The figure shows a time-sequence of the evolution of the free surface deformation fields for a particular case of the aspect ratio explored, namely $a/d = 0.5$. The wave's incident frequency corresponds to $f = 2.5$ Hz. Frames are separated by $\Delta t = 0.04$ s.



(a) $a/d = 0.5$ (b) $a/d = 0.85$

Figure 5: Experimental evidence of the trapped mode resonance: $1/2 \cdot [h_T(x, y, t) - h_T(x, -y, t)]$ for some fixed (y, t) is displayed in color scale as a function of x and ω. (a) For $a/d = 0.5$, one resonance is visible near the cylinder, (b) for $a/d = 0.85$ in addition to the first resonance a second maximum near the cut-off frequency can be seen. The cylinder lays at $x = 0$ mm (configuration I). The scale of the color bar is in mm.

In these figures, local height is linearly color-coded between red and blue, the former corresponding to elevations and the latter to depressions (with respect to the free-surface at rest). With this convention, green is associated with undeformed regions. For the sake of comparison, the same color scale was maintained throughout the sequence.

These snapshots illustrate the dynamics of the free-surface in the presence of a trapped mode. The region near the obstacle is characterised by an asymmetric oscillation at the driving frequency, with amplitudes that largely exceed that at the waveguide's entrance. In this region the local surface curvature is rather large, as evidenced by the presence of steep slopes in the vicinity of the obstacle.

In contrast, the region far past the cylinder shows only the propagation of a plane, slightly attenuated wave. Furthermore, the amplitude of this wave is of the same order as that of the incident wavefront. Perhaps the most striking feature observed in this region is the recovery of symmetry.

These observations effectively suggest the existence of an antisymmetric deformation localised in the vicinity of the obstacle, decaying rapidly with distance. However, and due to our particular choice of the experimental setup, the theoretically predicted pure antisymmetric nature of the trapped mode is still concealed by the plane wave propagating down the waveguide and by the presence of non-linearities (if any).

From these acquisitions a direct but qualitative evidence of the trapped mode resonance can be exhibited. The symmetry of the geometry decouples the fields into two families, even and odd with respect to y. Figure 5 shows the odd family: $1/2 \cdot [h_T(x, y, t) - h_T(x, -y, t)]$ as a function of x and the driving pulsation ω at some fixed (y, t). One or two spots with maximum amplitudes are visible in the vicinity of the cylinder at some particular frequencies, indicative of the presence of resonances.

3.2. *Pattern of the harmonics*

A time decomposition in harmonics of the driving frequency is calculated from 100 instantaneous FSD fields within one period. The first three Fourier modes obtained with this decomposition ($a/d = 0.5$, at the resonance frequency $f_r = 2.47$ Hz) are shown in Fig. 6 and Fig. 7 for type-I and II configurations, respectively.

For both types of configurations (Figs. 6-7), the linear mode $h_1(x, y, t)$ is depicted in

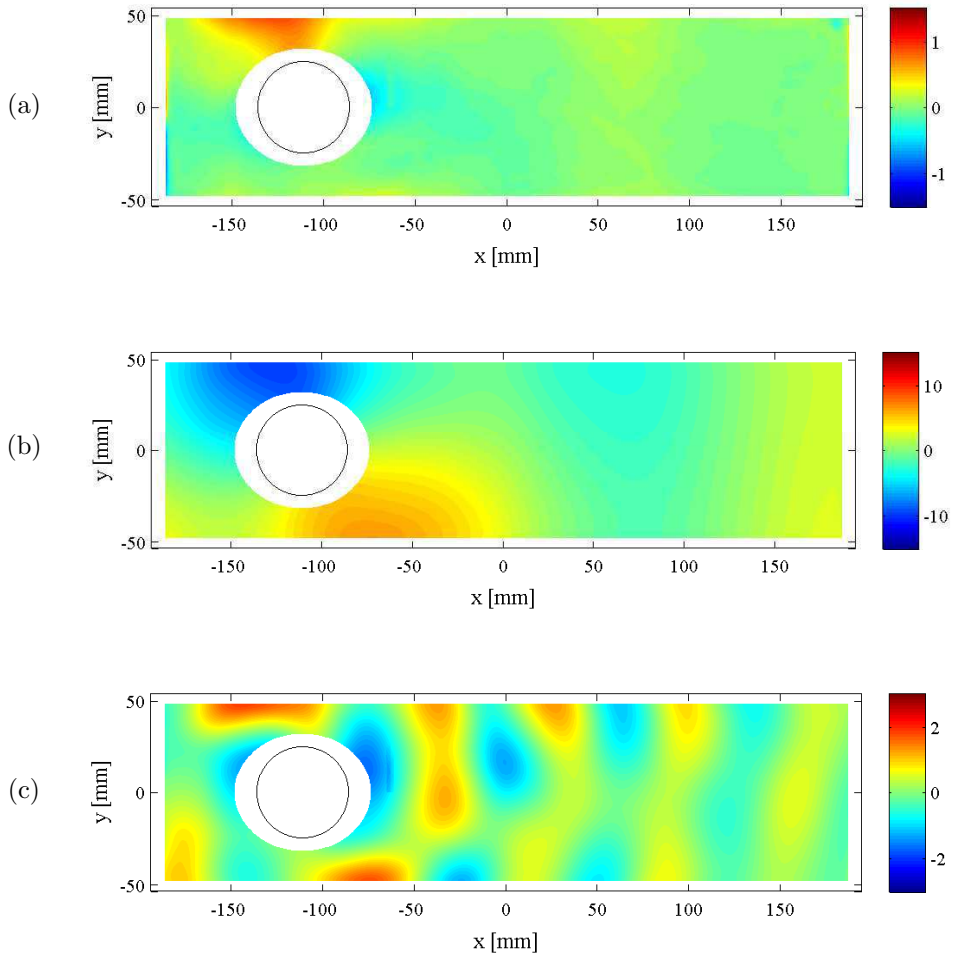


Figure 6: Experimentally measured free-surface deformation fields decomposed in harmonics of the driving frequency: Type I configuration for $a/d = 0.5$. (a) Zeroth order contribution $h_0(x, y)$, (b) linear contribution $h_1(x, y, t)$ and (c) first harmonic component $h_2(x, y, t)$ corresponding to a pulsating frequency of $2\,\omega$. The position of the obstacle within the waveguide is indicated by the black circle. The scale of the colorbar is in mm.

panel (b). The contribution of the antisymmetric trapped mode clearly appears when the cylinder is near the entrance, overcoming the contribution of the symmetric mode at this frequency. To the opposite, when the cylinder is farer in the waveguide, the field displays mainly the propagative plane symmetric mode. This is because the antisymmetric mode (evanescent) has lost in amplitude when it is trapped in the vicinity of the cylinder.

The panels (a) and (c) show the first two non linear fields $h_0(x, y, t)$ and $h_2(x, y, t)$ at $\omega \pm \omega$. The zeroth order contribution, $h_0(x, y)$ shown in Fig. 6(a) corresponds to the local steady deformation of the free surface,representing a distortion to the base flow.

The field $h_2(x, y, t)$ corresponds to oscillations of twice the pulsation frequency. In both cases, the proximity of the cylinder to the entrance clearly amplifies the non linearities. The symmetric field is not significantly different in the two configurations while the

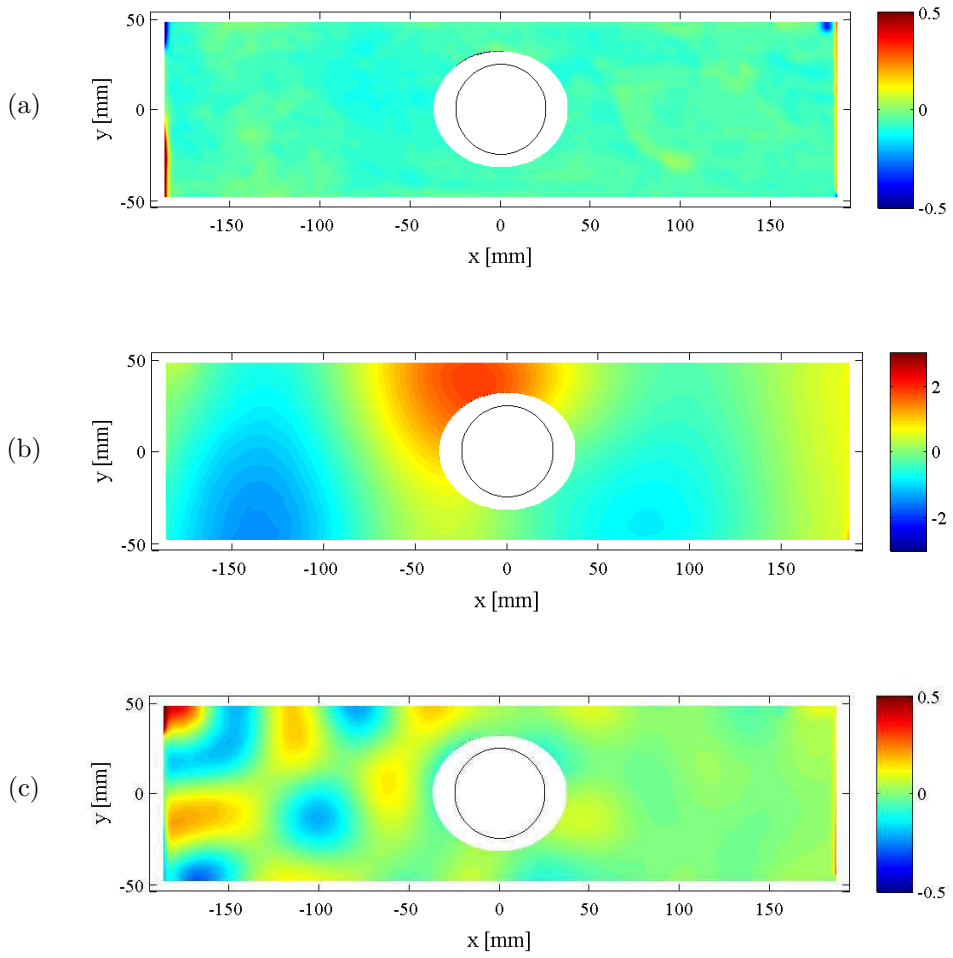


Figure 7: Experimentally measured free-surface deformation fields decomposed in harmonics of the driving frequency: Type II configuration for $a/d = 0.5$. (a) Zeroth order contribution $h_0(x, y)$, (b) linear contribution $h_1(x, y, t)$ and (c) first harmonic component $h_2(x, y, t)$ corresponding to a pulsating frequency of $2\,\omega$. The position of the obstacle within the waveguide is indicated by the black circle. The scale of the colorbar is in mm.

antisymmetric fields differ in both configuration by a factor close to 10. This is evidenced in the Fig. 8. This suggests that the nonlinearities are due mainly to the antisymmetric contribution. Incidentally, symmetric patterns are used to obtain a direct measurement of the incident wavelength k (see Section 4.1).

3.3. *Trapped mode pattern*

Figs. 8(b) and 9(b) show the spatial pattern of a trapped mode for the case $a/d = 0.5$, in type I and II geometrical configurations, respectively. In the following, we focus on the configuration I. This is done in order to be placed in the linear regime, avoiding the possible influence of nonlinearities on the linear contribution.

The same decomposition for the cases $a/d = 0.4, 0.8$ and 0.95 is shown in Figs. 10-11. These figures exemplify the two trapped modes isolated in the antisymmetric part of the

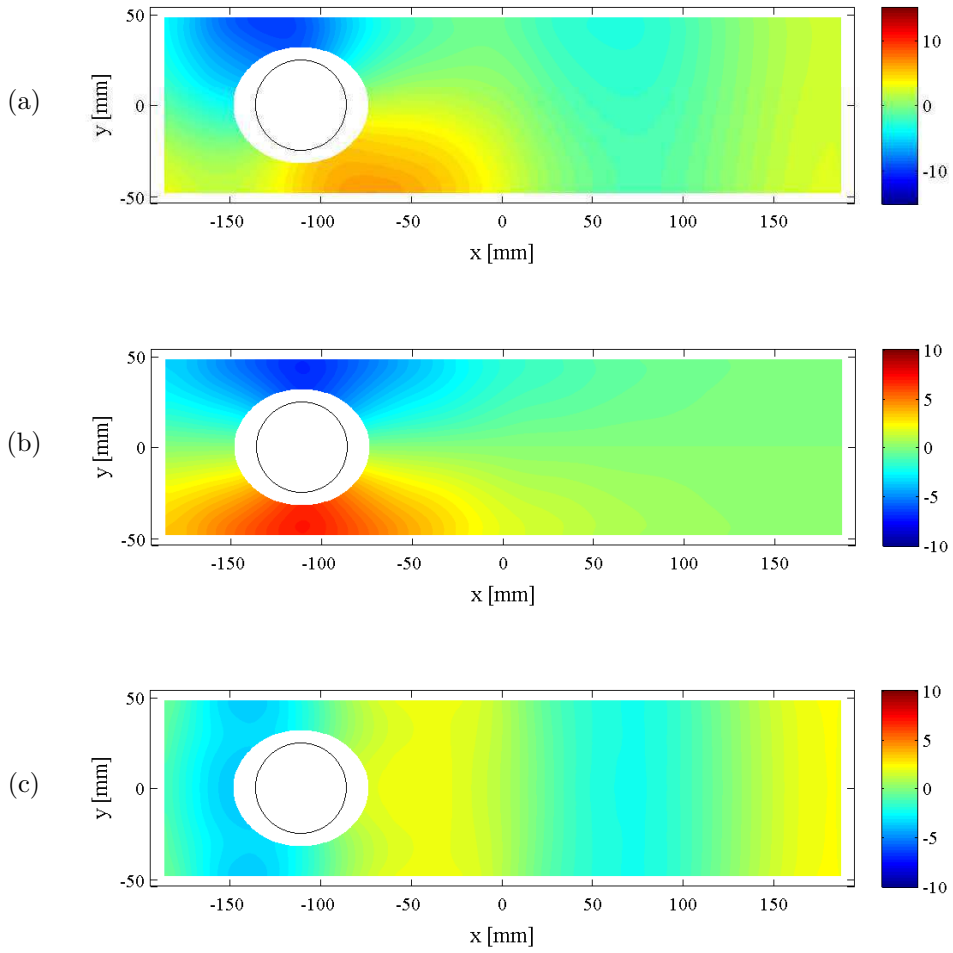


Figure 8: Linear part of the experimentally measured free-surface deformation: Type I configuration for $a/d = 0.5$. Panel (a) shows the linear deformation field $H_1(x, y)$ (same as in). Panels (b) and (c) presents the symmetric and antisymmetric parts of the linear mode $H_1(x, y)$, respectively. The position of the obstacle within the waveguide is indicated by the black circle. The scale of the colorbar is in mm.

field. They are well localized in the neighbourhood of the cylinder and are either symmetric with respect to the Oy axis, as predicted by Callan *et al.* (1991), or antisymmetric with respect to the Oy axis, as predicted in Evans & Porter (1999). This latter trapped mode is expected to exist for $a/d \gtrsim 0.81$, a fact that is experimentally confirmed in this study.

In the forthcoming section (see Section 4.2) the comparison between the spatial structure of the experimentally determined $h_1^a(x, y, t)$ and the theoretical predictions will be shown.

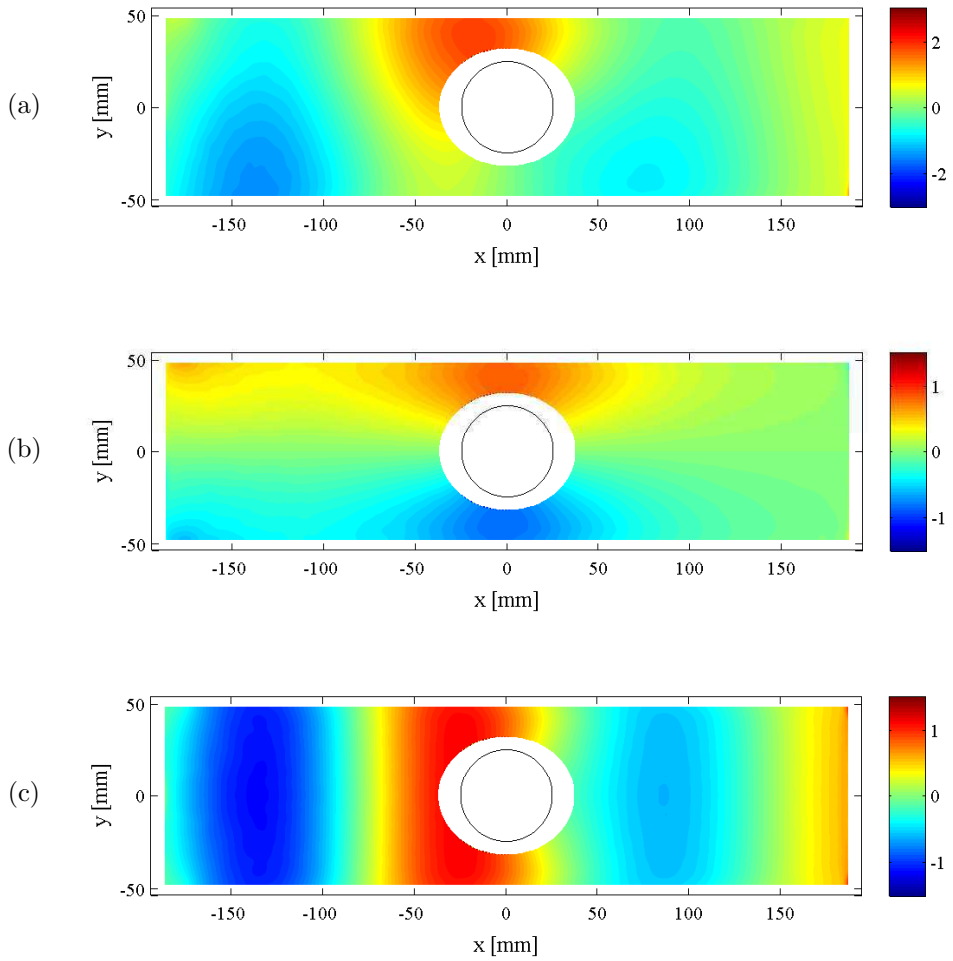


Figure 9: Linear part of the experimentally measured free-surface deformation: Type II configuration for $a/d = 0.5$. Panel (a) shows the linear deformation field $H_1(x, y)$ (same as in). Panels (b) and (c) presents the symmetric and antisymmetric parts of the linear mode $H_1(x, y)$, respectively. The position of the obstacle within the waveguide is indicated by the black circle. The scale of the colorbar is in mm.

4. Analysis of the experimental results and comparison with the linear theory

In this section, we will only keep the linear contribution to the free-surface deformation, discarding higher-order harmonics. The purpose of this data filtering is two-folded. On one hand, it serves to simplify both the analysis of data and the interpretation of results. On the other, it allows us to compare our experimental results with the available theoretical predictions arising from linear theories. Moreover, in light of the experimental evidence on the preponderance of the linear contribution, which represents 80 % of the total free-surface deformation, a description of the trapped mode resonance phenomena in terms of a linear theory is indeed justified.

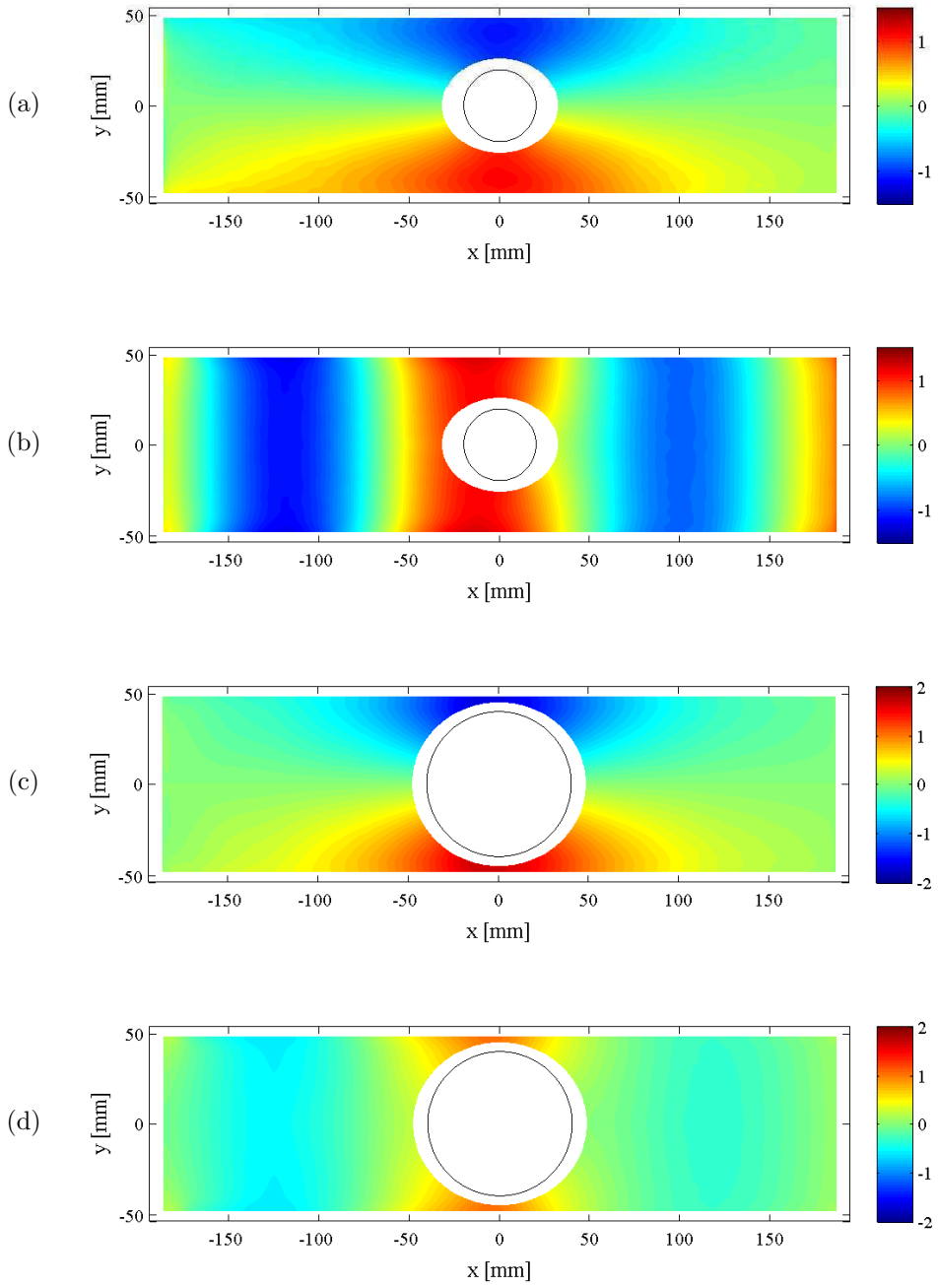


Figure 10: Experimental patterns of the trapped modes and their associated symmetric parts. Panels (a-b): Symmetric and antisymmetric fields of $h_1(x, y, t)$ for $a/d = 0.4$ and $kd = 1.46$, ($f = 2.50$ Hz). Panels (c-d): Same representation for $a/d = 0.80$ and $kd = 1.33$ ($f = 2.40$ Hz). The position of the obstacle is indicated by the black circle. The scale of the colorbar is in mm.

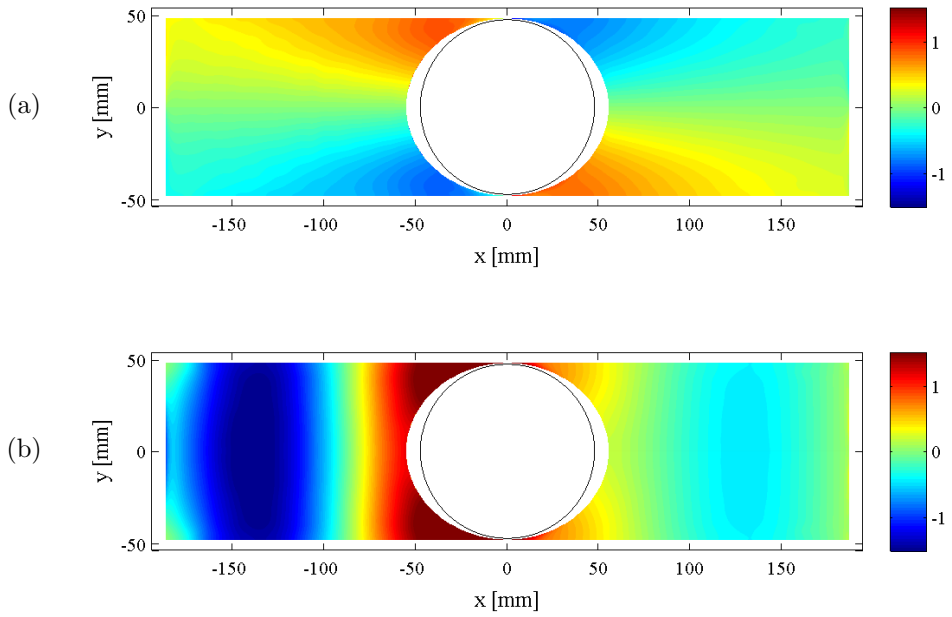


Figure 11: Experimental patterns of a second kind of trapped modes and their associated symmetric part. Panels (a-b): symmetric and antisymmetric fields of $h_1(x, y, t)$ for $a/d = 0.95$ and $kd = 1.51$ ($f = 2.62$ Hz). The position of the obstacle is indicated by the black circle. The scale of the colorbar is in mm.

4.1. *Dispersion relation*

From the symmetric part of the field at the driving frequency (as shown in panels (b) and (d) of Fig. 10 and in panel (b) of Fig. 11), we get a direct measurement of the wavenumber k. Although there is only few wavelengths in the waveguide, a reasonable estimate is possible by determining the periodicity of the quantity $h_1^s \times h_1^{s*}$ ($.^*$ denotes the complex conjugate). Indeed, h_1^s is the sum of an incident wave e^{ikx} and of a reflected wave e^{-ikx} (reflection at the end of the waveguide). Thus, the quantity $h_1^s \times h_1^{s*} \propto a + b\cos 2kx$ can be fitted. Fig. 12 shows the result for all values of the a/d ratio considered in this study. The resulting values agree with the theoretical prediction given by

$$\omega^2 = gk \tanh kh_0, \tag{4.1}$$

where $g = 9.81$ m.s^{-2} is the gravitational acceleration.

We expect the symmetric propagating mode to experience an attenuation, that is the wavenumber is

$$K = k + i\epsilon(k), \tag{4.2}$$

with k real and $\epsilon(k)$ being the attenuation due to dissipative mechanisms. Because of the smallness of this attenuation, we have not been able to obtain it from a direct measurement. In contrast, such a determination was made roughly indirectly (see Section 4.3.2).

4.2. *Analysis of the spatial structure of the trapped mode*

In this section, the detailed spatial structure of the measured surface-wave trapped mode is compared to the theoretical predictions based on multipole expansions (Linton & McIver

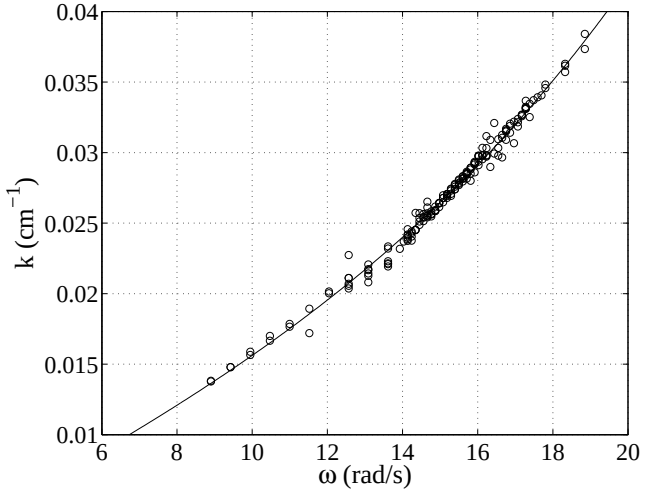


Figure 12: Dispersion relation. The point cloud gathers all experimental data points obtained throughou the experiences. The theoretical dispersion relation given by eq. 4.1, represented by the continuous line, is shown for comparison purposes.

2001). In this approach, the free surface deformation is represented by a sum of singularities placed within any structures that are present. These singularities, called multipoles, are constructed in such a way as to satisfy the field equation, the free-surface and bed boundary conditions, and a radiation condition. A linear combination of these multipoles is then considered and made to satisfy the appropriate body boundary condition. This leads to an infinite system of linear algebraic equations for the unknown coefficients of the multipole expansion which can be solved numerically by truncation. In addition, many theoretical studies have shown (Callan *et al.* 1991) that the systems of equations that result from using a multipole method possess good convergence characteristics and only a few equations are needed in order to obtain an accurate numerical approximation.

For the case of a surface-piercing vertical circular cylinder placed symmetrically between the walls of an infinite waveguide, Callan *et al.* (1991) have shown that the trapped mode solution can be written as

$$h(r,\theta) = \sum_{n=0}^{\infty} a_n \left[k\, Y'_{2n+1}(ka)\right]^{-1} \psi_{2n+1}(r,\theta), \tag{4.3}$$

where $\psi_{2n+1}(r,\theta)$ are a suitable set of multipoles defined by

$$\psi_{2n+1}(r,\theta) = Y_{2n+1}(r,\theta)(kr)\sin(2n+1)\,\theta + \sum_{m=0}^{\infty} A_{mn} J_{2n+1}(kr)\sin(2m+1)\,\theta, \tag{4.4}$$

and a_n are the expansion coefficients to be determined. In these expressions, the pair (r,θ) denotes standard polar coordinates; $J_\nu(\cdot)$ and $Y_\nu(\cdot)$ represent the Bessel functions of the first and second kind, respectively, and the dash refers to the derivative with

respect to the argument. In addition, A_{mn} is given by

$$A_{mn} = -\frac{4}{\pi}(-1)^{m+n}\int_0^\infty \frac{\mathrm{e}^{-\gamma d}\sinh(2n+1)\,v\sinh(2m+1)\,v}{\cosh(\gamma d)}\,dv - \frac{4}{\pi}\int_0^\pi \tan(\beta d)\cos(2n+1)\,u\cos(2m+1)\,u\,du, \quad (4.5)$$

where the auxiliary functions

$$\beta = k\sinh v, \quad (4.6)$$

$$\gamma = k\cos u, \quad (4.7)$$

have been defined to simplify the notation.

Application of the cylinder boundary condition leads to a homogeneous infinite Fredholm system of equations of the second kind for the coefficients a_n in the form

$$a_m + \sum_{n=0}^{\infty} B_{mn}\,a_n = 0, \qquad (m = 0, 1, 2, \ldots), \quad (4.8)$$

where

$$B_{mn} = A_{mn}\,\frac{J'_{2m+1}(ka)}{Y'_{2n+1}(ka)}. \quad (4.9)$$

This system has a non-trivial solution (trapped mode) if and only if its infinite determinant

$$\Delta_\infty \equiv \det\,(\delta_{mn} + B_{mn}(ka, kd)) \quad (4.10)$$

vanishes for some ka, kd, with $0 < ka < kd < \pi/2$. It has been shown (see Callan *et al.* 1991, Appendix B and subsequent discussion) that the determinant Δ_N associated to the truncated system at order N converges uniformly to the determinant of the infinite system Δ_∞ as N tends to infinity, so that trapped modes can be obtained numerically by solving the truncated system up to order N. However, it was found numerically (Callan *et al.* 1991) that the value of N required to obtain a given accuracy was strongly dependent on the value of the ratio a/d.

The numerical calculation scheme is as follows. For a given a/d ratio, we consider the associated truncated homogeneous system of equations of order N (composed of $N+1$ multipoles), *i.e.*,

$$a_m + \sum_{n=0}^{N} B_{mn}(ka, kd)\,a_n = 0, \qquad (m = 0, 1, 2, \ldots, N). \quad (4.11)$$

The zero of its determinant, corresponding to the theoretical trapped mode wavenumber k_{th}, is found numerically using a standard library routine. For this particular wavenumber, the expansion coefficients a_n are therefore determined by solving the truncated system up to order N. Now $N+1$ multipoles are considered, and this scheme is repeated iteratively until a convergence criteria is achieved for the determination of both the trapped mode frequency k_{th} and the expansion coefficients a_n. The integrals involved in the calculation of A_{mn} (given by eq. (4.5)) are evaluated numerically using a local adaptive integration strategy. Potential contours and streamlines are also determined numerically from these results.

A comparison between our experimental measurements and the theoretical predictions of linear theory for three different obstacle sizes is shown in Fig. 13. The top panel corresponds to $a/d = 0.2$, $kd = 1.55$. The theoretical contours depicted in this panel were

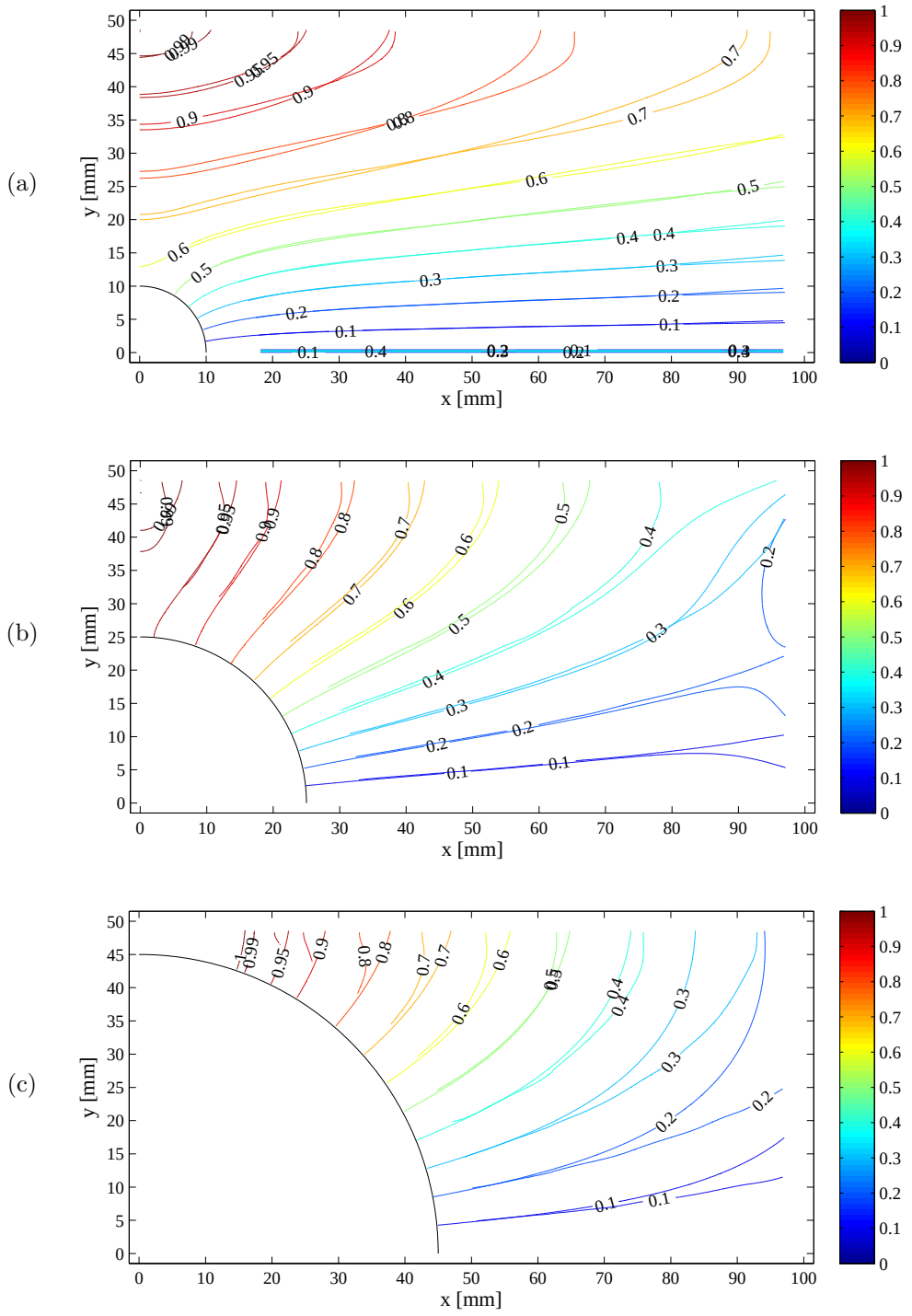


Figure 13: Experimentally measured trapped modes' spatial structure as compared to the theoretical predictions from linear theory. Experimental measurements (continuous lines) and theoretical predictions (dashed lines) for three a/d ratios at their respective resonance frequency. Top: $a/d = 0.2$, $kd = 1.55$, center: $a/d = 0.5$, $kd = 1.39$, and bottom: $a/d = 0.9$, $kd = 1.33$. Theoretical and experimental cases are normalized in this case to facilitate the comparison.

built using only 2 multipoles, which assures an error less than 5%. Shows a remarkable agreement between theory and experiment.

The same comparison is presented in panel (b) for an intermediate case, namely $a/d = 0.5$, $kd = 1.39$. The theoretical contours to which our experimental data are compared were built using a multipole expansion composed of $N = 6$ multipoles. The agreement between theory and experimental data is very good in the region near the obstacle, and slightly differs far from it. Another source of difference between the two can be found at the walls, as the theoretical model does not take into account the presence of the meniscus that is evidenced in the experimental case.

Finally, panel (c) shows a third case corresponding to $a/d = 0.9$, $kd = 1.33$. Theoretical contours used for comparison in this case correspond to an expansion built using $N = 9$ multipoles. Even though the overall agreement is good, our results shows that, for the largest aspect ratios considered, the multipole expansion method does not reproduce well the trapped mode's structure. This is presumably due to the fact that, in those cases, other factors not considered in the theory (such as surface tension) play a non-negligible role in determining the spatial shape of the trapped mode.

4.3. *Resonance curves*

4.3.1. *Analysis of the far field: the scattering problem*

The process of excitation of the trapped mode can be analysed as follows. Initially, an antisymmetric wave of amplitude A is sent into the guide. As the associated wavenumber $i\alpha$ is below the threshold for propagation ($\alpha d < \pi/2$), the antisymmetric wave enters the guide as an evanescent wave, its amplitude decaying exponentially with distance from the waveguide's entrance. However, the presence of an obstacle (placed at a finite distance within the guide) introduces a change in the geometry, drastically affecting the propagation conditions in its vicinity. In that region, even though its amplitude is weak, the incident antisymmetric wave interacts with the obstacle.

This interaction gives rise to a reflection and a transmission of the incident evanescent wave from the obstacle. At the waveguide's exit there is also a reflection due to the unmatched impedance. The long distance between the obstacle and the exit makes this latter reflection negligible.

Because of the Neumann boundary condition on the waveguide's walls, the antisymmetric field can be decomposed onto an infinity of transverse modes of the form $\sin(2n+1)\pi y/2d$. Each one of these transverse modes is associated with an eigenvalue α_n. Again, as we are working below the cut-off frequency, all α_n are real or, in other words, all these modes are evanescent. Among these, the less evanescent mode corresponds to $n = 0$.

To go further in our analysis, it is of interest to consider the field $H_1^a(x, y, t)$ as in a one-dimensional problem by projecting the 2D field onto this dominant first transverse mode. Assuming

$$H_1^a(x, y, t) \sim h(x, t) \sin \frac{\pi y}{2d}, \tag{4.12}$$

the one-dimensional field $h(x, t)$ is

$$h(x, t) = \frac{1}{d} \int_{-d}^{d} H_1^a(x, y, t) \, \sin \frac{\pi y}{2d} \, dy. \tag{4.13}$$

Of course, this assumption is expected to hold only in the far field of the obstacle (see Fig. 14). In the near field region, the higher transverse modes are expected to contribute to the 2D solution. The typical behaviour of $h(x, t)$ is illustrated on Fig. 14. For the sake

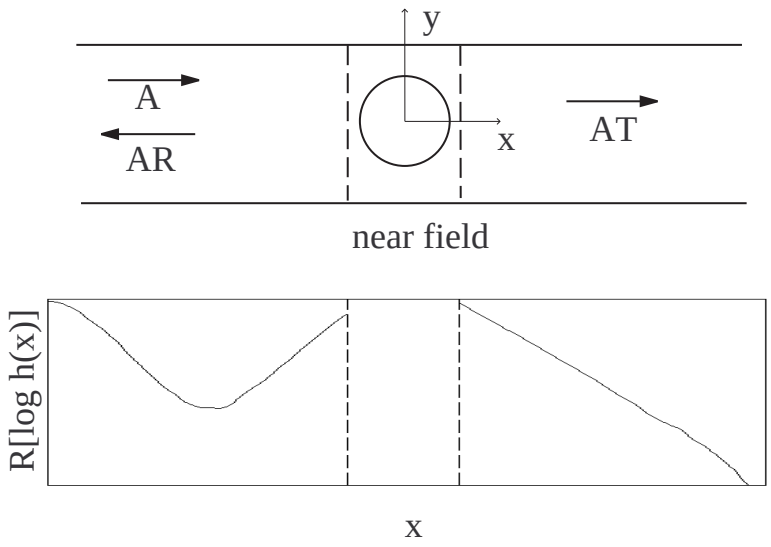


Figure 14: Top: The problem reduces to a 1D problem along the x-axis, by projecting the antisymmetric field onto the first transverse mode in $\sin \pi y/2d$ outside the near field region. Bottom: Typical variation of $h(x)$ along the x-axis: real part of $\log[h(x)]$ as a function of x (a.u.) (the curve has been obtained for $a/d = 0.4$, $kd = 1.47$).

of simplicity, the far field can be decomposed into two regions. The first one shows, as expected, the incident evanescent mode whose amplitude decays as it enters the guide as well as its reflection due to the presence of the obstacle. On the other side, only a transmitted mode is found, which decays rapidly away from the obstacle. It is worth noting that in this case no reflection is observed from the waveguide's exit, which confirms our working hypothesis.

4.3.2. *Shape of the resonance curves*

In the following, we denote by (R, T) the reflection and transmission coefficients of the obstacle, respectively. These magnitudes are of interest as they completely characterize the obstacle as an scatterer, independently of the incident amplitudes which may, experimentally, vary with frequency. Finally, to simplify the notation, the time dependence of $h(x, t)$ in $\cos(\omega t + \varphi)$ is omitted, leading to a one-dimensional profile $h(x)$:

$$h(x < -\delta) = A\, e^{-\alpha x} + AR\, e^{\alpha x}, \tag{4.14}$$

$$h(x > +\delta) = AT\, e^{-\alpha x}, \tag{4.15}$$

with A the amplitude of the incident wave, α stands for α_1. Experimentally, the profile $h(x)$ have to be fitted in both regions I and II to get α and (R, T). Two different strategies are used in each region. In practice, we begin by adjusting the second region. Here, $h(x)$ is simply fitted by an exponential decay from which AT and α are calculated.

For region I, owing to the previous determination of α, only two parameters A and $\mathcal{R}$

are to be fitted. This process can be simplified employing the two combinations given by

$$2A = \left(h(x) - \frac{h'(x)}{\alpha} \right) \mathrm{e}^{\alpha x}, \tag{4.16}$$

$$2AR = \left(h(x) + \frac{h'(x)}{\alpha} \right) \mathrm{e}^{-\alpha x}. \tag{4.17}$$

Gathering the results from both zones, the parameters R, T and α are obtained for any value of ω, the driving pulsation.

The uncertainty in the determination of the reflection–transmission pair (R, T) in these cases becomes significant, attaining values up to 30%, when the size of the intervals varies because of the low signal-to-noise-ratio.

For a given obstacle of diameter $2a$, a large range of driving frequencies was explored. In every case, the reflection and transmission coefficients, as well as α, are fitted as described below. These results led to the construction of the associated resonance curves.

Resonance curves obtained for several aspect ratios a/d considered in this study are shown in Fig. 15(a)-(h). Each panel shows the absolute values of the reflection (plain circles) and transmission (open circles) coefficients as a function of the non-dimensional parameter kd. As can be seen, there's a resonance visible in every curve (two resonances for $a/d = 0.85, 0.90, 0.95$). Nevertheless, the error on these coefficients becomes dramatically important with distance from the resonance. This is because the amplitudes far from resonance are very weak, near the threshold for resolution of the measuring method (about 0.1 mm). This is indeed illustrated in Fig. 16: at resonance (plain line), the signal's amplitude rests of the order of the millimeter over a large portion of the signal, allowing for a precise adjustment of the data. In contrast, at 15 % away from the resonance (dashed curve) the amplitude decreases ten times even before attaining the cylinder. This leaves most of the data below the threshold for detection. The corresponding reflection and transmission coefficients points have significant error bars but they have nevertheless been added to the resonance curves to illustrate the fact that they never overcome the values at resonance.

4.3.3. *Numerical study of the resonance*

An interesting feature is the marked asymmetry that is present in the resonance curves around their peak values. This corresponds to a behaviour which cannot be adequately described by means of the classical Breit-Wigner resonant shape. We have verified that this is not an experimental artifact by computing these coefficients numerically. For that purpose, we employed the PDEtools toolbox from MATLAB$^{\mathrm{TM}}$(finite difference scheme). We solve the Helmholtz equation $(\nabla^2 + k^2)\phi = 0$ with Neumann boundary conditions at the boundaries (walls and obstacle). The leading antisymmetric mode (with $\sin \pi y/2d$ transverse dependance) is imposed at the entrance. Then the transmitted and reflected wave are collected in the far field of the cylinder. This allows us to recover only the first evanescent mode, as the others (generated in the near field of the cylinder) decrease more rapidly with distance.

The asymmetry of the curves is recovered and follows the law given by:

$$T = \frac{B}{1 - C/\alpha d}, \tag{4.18}$$

where $\alpha d \equiv \sqrt{(\pi/2)^2 - (kd)^2}$. This relation was proposed by Granot (2002) for bound states in weakly bent waveguides. This equation has to be understood in the neighbourhood of the resonance in the complex k-plane, which means that the parameters B and C are only functions of the geometry. We have checked numerically that this is indeed the

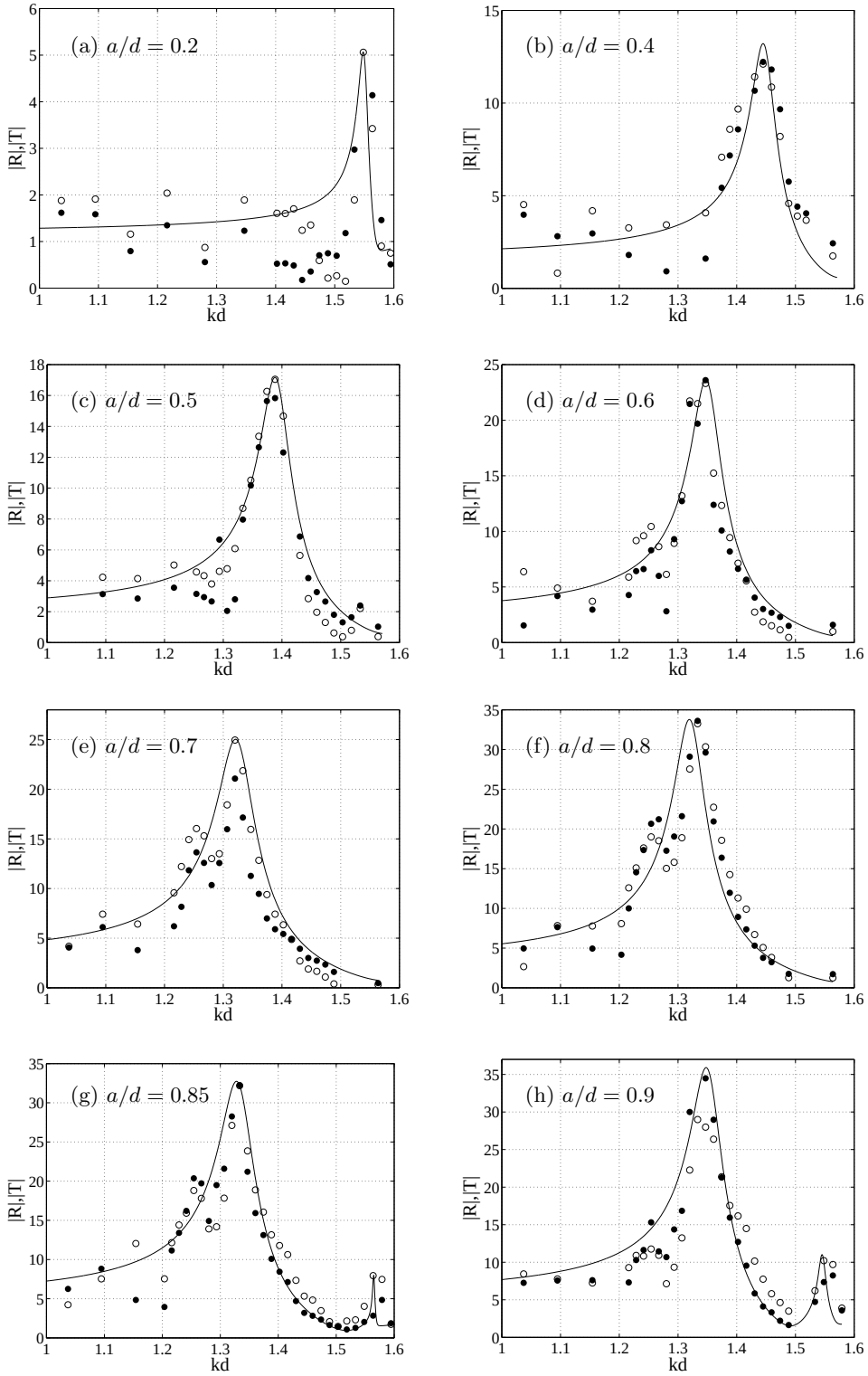


Figure 15: Resonance curves for several values of the aspect ratio a/d considered in this study. Full circles: reflection coeffient R; open circles: transmission coefficient. The continuous line represents the fit of the experimental data (see text for details).

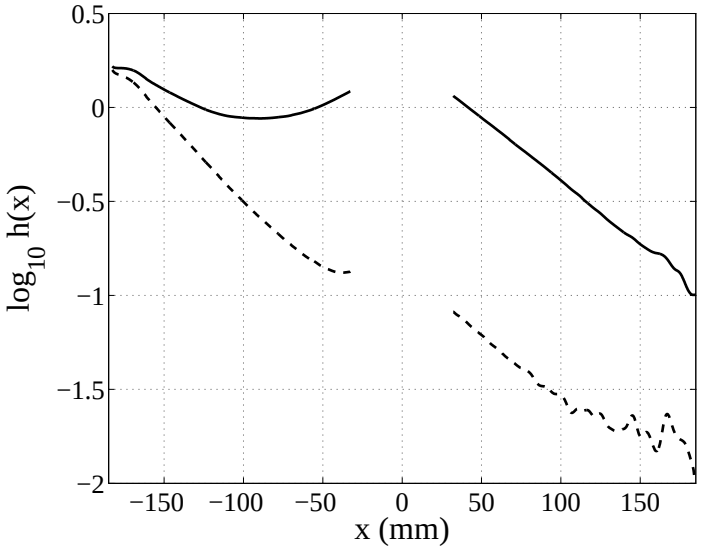


Figure 16: Comparison between two typical profiles of $h(x)$ employed for the determination of the reflection and transmission coefficients leading to the resonance curves shown in Fig. 15.

case employing different attenuation laws $\Im(k)$ in numeric calculations. The numerical curves, undistinguishable from the fitted law (4.18), are shown in plain line in Fig. 15 for each of the aspect ratios explored. For constructing these curves, the attenuation law must be known.

In the experiments a small attenuation is present that is modelised by a small imaginary part of k. This attenuation can only be roughly evaluated because of a low signal to noise ratio on the imaginary part of α even at resonance. The experimental measurements of α given through the relation $k = \sqrt{(\pi/2d)^2 - \alpha^2}$ an estimate of $\Im(k)d \sim 0.03$. As shown in Fig. 15 a good agreement is observed between the experimental data and theoretical prediction given by (4.18), for values of the attenuation coefficient consistent with this estimation for the single-peak resonance curves Figs. 15(a-f). For these curves the attenuation coefficient $\Im(k)d$ has been chosen within the range $[0.027, 0.03]$ for $a/d > 0.3$, whereas for smallest aspect ratios, $\Im(k)d \sim 0.01$ was observed to provide better results. For the doubly-peaked resonance curves shown in Fig. 15(g-h), the second resonance that is visible fact can be reproduced only assuming a significant decrease in the attenuation of about a factor of ten. Fig. 17 shows the dependence of the parameters B, C for both resonances as a function of the aspect ratio a/d. A simple fit for B gives $B = 1 + 1.35\,(a/d)^3$.

4.3.4. *Dependence on the geometry*

In this section we consider the dependance of the resonant trapped mode frequency on the obstacle's size. Fig. 18 shows the resonant frequencies $k_c d$ for each of the aspect ratios a/d studied. In the figure, open circles denote the experimental values corresponding to the maxima of the resonance curves previously obtained. There are two branches: the first (lower curve) correspond to trapped modes symmetric with respect to the Oy axis and the second to trapped modes antisymmetric with respect to the Oy axis (upper curve). The theoretical results are compared to the theoretical prediction by Callan *et al.* (1991) for the first branch, and with the theoretical prediction of Evans & Porter (1999) for

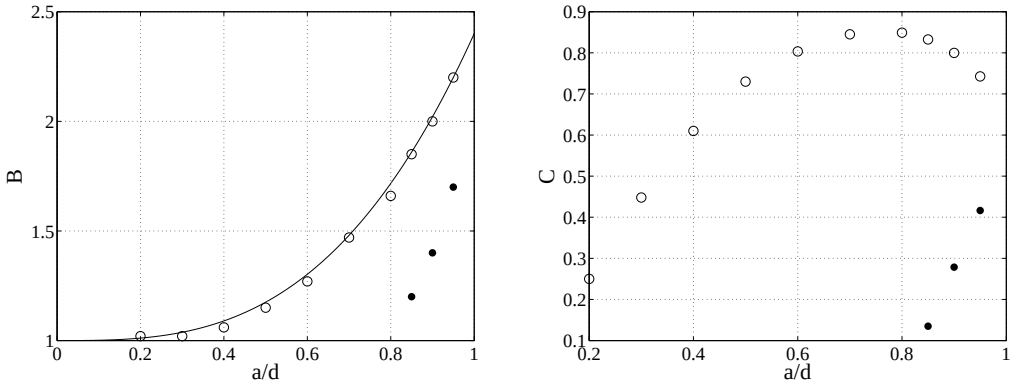


Figure 17: Parameters B, C of the transmission coeffient T in (4.18) at resonance as a function of a/d. Open circles correspond to the first resonance, whereas full circles denote the second resonance.

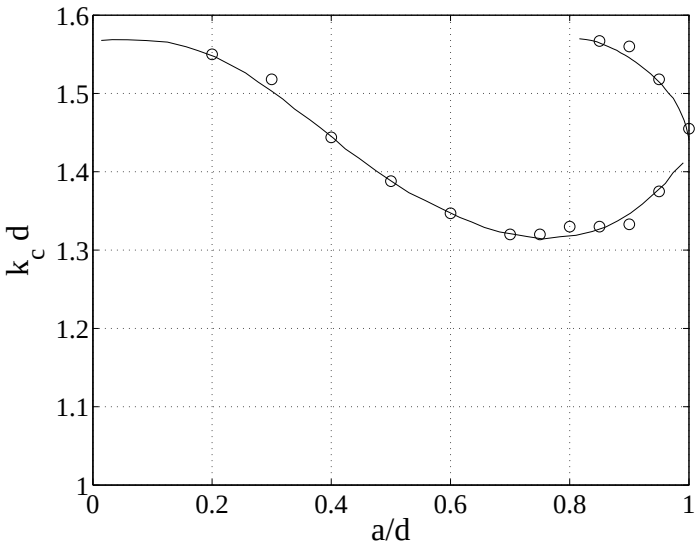


Figure 18: Variation of the trapped mode frequency parameter kd with a/d, the ratio of cylinder radius to channel half-width. The continuous line represents the theoretical predictions by Callan *et al.* (1991) (for NS-type trapped modes) and Evans & Porter (1999) (for NA-type trapped modes); dots summarize the experimental results obtained in this study for the two types of trapped modes observed.

the second branch. Evans & Porter (1999) predicted that the resonances of the second branch exist for $a/d \gtrsim 0.81$. This prediction is confirmed here. An excellent agreement is observed with the theoretical prediction for both branches.

4.3.5. *From trapped to edge mode*

The case of the totally obstructing cylinder $a/d = 1$ deserves closer inspection. In this case, the trapped mode becomes an edge mode. It corresponds to the degeneracy of the symmetric and antisymmetric trapped modes and thus to the intersection between the

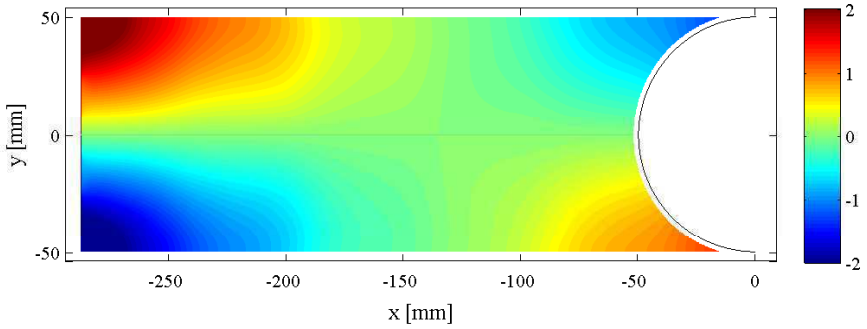


Figure 19: Edge mode experimentally observed for $a/d = 1$ and $kd = 144$. The position of the obstacle is indicated by the black circle. The scale of the colorbar is in mm.

two branches of resonance in Fig. 18. Experimentally, the resonance frequency of the edge mode is found at $kd = 1.44$. The corresponding pattern is shown in Fig. 19.

5. Summary and conclusions

In this study we have presented experimental evidence of the occurrence of trapped modes around a vertical surface-piercing circular cylinder placed symmetrically between the walls of a long but finite water waveguide. Using an optical profilometric technique, we were able to measure the space-time evolution of the free-surface deformation within the guide.

By decomposing the surface deformation in term of the harmonics of the driving frequency, we were able to isolate the dominant linear contribution from the higher order harmonics. Further separation of the free-surface deformation into symmetric and anti-symmetric parts with respect to the centerplane of the channel led us to the recovery of the detailed structure of the trapped mode.

The trapped mode spatial structure was determined for several aspect ratios a/d, and two types of trapped modes were observed. In particular, only one trapped mode of type NS was observed for each value of a/d explored within the frequency range (always below the waveguide's cutoff). A second trapped mode of type NA was observed for $a/d = 0.85, 0.90$ and 0.95, consistent with the theoretical predictions.

The detailed spatial structure of the experimentally observed trapped mode was compared to the predictions of a linear multipole expansion method, showing good overall agreement for various a/d.

For every value of a/d explored, the eigenfrequencies of the trapped modes were determined. To this end, one-dimensional reflection and transmission coefficients within the guide were introduced, allowing for the construction of resonance curves. It is worth noting that such a complete characterization of the scatterer system in terms of reflection and transmission coefficients is rather rare in practice due to the difficulties associated with their experimental determination. In these curves, the presence of a sharp peak evidences the occurrence of a trapped mode. Only for the largest cylinders these curves show two peaks, the second one corresponding to NA-type trapped modes.

Finally, all the results of the present study were summarized in a curve that shows the dependance of the trapped mode (adimensional) wavenumber $k_c d$ on the aspect ratio a/d. This curve is composed by two branches, corresponding to NS- and NA-type

trapped modes. Comparison to theoretical predictions available within the frame of the linear theory show excellent agreement for both branches.

Incidentally, the case for which the cylinder's diameter coincides with the waveguide's width, namely $a/d = 1$, is of particular interest as no theoretical predictions are available. In this case, the trapped mode becomes an edge mode, corresponding to the degeneracy of the symmetric and antisymmetric trapped modes and thus to the intersection of the two branches of resonance.

This work is supported by the ANR project ANR-08-BLAN-01108 Tourbillonde.

REFERENCES

Callan, M., Linton, C. M. & Evans, D. V. 1991 Trapped modes in two-dimensional waveguides. *J. Fluid. Mech.* **229**, 51–64.

Cobelli, P. J., Maurel, A., Pagneux, V. & Petitjeans, P. 2009 Global measurement of water waves by fourier transform profilometry. *Experiments in Fluids* **46**, 1037–1047.

Evans, D. V., Levitin, M. & Vassiliev, D. 1994 Existence theorems for trapped modes. *J. Fluid Mech* **261**, 21–31.

Evans, D. V. & Linton, C. M. 1991 Trapped modes in open channels. *J. Fluid Mech.* **225**, 153–175.

Evans, D. V. & McIver, P. 1991 Trapped waves over symmetric thin bodies. *J. Fluid Mech.* **223**, 509–519.

Evans, D. V. & Porter, R. 1997*a* Near-trapping of water waves by circular arrays of vertical cylinders. *Appl. Ocean Res.* **19**, 83–89.

Evans, D. V. & Porter, R. 1997*b* Trapped modes about multiple cylinders in a channel. *J. Fluid Mech.* **339**, 331–356.

Evans, D. V. & Porter, R. 1999 Trapping and near-trapping by arrays of cylinders in waves. *J. Eng. Math.* **35**, 149–179.

Evans, D. V. & Porter, R. 2002 An example of non-uniqueness in the two-dimensional linear water-wave problem involving a submerged body. *Proc. R. Soc. Lond. A* **454**, 3145–3165.

Granot, E. 2002 Emergence of a confined state in a weakly bent wire. *Phys. Rev. B* **65** (23), 233101.

Harter, R., Abrahams, I. D. & Simon, M. J. 2007 The effect of surface tension on trapped modes in water-wave problems. *Proc. R. Soc. A* **463**, 3131–3149.

Huntley, D. A. & Bowen, A. J. 1973 Field observations of edge waves. *Nature* **243**, 349–365.

Johnson, R. S. 2007 Edge waves: theories past and present. *Phil. Trans. R. Soc. A* **365**, 2359–2376.

Jones, D. S. 1953 The eigenvalues of $\nabla^2 u + \lambda u = 0$ when the boundary conditions are given in semi-infinite domains. *Proc. Camb. Phil. Soc.* **49**, 668–684.

Kuznetsov, N. G. & McIver, P. 1997 On uniqueness and trapped modes in the water-wave problem for a surface-piercing axisymmetric body. *Q. J. Mech. Appl. Math.* **50** (4), 565–580.

LeBlond, P. H. & Mysak, L. A. 1978 *Waves in the ocean*. Elsevier.

Linton, C. M. & Evans, D. V. 1992 Integral equations for a class of problems concerning obstacles in waveguides. *J. Fluid Mech.* **245**, 349–365.

Linton, C. M. & McIver, M. 2002 The existence of rayleigh–bloch surface waves. *J. Fluid Mech.* **470**, 85–90.

Linton, C. M. & McIver, P. 2001 *Handbook of Mathematical Techniques for Wave/Structure Interactions*. CRC Press.

Linton, C. M. & McIver, P. 2007 Embedded trapped modes in water waves and acoustics. *Wave motion* **45**, 16–29.

Maniar, D. H. D. & Newman, J. N. 1997 Waves diffraction by a long array of cylinders. *J. Fluid Mech.* **339**, 309–330.

Maurel, A., Cobelli, P. J., Pagneux, V. & Petitjeans, P. 2009 Experimental and theoretical inspection of the phase-to-height relation in fourier transform profilometry. *Applied Optics* **48**, 380–392.

McIver, M. 1996 An example of non-uniqueness in the two-dimensional linear water wave problem. *J. Fluid Mech.* **315**, 257–266.

McIver, M. 2000 Trapped modes supported by submerged obstacles. *Proc. R. Soc. Lond. A* **456**, 1851–1860.

McIver, M. & Porter, R. 2002 Trapping of waves by a submerged elliptical torus. *J. Fluid Mech.* **456**, 277–293.

McIver, P. 1991 Trapping of surface water waves by fixed bodies in channels. *Q. J. Mech. Appl. Maths* **44** (2), 193–208.

McIver, P. 2002 Wave interaction with arrays of structures. *Applied Ocean Research* **24**, 121–126.

McIver, P. & Evans, D. V. 1985 The trapping of surface waves above a submerged, horizontal cylinder. *J. Fluid Mech.* **151**, 243–255.

McIver, P. & McIver, M. 1997 Trapped modes in an axisymmetric water wave problem. *Q. J. Mech. Appl. Math.* **50** (2), 165–178.

McIver, P. & McIver, M. 2006 Trapped modes in the water-wave problem for a freely floating structure. *J. Fluid Mech.* **558**, 53–67.

McIver, P. & Newman, J. N. 2003 Trapping structures in the three dimensional water-wave problem. *J. Fluid Mech.* **484**, 283–302.

Retzler, C. H. 2001 Trapped modes: an experimental investigation. *Appl. Ocean Res.* **23**, 249–250.

Stokes, G. G. 1846 Report on recent researches in hydrodynamics. *Report to 16th Meeting Brit Assoc. Adv. Sci., Southampton, Murrey, London* pp. 1–20.

Takeda, M., Ina, H. & Kobayashi, S. 1982 Fourier-transform method of fringe-pattern analysis for computer-based topography and interferometry. *J. Opt. Soc. Am.* **72**, 156.

Takeda, M. & Mutoh, K. 1983 Fourier tranform profilometry for the automatic measurement of 3-d object shapes. *Appl. Opt.* **22**, 3977–3982.

Ursell, F. 1951 Trapping modes in the theory of surface waves. *Proc. Camb. Phil. Soc.* **47**, 1346–358.

Ursell, F. 1952 Edge waves on a sloping beach. *Proc. Roy. Soc. A* **214**, 79–97.

Ursell, F. 1987 Mathematical aspects of trapping modes in the theory of surface waves. *J. Fluid Mech.* **183**, 421–437.

CHAPTER 5

WAVE TURBULENCE IN A VIBRATING PLATE

This chapter is composed by an article submitted to publication in *Physical Review Letters* [12]. It concerns an experimental study regarding wave turbulence in a thin elastic plate subject to forced vibration, carried out in the frame of a joint collaboration with the *Laboratoire de Physique Statistique de l'École Normale Supérieure*.

Wave turbulence is a state of waves in non-linear interaction that has been observed for a large variety of physical systems, including (but not limited to) ocean waves, Alfvèn waves in solar winds, non-linear optics and superfluids. In a manner that is similar to the phenomenological theory of hydrodynamic turbulence, weak turbulence theory for wave turbulence predicts a Kolmogorov-Zakharov energy cascade. Moreover, this analytical theory assumes the persistence of the space-time structure of the linear waves through the dispersion relation.

Very few experimental studies have taken place and available results show only partial agreement with theory. Moreover, almost none of these experiments look beyond the analysis of single-point measurements, leading to limited statistics in terms of one-point spectrums.

In this study we present the results of an experimental study of wave turbulence of bending waves on a thin elastic plate subject to forced vibration. By using the optical profilometric technique developed during the course of this thesis (and described in detail in Chapters 2 and 3), the deformation of the plate's surface is measured simultanously in space and time.

The seed result of this chapter, from which all other results are drawn, is the determination of the 3D wavevector-frequency Fourier spectrum $E(\mathbf{k},\omega)$ of the plate's deformation velocity made possible by fully resolved space-time measurement of the plate's deformation. This constitutes, to our knowledge, the first experimental observation of such a space-time spectrum in wave turbulence.

Detailed analysis of the experimentally obtained 3D spectrum reveals the isotropy at large wave numbers, whereas the anisotropic response associated to the forcing is apparent at low wave numbers. Such a behaviour is expected in the phenomenology of Kolmogorov's energy cascade and is evidenced in this study: after a few steps in the cascade, the anisotropy of the forcing is forgotten down to the smallest scales at which the dissipation mechanisms are dominant.

Moreover, our results show that, in the 3D $(\mathbf{k},\omega)$ space, the energy of the motion is concentrated on a 2D surface that represents a non-linear dispersion relation, slightly deviated from its

linear counterpart for the bending waves in the plate. This is interpreted as strong evidence indicating that our system is indeed weakly non-linear. This result leads us to conclude that the quantitative disagreement between one-point spectrum and the predictions of the weak turbulence theory reported by Mordant [76], Boudaoud et al. [5] in previous studies cannot be attributed to the existence of strongly non linear structures. Instead, we advance the hypothesis that the aforementioned discrepancy could be due to a 'leakage' in the Kolmogorov-Zakharov cascade, *i.e.*, the presence of dissipative mechanisms operating at *all* scales.

Although some experiments directly measure the space spectrum, in most cases it is the motion at one given point as a function of time what is measured. In this latter case, only the time spectrum $E(\omega)$ can be calculated, and in order to compare with theoretical results, the space spectrum $E(\mathbf{k})$ is determined via the dispersion relation. In contrast, the global nature of our measuring technique enables us to *independently* estimate both $E(\omega)$ and $E(\mathbf{k})$. Moreover, such advantage allows us to assess the validity of the 'change of variables technique' described above (through either the linear or non-linear dispersion relation). In both cases, we are able to successfully reproduce the inertial range, with a rather better agreement when employing the non-linear dispersion relation. Large time and length scales are well reproduced only when using the non-linear relation, therefore validating the usual change of variables when the non linearities are weak.

Furthermore, the observed localization of the energy in the spectrum allows us to confirm the premise of weak turbulence theory: the persistence of the space-time structure of waves. In addition, the study presented in the following chapter confirms and quantifies the weakly non-linear behaviour of the waves comprising the turbulent cascade. Overcoming the discrepancies between experiments and theory claimed previously, we show some agreement between experimental results and wave turbulence theory.

We anticipate that this experiment will allow for precise and quantitative comparisons with theoretical investigations of wave turbulence of prime importance for the large number of turbulent systems in which extensive measurements are out of reach.

Beyond the results that are valuable to the wave turbulence community, there is another aspect to this study that is of significant importance in assessing the capabilities of our optical profilometric measuring technique.

In contrast to the surface waves considered in previous chapters, bending waves in a plate propagate much faster. In experimental terms, this poses a rather strong restriction on the measurement times, which should be short enough in order to assure that the surface under study does not evolve significatively in the interval the measurement is performed. Moreover, preliminary experiences showed that the amplitude of the driving vibration must be kept small for the plate dynamics to remain within the linear regime, otherwise it would rapidly become fully nonlinear. Successfully dealing with this limitation depends on the sensibility of the measuring system: it should be capable of detecting such low-amplitude vibrations (of the order of 0.5 mm in the present case). An additional experimental difficulty arises from the consideration of the wavelength range physically significative for this problem. The energy cascade's inertial range corresponds roughly to wavelengths between 5 and 20 cm, therefore requiring the use of an observation window of at least 40^2 cm^2 so as to capture a minimum of two wavelengths of the largest waves in the plate.

From these remarks it becomes evident that obtaining space-time resolved measurements of the waves' propagation and mutual interaction in the plate represents a true challenge to any experimental technique. However, by careful selection and precise tunning of the measurement system's parameters (such as the relative positioning of the projection–recording system, the size of

the projection and observation windows and the spatial frequency of the projected pattern) we were able to obtain the fully space-time resolved measurements that constitute the keystone of this study.

In this measurement campaign, the system's setup employed allowed us to obtain several series of measurements over large areas on the plate's surface (between 60^2 and 70^2 cm^2), using high spatial resolutions (800^2–1000^2 px^2) and at considerably high acquisition rates (1300–2600 fps).

These measurements, and the results derived from them, effectively illustrate the capabilities of our optical profilometric technique, showing both its versatility for the application to systems other than water waves and its adaptability to more experimentally demanding scenarios.

Wave turbulence served up on a plate

Pablo Cobelli, Philippe Petitjeans
Physique et Mécanique des Milieux Hétérogènes, ESPCI & CNRS, 10 rue Vauquelin, 75005 Paris, France.

Agnès Maurel
Laboratoire Ondes et Acoustique, ESPCI & CNRS, 10 rue Vauquelin, 75005 Paris, France.

Vincent Pagneux
Laboratoire d'Acoustique de l'Université du Maine & CNRS, Le Mans, France.

Nicolas Mordant*
Laboratoire de Physique Statistique, Ecole Normale Supérieure & CNRS, 24 rue Lhomond, 75005 Paris, France.

Wave turbulence in a thin elastic plate is experimentally investigated. By using a Fourier transform profilometry technique, the deformation field of the plate surface is measured simultaneously in time and space. This enables us to compute the wavevector-frequency Fourier $(\mathbf{k},\omega)$ spectrum of the full space-time deformation velocity. In the 3D $(\mathbf{k},\omega)$ space, we show that the energy of the motion is concentrated on a 2D surface that represents a nonlinear dispersion relation. This nonlinear dispersion relation is close to the linear dispersion relation. This validates the usual wavenumber-frequency change of variables used in many experimental studies of wave turbulence. The deviation from the linear dispersion, which increases with the input power of the forcing, is attributed to weak non linear effects. Our technique opens the way for many new extensive quantitative comparisons between theory and experiments of wave turbulence.

PACS numbers: 46.40.-f,62.30.+d,05.45.-a

Wave turbulence is a state of waves in non-linear interaction as observed for a large variety of systems including Alfven waves in solar winds [1, 2], ocean waves [3], non linear optics [4] and superfluids [5]. Similarly to the phenomenological theory of hydrodynamic turbulence, the so-called weak turbulence (WT) theory for wave turbulence predicts a Kolmogorov-Zakharov energy cascade [6]. This analytical weak turbulence theory assumes the persistence of the space-time structure of the linear waves through the dispersion relation. Very few experimental studies have taken place and results show only partial agreement with theory [7–10]. Furthermore, almost none of these experiments look beyond the analysis of measurement at a single point. Here we report the analysis of the turbulence of bending waves on a shaken, thin elastic plate, a phenomenon used in theatres to simulate the sound of thunder. We are able to measure the fully resolved space-time dynamics of the deformation of the plate and we show that the energy is localized on a line in the wavenumber-frequency plane of the Fourier spectrum. This confirms the persistence of the space-time structure of waves which is the premise of weak turbulence theory. In addition, our system displays the phenomenology described by the theory and yet some of its predictions are not quantitatively fulfilled: the non-linear shift to the dispersion relation and the power spectrum do not obey the predicted scaling laws.

The theory of WT relies on the assumption of weak non linearity of waves. The latter induces a scale separation in the time evolution of the wave amplitude compared to the wave period and it provides a natural closure of the hierarchy of cumulants derived from the wave equation [6, 11]. In contrast, no such closure can be exhibited for hydrodynamic turbulence. In particular, the WT theory of wave turbulence leads to a kinetic equation for the evolution of the energy spectrum of the waves. Stationary solutions are exhibited which corresponds to the Rayleigh-Jeans spectrum for systems in equilibrium and the Kolmogorov-Zakharov energy cascade for non-equilibrium systems. This prediction of the power spectrum density of the wave amplitude has been derived in many cases such as non linear optics, superfluids, gravity-capillary water waves, sound waves, Alfven waves, plasmas, oceanography, semiconductor lasers and bending waves in elastic plates [6, 11, 12]. There are a paucity of experiments specifically designed for wave turbulence and of those, most concern surface waves on liquids [7, 8]. Our wave system consists of a thin steel plate on which elastic bending waves are excited by an electromagnetic vibrator. The dynamics of the plate follow the Föppl-Von Karman equations for the deformation:

$$\rho\frac{\partial^2\zeta}{\partial t^2} = -\frac{Eh^2}{12(1-\sigma^2)}\Delta^2\zeta + \{\zeta,\chi\} \qquad (1)$$

$$\frac{1}{E}\Delta^2\chi = -\frac{1}{2}\{\zeta,\zeta\} \qquad (2)$$

where ρ is the density, ζ the plate deformation, E the Young's modulus, σ the Poisson ratio, Δ the Laplacian operator, χ the stress function and $\{.,.\}$ is a bilinear differential operator [12]. Linearizing the first equation

in (1) provides the linear dispersion relation

$$\omega_k = \sqrt{\frac{Eh^2}{12\rho(1-\sigma^2)}}k^2\,. \qquad (3)$$

The non linear term in (1) is due to the stretching of the plate and it is cubic in the wave amplitude. The WT theory has recently been applied to this case [12] and predicts a space Fourier spectrum of the amplitude of the waves

$$E_\zeta(k) = C\frac{P^{1/3}}{(12(1-\sigma^2))^{1/6}}\frac{\ln^{1/3}(k^\star/k)}{\sqrt{E/\rho}\,k^3} \qquad (4)$$

where P is the average power input in the system from the applied forcing, C is a number and $k^\star$ is a cut-off frequency. The one-point spectrum of the waves has been investigated experimentally [9, 10] and has been shown not to obey the WT prediction in particular in its scaling in P :

$$E(k) \propto \frac{P^{0.7}}{k^4} \qquad (5)$$

Nevertheless, it displays a turbulent-like behaviour , i.e. a broadband spectrum, and the question is raised whether or not the disagreement with the theory is due to strongly non linear structures, to boundary condition effects or to some dissipative mechanism.

A sketch of the experimental setup is shown in fig. 1(a). The plate is made of stainless steel and its size is 2 m by 1 m and 0.4 mm thick. Its is bolted on a I beam by one short end and is hanging under its own weight. An electromagnetic vibrator is anchored 40 cm from the bottom of the plate and excites the waves at 30 Hz with a varying amplitude. The vibrator is fitted with a FGP sensors force probe and Brüel & Kjaer accelerometer to measure the input power P. A Fourier transform profilometry technique [13, 14] gives access to the temporal evolution of the deformation of the plate measured over a significant portion of its area. The principle is the following: a sine intensity pattern $I(x,y) \propto \sin(2\pi y/p)$ is projected on the surface of the plate by a videoprojector. The pattern is then recorded by a Phantom v9 high speed camera. The deformation of the plate induces a phase shift of the pattern recorded by the camera. The deformation of the plate is recovered by a 2D phase demodulation of each image in the movie [13, 14]. Movies are recorded either with 1000^2 (resp. 800^2) pixels at 1300 (resp. 2600) frames per seconds (fps). The configuration and the processing is similar to that of Cobelli et al. [13] with a distance of $L = 193$ cm from the projector to the plate and a distance of $D = 35$ cm between the optical axes. The normal velocity of the plate is obtained by differentiating the deformation movie in time. The field of view is about 71^2 cm^2 at 1300 fps and 62^2 cm^2 at 2600 fps. The spectra are calculated by performing

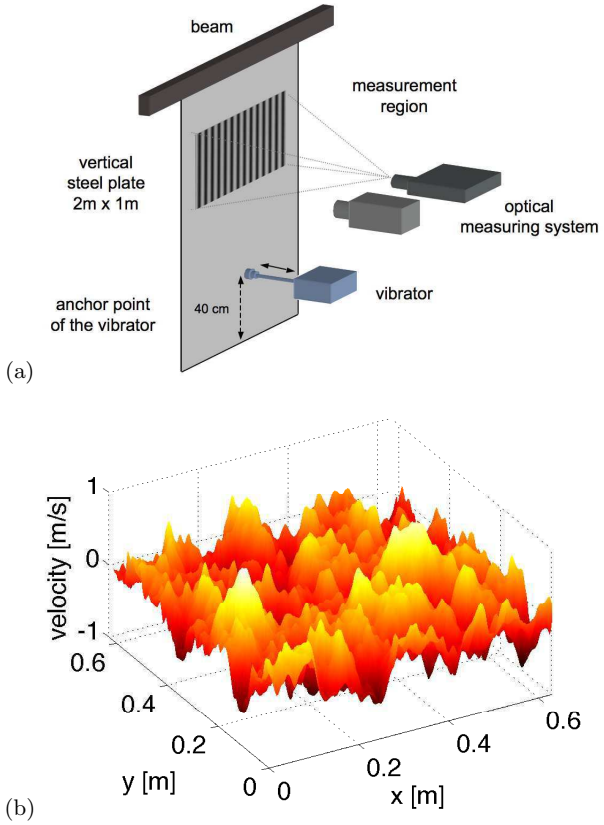


FIG. 1: (a) Sketch of the wave turbulence experiment. The specifically designed 2D mechanical system is made of a 2×1 m^2, 0.4 mm thick stainless steel plate held vertically and set in motion by an electromagnetic vibrator at 30 Hz. The Fourier Transform profilometry is based on the projection of a sine intensity pattern by a high definition video projector. The deformed image is then recorded by a high speed camera (1300 or 2600 fps). (b) Example of measurement of the deformation velocity on a 63 cm by 62 cm area.

a multidimensional Fourier transform without applying any windowing to preserve the localization of the energy in the Fourier space. An example of the normal velocity of the plate is displayed in fig. 1.

The full space-time Fourier spectrum (shown in fig. 2(a)) of the deformation $E(\mathbf{k},\omega)$ (a function of both the wave vector $\mathbf{k}$ and the frequency ω) is constructed from the movie of the deformation velocity. The striking feature is the localization of the energy in the vicinity of a surface showing that the motion is a non linear superposition of waves following a dispersion relation $\omega = f(\mathbf{k})$, close to the linear dispersion relation. This is the first experimental observation of such a space-time spectrum in wave turbulence. In addition to the full space-time spectrum, we can analyse the space spectrum $E(\mathbf{k})$, as displayed in fig. 2(b). The isocontours for large wave numbers are circles, revealing the isotropy of the spec-

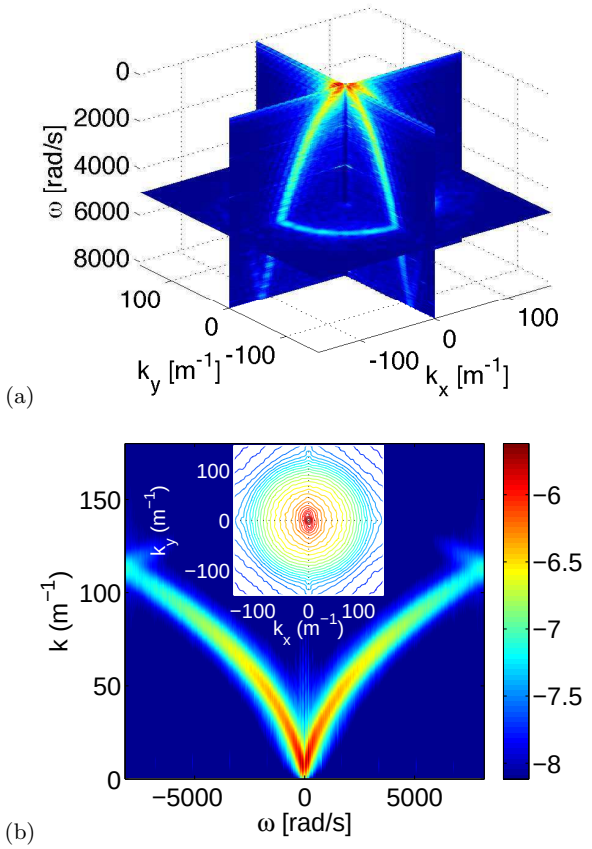


FIG. 2: (a) Space-time spectrum $E(\mathbf{k},\omega)$ of the deformation velocity (colors are log scaled). The cuts are located at $k_x = 0$, $k_y = 0$ and $\omega = 5000$ rad/s. The energy is localized on a surface in the $(\mathbf{k},\omega)$ space which confirms that the turbulent motion is due to a non linear superposition of waves following a dispersion relation. (b) Spectrum $E(k,\omega)$ obtained from $E(\mathbf{k},\omega)$ by integrating over the direction of $\mathbf{k}$. Insert: space spectrum $E(\mathbf{k})$ computed from $E(\mathbf{k},\omega)$ by summing over the frequencies. Contours are log scaled in both plots.

trum in this regime. The anisotropic response to the forcing is visible at low wave numbers. This behaviour is expected in the phenomenology of the Kolmogorov cascade of energy and is evidenced here: After a few steps in the cascade, the anisotropy of the forcing is forgotten down to the small scales at which the dissipation is dominant. Owing to the isotropy of the spectrum, in fig. 2(b) we show the spectrum $E(k = \|\mathbf{k}\|,\omega)$ obtained by integrating $E(\mathbf{k},\omega)$ over all the directions of the wave vector. The localisation of the energy appears as a line in the (k,ω) plane. The width of this line is close to the inverse of the image size, which indicates that the localization of the energy in our measurement is actually limited by the resolution of the Fourier transform due to the finite size of the plate. At low frequency, the injection of energy corresponds to a peak on the energy line: even though the forcing is localized in space, its monochromatic nature (at 188 rad/s) makes it local in the (k,ω) plane. The forcing operates effectively at low frequency and at low wavenumber as is expected in the phenomenology of the Kolmogorov-Zakharov cascade.

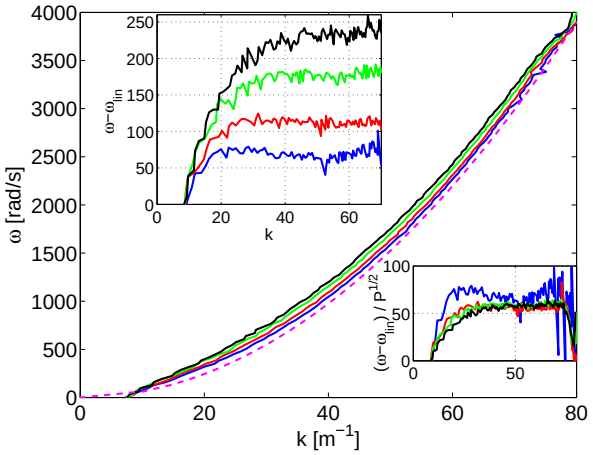


FIG. 3: Non linear dispersion relation $\omega(k)$ computed from the line of maximum energy in the space-time spectrum of the plate deformation velocity for various input power P of the forcing (from bottom to top $P^{1/2} = 1, 2, 3, 4$ in arbitrary units). The dashed line is the linear dispersion relation (3). A systematic shift is observed which increases with the forcing power. The top insert shows the deviation from the linear dispersion. At high wave numbers, the shift is seen to be independent of k. The bottom insert shows the shift normalized by $P^{1/2}$.

The concentrated line of energy in the spectrum $E(k,\omega)$ allows the dispersion relation to be computed; it is extracted by computing the position of the crest of the energy line at each frequency and is displayed in fig. 3 for various values of the forcing P. The dispersion relation remains close to the linear dispersion relation with a small but systematic shift. This provides strong evidence that our system is indeed weakly non linear. Thus, the quantitative disagreement between the one point spectrum and the WT theory prediction [9, 10] cannot be attributed to the existence of strongly non linear structures. Instead, the disagreement is proposed to be attributed to the dissipative mechanisms which are believed to exist at all scales rather than being present at only small scales; hence the Kolmogorov-Zakharov cascade is "leaking" [15].

Figure 3 allows us to quantify the departure of the observed dispersion relation from the linear one. Notably, it is shown that the correction increases with the power input P with a behaviour close to $P^{1/2}$ behaviour. It is also observed to be constant at high wavenumbers so that the various dispersion relations are parallel to one another.

This behaviour is of particular interest when compared with the WT prediction. Indeed, it is expected that the departure of the dispersion relation from the linear one has a power law scaling in P which is identical to the scaling for the energy spectrum [16]. Our experimental measurements confirm this prediction: the exponent close to 1/2 in P is common to both departure from linearity in the dispersion relation and also to the energy spectrum.

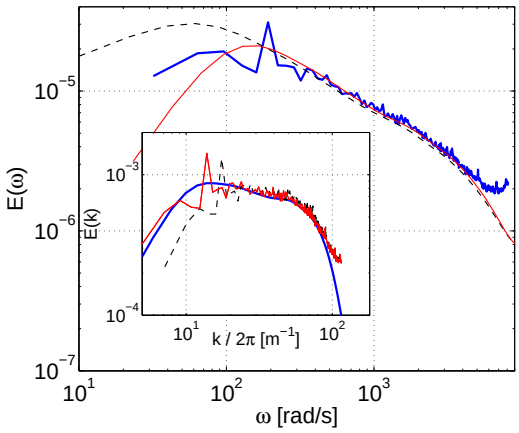


FIG. 4: Test of the validity of the change of variable $k \leftrightarrow \omega$ using the dispersion relation. Solid blue line: direct measurement of the time spectrum $E(\omega)$ – solid red (resp black dashed) line: $E(\omega)$ computed from the space spectrum $E(k)$ using the nonlinear (resp. linear) dispersion relation to change variable. Insert: same for the space spectrum $E(k)$. Solid blue line: direct estimation of $E(k)$ – red (resp black dashed) line: $E(k)$ computed from $E(\omega)$ by the change of variable using the nonlinear (resp. linear) dispersion relation.

The application of the WT turbulence theory is often restricted to the prediction of the Kolmogorov-Zakharov space spectrum $E(k)$. Although some experiments directly measure the space spectrum [17, 18], it is often easier to measure the motion at one given point as a function of time. In that case, only the time spectrum $E(\omega)$ can be estimated. To compare with the theory, the space spectrum is determined by using the dispersion relation to obtain $E(k)$ from $E(\omega)$ [7, 8, 19]. This approach was used to deduce the law in Eq. (5) [9, 10]. We can independently estimate both $E(\omega)$ and $E(k)$ directly. We can assess the validity of the change of variables technique above (via the linear or non linear dispersion relation). The comparison of the various cases is shown in fig. 4. Both dispersion relations allow us to reproduce the inertial range, with a better agreement shown when using the non linear relation. The large time or length scales are well reproduced only when using the non linear dispersion relation. This validates the usual change of variables when the non linearity is weak.

Our experimental approach of wave turbulence reveals the main features of the weakly coupled waves that can be usefully compared with weak turbulence theory. Until now, only the spectrum $E(k)$ has been compared with theoretical prediction. However, WT theory can go far beyond spectra predictions: it gives quantitative predictions for multipoint statistics. Our present study confirms and quantifies the weakly nonlinear behaviour of the waves comprising the turbulent cascade. It confirms that the scaling law in the supplied power P is the same for the departure from the linear dispersion relation and also for the energy spectrum. Overcoming the discrepancy between experiments and theory claimed previously, we have shown some agreement between experimental results and WT theory. We anticipate that this experiment will allow precise and quantitative comparisons with theoretical investigations of wave turbulence [6, 20, 21] of prime importance for the large number of turbulent systems in which extensive measurements are out of reach.

N.M. thanks Agence Nationale de la Recherche for its funding under grant TURBONDE BLAN07-3-197846.

* nmordant@ens.fr

[1] C. S. Ng and A. Bhattacharjee, Astrophysical Journal **465**, 845 (1996).
[2] S. Galtier, S. V. Nazarenko, A. C. Newell, and A. Pouquet, J. Plasma Phys. **63**, 447 (2000).
[3] K. Hasselmann, J. Fluid Mech. **12**, 481 (1962).
[4] S. Dyachenko, A. C. Newell, A. Pushkarev, and V. E. Zakharov, Physica D **57**, 96 (1992).
[5] V. S. L'vov, S. V. Nazarenko, and O. Rudenko, Phys. Rev. B. **76**, 024520 (2007).
[6] V. E. Zakharov, V. S. L'vov, and G. Falkovich, *Kolmogorov Spectra of Turbulence* (Springer, Berlin, 1992).
[7] P. Denissenko, S. Lukaschuk, and S. Nazarenko, Phys. Rev. Lett. **99**, 014501 (2007).
[8] E. Falcon, C. Laroche, and S. Fauve, Phys. Rev. Lett. **98**, 094503 (2007).
[9] N. Mordant, Phys. Rev. Lett. **100**, 234505 (2008).
[10] A. Boudaoud, O. Cadot, B. Odille, and C. Touzé, Phys. Rev. Lett. **100**, 234504 (2008).
[11] A. C. Newell, S. Nazarenko, and L. Biven, Physica D **152-153**, 520 (2001).
[12] G. Düring, C. Josserand, and S. S. Rica, Phys. Rev. Lett. **97**, 025503 (2006).
[13] P. J. Cobelli, A. Maurel, V. Pagneux, and P. Petitjeans, Exp. Fluids **46**, 1037 (2009).
[14] A. Maurel, P. Cobelli, V. Pagneux, and P. Petitjeans, Applied Optics **48**, 380 (2009).
[15] C. Josserand, Private communication.
[16] G. Düring and S. Rica, Private communication.
[17] W. B. Wright, R. Budakian, D. J. Pine, and S. J.Putterman, Science **278**, 1609 (1997).
[18] D. Snouck, M. T. Westra, and W. van de Water, Phys. Fluids **21**, 025102 (2009).
[19] E. Henry, P. Alstrøm, and M. T. Levinsen, Europhys. Lett. **52**, 27 (2000).

[20] E. A. Kartashova, Phys. Rev. Lett. **72**, 2013 (1994).
[21] O. M. Philips, J. Fluid Mech **156**, 505 (1985).

CHAPTER 6

CONCLUSIONS AND PERSPECTIVES

6.1 Summary and conclusions

This thesis presents a contribution to the understanding of water waves phenomena, introducing a number of results of interest in current research. It is mainly concerned with the experimental study of wave interaction through the measurement of the free surface deformation both in space and time.

The first important result arising from this work is the development of a versatile experimental technique that allows for high-resolution single-shot global measurement and time-tracking of free surface deformations; overcoming a need which, at the time, appeared as a serious obstacle imparing further development in this field. This optical profilometric technique is based on the principle of fringe projection profilometry. A fringe projection pattern of known spatial frequency is projected onto the liquid's free surface by means of a digital videoprojector and its image is recorded by a camera. The topography of the surface introduces a frequency modulation in the observed pattern, which is also modified by the perspective due to the relative positioning and orientation of the projection–recording system. The deformed fringe pattern is later compared to the undeformed (reference) one, leading to a phase map from which the free surface can be reconstructed by means of a so-called 'phase-to-height relation' derived from the system setup through geometrical optics.

Fringe projection profilometry has been sucessfully employed in the past for the topography of solid surfaces in a variety of fields, such as 3D sensing systems, mechanical engineering, machine vision, robotic control, industry monitoring and quality assessment and biomedicine. In this work we developed the liquid surface extension of this technique, and we introduced several significant improvements to the optical setup, as well as to the signal processing algorithms.

In order to be able to project images onto the liquid surface, its light difussivity is enhanced by the addition of a white liquid dye. It is worth highlighting that, even though the use of dye renders the liquid opaque, precluding the simultaneous use of introspective optical techniques (such as Particle image Velocimetry and Laser Doppler Velocimetry), bulk measurements are still

possible using acoustic techniques (such as Ultrasonic Doppler Velocimetry). A high-contrast & high-resolution videoprojector is employed for the projection of fringes onto the surface, allowing for the projection of wavelength-controlled sinusoidal-profile fringe patterns, increasing considerably the overall performance of the technique and the quality of the reconstruction.

The system's resolution (both in-plane and vertical) is given by the physical size of the projected pixel onto the undeformed (reference) surface, a fact that was confirmed experimentally by testing against an standard point laser displacement sensor.

Another characteristic of this technique lies in the fact that, besides the reference image, only one image (that of the deformed fringe pattern) is needed to achieve a reconstruction of the associated free surface. Through this single-shot feature, the technique poses, bit itself, no restrictions on the time-tracking of the free-surface deformation (other than that arising from the exposure time). Therefore, the obtention of time-resolved measurements of the surface's evolution is only limited by the capturing system's acquisition rate.

Moreover, careful consideration of the profilometric reconstruction formulas commonly used in the literature regarding FTP led us to realize an error in their derivation. This finding motivated a theoretical and experimental study (described in Chapter 3) in which we were able to confirm and provide experimental evidence for this error. More importantly, this study was the first to provide for both exact (within the approximation of geometrical optics) and experimentally validated reconstruction formulas for the different geometries and configurations in which the system can be used for the profilometry of the free surface (namely, parallel- and crossed-optical axes; collimated and non-collimated projections). As a final remark, it is worth highlighting that the range of applicability of these results extends well beyond the limits of FTP, to include all profilometric methods based on fringe projection.

The development of this experimental technique represented a landmark for all the subsequent work carried out in the framework of this thesis. Preliminar applications of this technique to fluid dynamics' scenarios of interest in current research include the measurement of spiral waves spontaneously emitted by a pinned vortex in fast rotation, and the study of the vortex–surface-wave interaction. The results obtained in these case studies served also as an early illustration of the large scope of applicability of this technique.

Next, we turned our attention to the study of trapped mode resonances in water waves, a problem of interest due to its large potential for technological applications, ranging from the design of metamaterials to coastal engineering. In particular, we considered water wave trapped modes occurring in the vicinity of a vertical surface-piercing cylinder placed symmetrically between the parallel walls of a long but otherwise finite water waveguide of constant depth. In this configuration, a significant number of values of the geometrical control parameter of the problem, namely the aspect ratio between the obstacle's diameter and waveguide's width, were explored. Our optical profilometric technique was used to obtain space-time resolved measurements of the free-surface deformation within the waveguide excited by (forcing) incident waves. In the context of this study, we have reached a number of novel results worth highlighting.

Firstly, the occurrence of trapped modes in this water wave scenario was experimentally observed in the form of non-propagative oscillations of the free surface localized in the neighbourhood of the cylinder, antisymmetric with respect to the longitudinal axis of the waveguide. Decomposition of the surface deformation in harmonics of the driving frequency for every sampled

point over the surface allowed for the separate analysis of the linear and non-linear components. Comparison showed that the dynamics of the free surface is dominated by the linear contribution, therefore validating the use of theoretical models based on linear water wave theory.

The pure trapped modes' spatial structure was obtained from by the subsequent separation of the linear deformation field in terms in terms of the natural symmetries of the problem. The spatial structure of the trapped mode was studied in detail and successfully compared to the theoretical predictions arising from a multipole expansion method.

From the analysis of the spatial structure of the trapped mode resonances we were able to identify two different types of trapped modes: either symmetric (termed NS-type trapped modes) or antisymmetric (NA-type modes) with respect to an axis perpendicular to the waveguide walls and passing through the obstacle's center. Although never observed before, NA-type trapped modes were numerically predicted to exist only for the largest aspect ratios; lower values being only associated with a NS-type trapped mode. The range of values of the aspect ratio for which this second type of trapped mode was observed in our experiences confirms those predictions.

The trapped modes' eigenfrequencies were determined by treating the system as a scattering problem in the far field. The introduction of one-dimensional reflection and transmission coefficients allowed the construction of experimental resonance curves characterising the frequency behaviour of the modes for every value of the aspect ratio considered. As a side note, it is worth mentioning that this description of the system in terms of resonance curves amounts to the complete characterization of the system as a scatterer, which is rather rare in practice due to the difficulties associated with their experimental determination.

For a particular frequency, the occurrence of a trapped mode is evidenced in the resonance curves by a peak in the reflection–transmission coefficients. Only one peak is observed in most resonance curves, associated with a NS-type trapped mode. For the largest aspect ratios considered, the associated resonance curves showed the presence of two peaks, consistent with the additional occurrence of a NA-type trapped mode. In any case, these curves present a marked asymmetry around the peak values, which cannot be adequately described by the classical Breit-Wigner formula. In order to reproduce this experimental behaviour, a model is proposed which takes account of the proximity to the waveguide's threshold for propagation and its influence on the frequency dependence of the scattering data. This model enabled us to reproduce the asymmetry of the resonance curves and was successfully validated with the experimental results.

Finally, all the experimental results obtained during the course of this study are summarized in the form of a master curve, depicting the dependence of the trapped mode frequency with the aspect ratio. Two branches, corresponding to NS- and NA-type trapped modes, are present in this curve. Comparison to theoretical predictions available (only) within the frame of the linear theory showed excellent agreement for both branches. Incidentally, our study shows that, when the cylinder's diameter equals the waveguide's width (a case for which no theoretical predictions are available) the associated trapped mode becomes and edge mode, corresponding to the degeneracy of the symmetric and antisymmetric trapped modes, *i.e.*, to the intersection of the two branches of resonance on the master curve.

As a closing remark, we would like to point out that the results obtained in the frame of this study represent a significant advance in the understanding of trapped modes in water waves. It constitutes, to our knowledge, the first experimental investigation to provide a complete characterization of the trapped modes in frequency space, as well as to present a detailed analysis of their spatial structure.

The last experimental study carried out during the course of this thesis is concerned with wave turbulence, a state of waves in non-linear interaction that has been observed in a large variety of physical systems, including gravity-capillary water waves, ocean waves, superfluids, Alfvén waves astrophysical plasmas, semiconductor lasers and non-linear optics.

As in the case of the phenomenological theory of hydrodynamical turbulence, weak turbulence theory for wave turbulence predicts a Kolmogorov-Zakharov energy cascade. Moreover, this analytical theory assumes the persistence of the space-time structure of the linear waves through the dispersion relation. Contrary to hydrodynamical turbulence (either 2D or 3D), however, only few experimental studies exist of wave turbulence, and available results only show partial agreement with theory. Moreover, the vast majority of these experiments are restricted to one- or two-point measurements, leading to limited statistical descriptions. In particular, prior to the present study, only the space energy spectrum has been compared with the theory. However, weak turbulence theory goes well beyond spectral predictions, allowing quantitative determination of multi-point statistics.

In the framework of this study, we focus on the analysis of turbulence of bending waves on a shaken, thin elastic steel plate, a phenomenon commonly used in theatres to simulate the sound of thunder. Our optical profilometric (described in Chapters 2 and 3)technique is used to measure the plate's surface deformation in space and time, overcoming the limitations of previous experimental studies.

The most important result of this study is, without doubt, the experimental determination of the 3D wavevector-frequency Fourier spectrum of the plate's deformation velocity, made possible by the fully resolved space-time measurements of the plate's deformation provided by our profilometric technique. This constitutes, to our knowledge, the first experimental observation of such a space-time spectrum in wave turbulence. All other results of this study are drawn from the subsequent detailed analysis of this 3D spectrum.

As a first result from its analysis, and consistly with the phenomenology of Kolmogorov's energy cascade, the 3D spectrum reveals isotropy at large wave numbers, whereas anisotropy associated to the forcing is only apparent at low wave numbers.

Furthermore, our results showed that, in the 3D wavenumber-frequency space, the energy of the motion is concentrated in the vicinity of a 2D surface, confirming the persistence of the space-time structure of waves. In addition, it was observed that such 2D surface represents a non-linear dispersion relation slighlty deviated from its linear counterpart for bending waves in the plate. This weak non-linearity led us to conclude that the quantitative disagreement between one-point spectrums and the predictions of weak turbulence theory reported in previous studies could not be attributed, as was proposed, to the presence non-linear structures. Instead, we propose a plausible alternative explanation of the discrepancy by admitting the existence of dissipative mechanisms operating at all scales.

It is worth mentioning, however, that although our system displays the phenomenology described by the theory, some of its predictions are not quantitatively fulfilled and remain as open questions to be addressed by subsequent studies. This is the case for the non-linear shift to the dispersion relation and the power spectrum, which do not obey the predicted scaling laws.

Our experimental approach for wave turbulence successfully revealed the main features of the weakly coupled waves that can be usefully compared with the predictions of weak turbulence theory. This study confirmed and quantified the weakly non-linear behaviour of the waves comprising the turbulent cascade. Moreover, our results confirmed that the scaling law in the supplied power is the same for the departure from linearity and also for the energy spectrum. Overcoming the discrepancy between experiments and theory claimed in previous studies, we have shown some

agreement between experimental results and weak turbulence theory.

6.2 Perspectives

The development of the optical profilometric technique for the measurement of the free-surface deformation presented in this thesis widens the horizon of potential experiences in water waves, motivating the exploration of a variety of interesting surface phenomena in a manner that was previously unavailable. Among these, we would like to point out four specific problems that are of major relevance to current research.

The first of these experimental challenges consists in the study of the time reversal of water waves using only a single element. Similarily to the experiments performed by Draeger and Fink [20] in silicon wafers, we propose the water wave analogue by considering a chaotic surface-wave cavity with negligible absorption. Using our profilometric technique, the deformation of the free surface within the cavity could effectively be measured and, the time-reversed signal, now available at any sampled point over the surface, could be reinjected at the same position.

The impact of drops onto thin liquid films constitutes another physical system of interest. In this case, we are interested in the bowl-shaped thin crown that is formed inmediately after the impact. This crown subsequently expands outwards and finally breaks. Although our technique would not be capable of reproducing the splasing phase, it could indeed prove to be very useful in the characterization of the expansion stage. The first step towards the characterization of this expansion would therefore involve an experimental determination of the crown's spreading velocity.

Stimulated by the promising results obtained on the emission of spiral waves a pinned vortex in fast rotation (shown in Chapter 2), we propose to perform a more detailed characterization of this phenomenon. Such an experimental investigation could also be complemented with the study of the interaction of the vortex core with short surface wave trains.

The last problem proposed for future consideration is motivated by the study on wave turbulence described in Chapter 5. In this case, the objective consists in studying the transition between the monochromatic plane surface-wave regime and Kolmogorov's turbulent state [52], characterized by, among other features, a continuous spectrum. With the ability to perform space-time measurements of the surface deformation, it could be indeed possible to observe the enrichment of the spectrum and, hopefully, the emergence of the continuous part. Experimentally, such enrichment could be easily achieved by progressively increasing the amplitude of the waves, or by the addition of obstacles and other sources inside the wave tank.

APPENDIX A

OTHER EXPERIMENTAL STUDIES CONDUCTED DURING THE COURSE OF THIS THESIS

This section presents briefly *preliminary* results of two additional experimental studies carried out during the course of this thesis. The first one concerns the time reversal of water waves, whereas the second comprises the study of drop impacts onto thin liquid films.

A.1 Time reversal of water waves

The preliminar results on the experimental study on time reversal of water waves presented in this section was carried out during the last months of this thesis, with Romain Denèfle in the frame of his *Projet de 3ème année de l'ESPCI* on water waves, which I have co-directed.

The experimental setup consists of a water-wave cavity in the form of an irregularily shaped container of plastic deformable walls filled with water up to a height of 5 cm. A linear motor drives a rod whose pointy tip is used to tap on the external side of one of the container's walls, thus creating a perturbation over the free surface. Fig. A.1(left panel) shows a photograph of the experimental setup, illustrating the container shape. For reference, its size is approximately 10×10 cm^2.

In the framework of these experiments, the perturbation transmitted by rod was chosen to be a harmonic oscillation convoluted by a Hanning window, as shown in Fig. A.2. The associated free surface deformation is measured in space and time by means of our optical profilometric technique, using a Phantom V9 camera employed at an acquisition rate of 200 fps at full resolution (1200×1600 px^2), leading to a resolution in the reconstruction of about 0.1 mm. The evolution of the surface was registered for a period of over 10 s.

Fig. A.1(right panel) shows an example of a typical experimental measurement of the free surface deformation field inside the cavity, corresponding to early stages in the injection of the pulse. The reconstruction shows clearly the excitation of a cylindrical surface wave (peak amplitude 2 mm), originated at the position of injection.

Next, a sampled point over the surface is selected and its amplitude signal is time-reversed and used as forcing *at that point over the surface* in a subsequent measurement. The aim of such a procedure is to observe an spatial reconstruction of the original perturbation. To that end, we

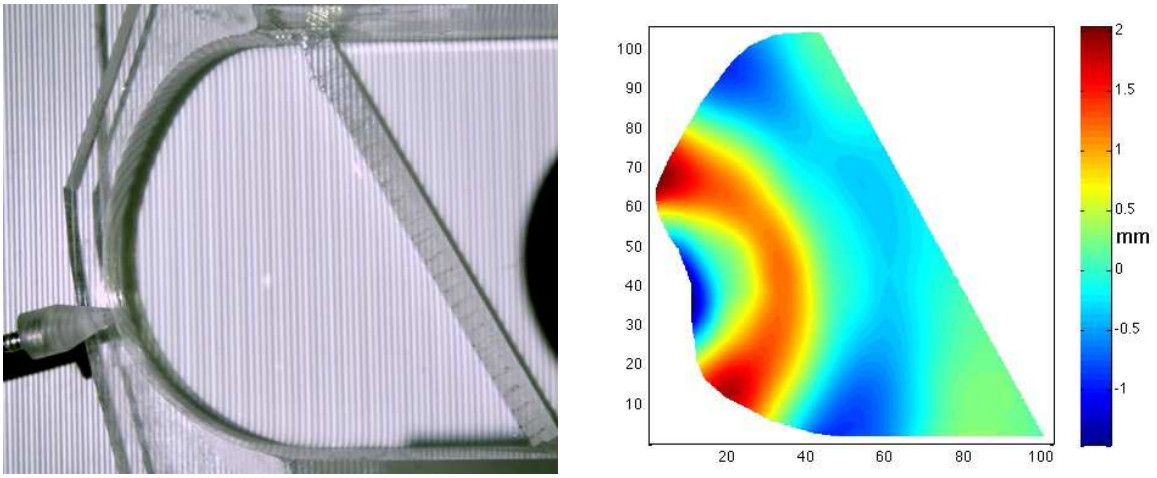


Figure A.1: Experimental results from a preliminar study on time reversal of water waves. *Left panel:* top view of the plastic container of plastic deformable walls filled with water. At the left border of the image, the rod used to inject a pulsed perturbation can be seen. Incidentally, the fringe pattern employed by our profilometric measuring technique is recognizable. *Right panel:* example of an experimental measurement of the free surface deformation field inside the container, corresponding to early stages in the injection of the pulse. The excitation of a cylindrical surface wave originated at the position of injection is clearly evidenced.

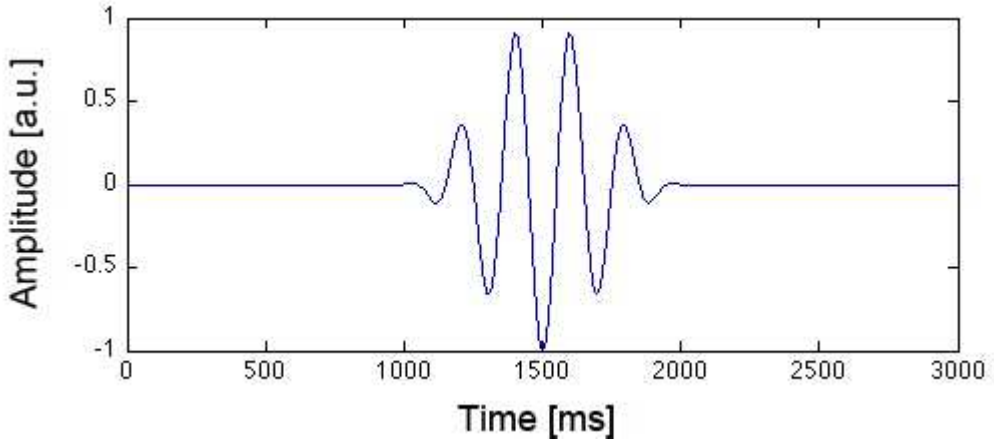


Figure A.2: Source pulse employed to excite surface waves inside our cavity.

choose an observation point inside the cavity near the point of injection of the original pulse.

The resulting curve, shown in Fig.A.3 corresponding to the measurements by our measuring technique at that point (in blue in the figure) reproduces well the local surface deformation resulting from the source pulse (shown in red). Indeed, a comparison of both curves shows that the key features of the original deformation are well reconstructed after time-inversion, yet the duration of the reconstructed pulse seems slightly longer. Whether this is due to the dispersive nature of water waves or not remains an open question that would need to be addressed in subsequent studies.

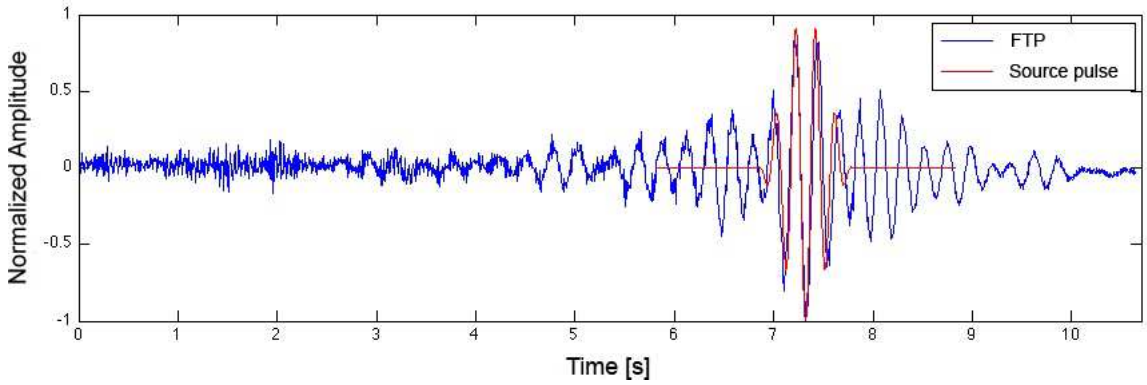


Figure A.3: Time-reversed pulse experimentally observed in water waves. In blue, we show the deformation of the free surface at the original injection point (near the wall) corresponding to reinjection of the original pulse. In red, the original free surface deformation observed at the injection point during the injection of the (original) pulse. [Both curves are represented in arbitrary units to facilitate comparison.]

A.2 Drop impact onto thin liquid films

In parallel to the experimental studies that constitute the main body of this thesis, we have also obtained promising preliminary results in the study of the drop impact onto thin liquid films.

The experimental protocol is as follows. A drop of about 2.5 mm in diameter is slowly released from a syringe and falls freely into a container holding a thin (~10 mm) layer of the same fluid at rest. The distance between the position of the syringe mouth and the free surface at rest is of approximately 50 cm. The time-evolution of the free-surface deformation is measured by our optical profilometric technique by the use of a Phantom V9 high-speed camera employed at an acquisition rate of 1000 fps at full resolution (1200×1600 px^2). One of the most important results of these preliminar tests was the observation that, although the measurement of the free surface shape is not be possible during the initial instants due to the abrupt splashing of the drop, subsequent stages are indeed well reconstructed.

Fig. A.4 depicts an example of the typical experimental results obtained in the frame of this study, corresponding to the space-time evolution of the free surface after the drop's impact. The figure is composed by a sequence of 10 selected snapshots equally spaced in time (from a total of over 2000 obtained for this particular impact) following the evolution of the surface deformation. In this series of snapshots, time evolves columnwise from top to bottom and from left to right. For reference, the liquid surface shown in these figures, which is just a portion of the total registered field, is sampled at a resolution of 800×1000 px^2.

Following the initial impact, a jet is observed in the first snapshot as well as a small circular crown surrounding it. In the following snapshots, the jet sunk into the layer and in its previous position we find a depression. However, the crown continues to grow and expand, as its lip develops a number of peaks. During this experiments, we have come to observe, to our surprise, that this arrangement in the form of peaks around the central dip is quite reproductible, as well as its discrete symmetry. During the subsequent instants the crown decreses in height as it continues to expand laterally. A new jet, emerging from its center is observed again. The last five snapshots show the evolution of the jet as it decreases gradually. Towards the end of the sequence, the surface

deformation is mainly dominated by the cylindrical surface waves generated by the impact.

The preliminary results presented in this section show that an experimental study of drop impacts onto liquid films can be successfully carried out by means of our optical profilometric technique. Furthermore, we anticipate that these experiments will allow precise and quantitative comparisons with theoretical investigations, providing also a firm ground for the validation of numerical models.

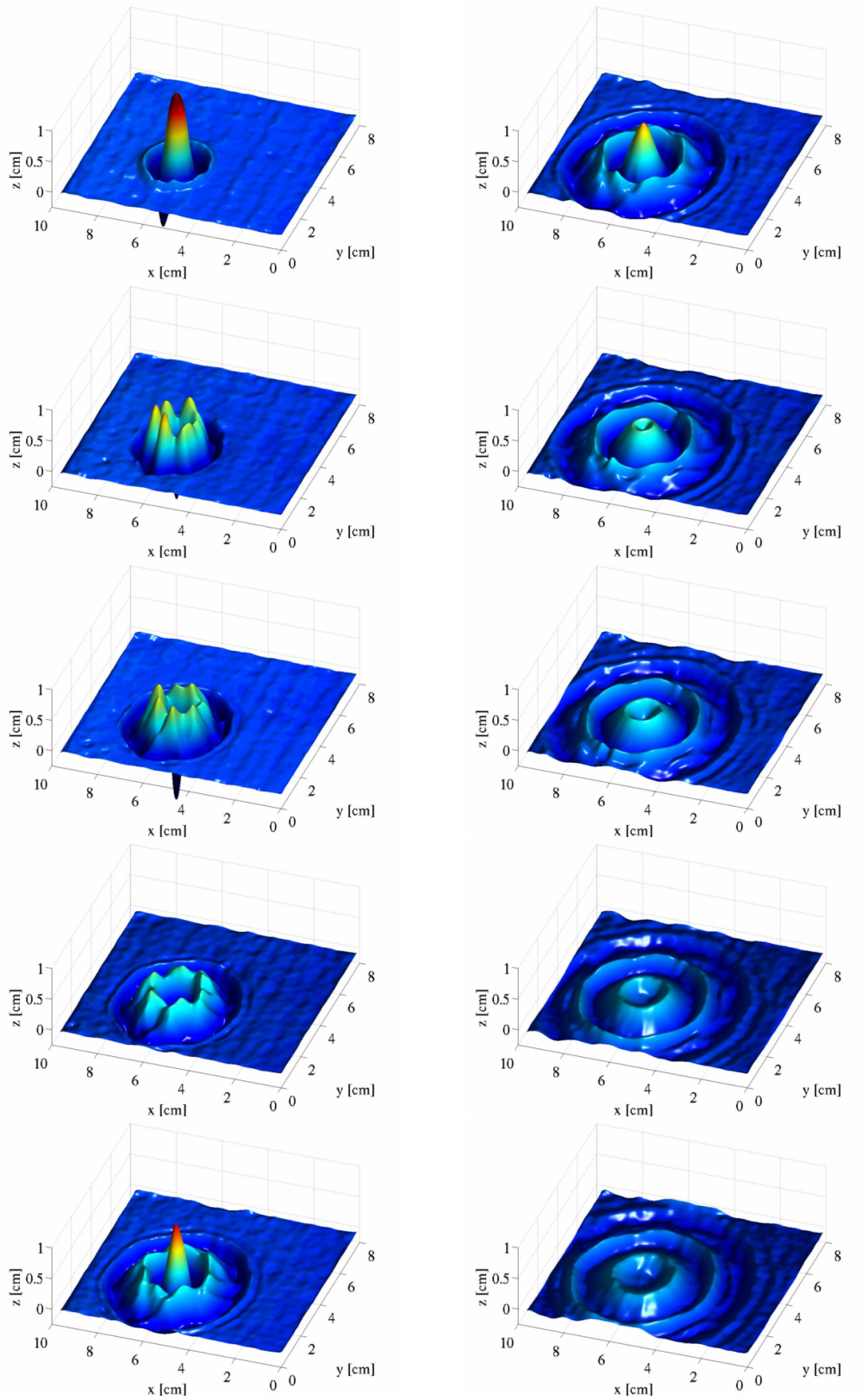


Figure A.4: Experimental measurements of a drop impact onto a thin liquid film of the same fluid. In this series of snapshots, time evolves columnwise from top to bottom and from left to right. The liquid surface shown in these figures is sampled at a resolution of 800×1000 px^2, using a high speed camera. [See text for further details.]

BIBLIOGRAPHY

[1] Y. Aharonov and D. Bohm. Significance of Electromagnetic Potentials in the Quantum Theory. *Physical Review*, 115:485–491, August 1959. doi: 10.1103/PhysRev.115.485.

[2] M. V. Berry, R. G. Chambers, M. D. Large, C. Upstill, and J. C. Walmsley. Wavefront dislocations in the Aharonov-Bohm effect and its water wave analogue. *European Journal of Physics*, 1:154–162, July 1980. doi: 10.1088/0143-0807/1/3/008.

[3] F. Berryman, P. Pynsent, and J. Cubillo. A theoretical comparison of three fringe analysis methods for determining the three-dimensional shape of an object in the presence of noise. *Optics and Lasers in Engineering*, 39:35–50, January 2003. doi: 10.1016/S0143-8166(02)00071-4.

[4] F. Berryman, P. Pynsent, and J. Cubillo. The effect of windowing in Fourier transform profilometry applied to noisy images. *Optics and Lasers in Engineering*, 41:815–825, June 2004. doi: 10.1016/S0143-8166(03)00061-7.

[5] A. Boudaoud, O. Cadot, B. Odille, and C. Touze. Observation of wave turbulence in vibrating plates. *Phys. Rev. Lett.*, 100:234504–1–4, 2008.

[6] M. Callan, C. M. Linton, and D. V. Evans. Trapped modes in two-dimensional waveguides. *J. Fluid. Mech.*, 229:51–64, 1991.

[7] P.-H. Chan, P. J. Bryanston-Cross, and T. R. Judge. Studies of Fourier transform profilometry. In R. J. Moorhead, D. E. Silver, & S. P. Uselton, editor, *Society of Photo-Optical Instrumentation Engineers (SPIE) Conference Series*, volume 2178 of *Society of Photo-Optical Instrumentation Engineers (SPIE) Conference Series*, pages 165–176, April 1994.

[8] W. Chen, Y. Hu, X. Su, and S. Tan. Error caused by sampling in Fourier transform profilometry. *Optical Engineering*, 38:1029–1034, June 1999. doi: 10.1117/1.602146.

[9] W. Chen, X. Su, Y. Cao, Q. Zhang, and L. Xiang. Method for eliminating zero spectrum in Fourier transform profilometry. *Optics and Lasers in Engineering*, 43:1267–1276, November 2005. doi: 10.1016/j.optlaseng.2004.12.002.

[10] P. J. Cobelli, A. Maurel, V. Pagneux, and P. Petitjeans. Global measurement of water waves by fourier transform profilometry. *Experiments in Fluids*, 46:1037–1047, 2009. doi: 10.1007/s00348-009-0611-z.

[11] P. J. Cobelli, V. Pagneux, A. Maurel, and P. Petitjeans. Experimental observation of trapped modes in a water wave channel. *Accepted for publication in Europhys. Lett.*, October 2009.

[12] P. J. Cobelli, P. Petitjeans, A. Maurel, V. Pagneux, and N. Mordant. Wave turbulence in a vibrating plate. *Submitted for publication in Phys. Rev. Lett.*, August 2009.

[13] S. Cochard and C. Ancey. Tracking the free surface of time-dependent flows: image processing for the dam-break problem. *Experiments in Fluids*, 44:59–71, January 2008. doi: 10.1007/s00348-007-0374-3.

[14] C. Coste and F. Lund. Scattering of dislocated wave fronts by vertical vorticity and the Aharonov-Bohm effect. II. Dispersive waves. *Phys. Rev. E*, 60:4917–4925, October 1999. doi: 10.1103/PhysRevE.60.4917.

[15] C. Coste, F. Lund, and M. Umeki. Scattering of dislocated wave fronts by vertical vorticity and the Aharonov-Bohm effect. I. Shallow water. *Phys. Rev. E*, 60:4908–4916, October 1999. doi: 10.1103/PhysRevE.60.4908.

[16] A. D. D. Craik. The Origins of Water Wave Theory. *Annual Review of Fluid Mechanics*, 36:1–28, 2004. doi: 10.1146/annurev.fluid.36.050802.122118.

[17] D. Dabiri. On the interaction of a vertical shear layer with a free surface. *Journal of Fluid Mechanics*, 480:217–232, April 2003. doi: 10.1017/S0022112002003671.

[18] P. Denissenko, S. Lukaschuk, and S. Nakarenko. Gravity wave turbulence in a laboratory flume. *Phys. Rev. Lett.*, 99:014501–1–4, 2007.

[19] D. G. Dommermuth, E. A. Novikov, and R. C. Y. Mui. The interaction of surface waves with turbulence. In *Proc. of the ASME Symp. on Free-Surface Turbulence*, 1994.

[20] C. Draeger and M. Fink. One-channel time reversal of elastic waves in a chaotic 2d-silicon cavity. *Phys. Rev. Lett.*, 73(3):407–410, 1997.

[21] G. Duclos and A. H. Clement. Wave propagation through arrays of unevenly spaced vertical piles. *Ocean Eng.*, 31:1655–1668, 2004.

[22] A. G. During, C. Josserand, and S. S. Rica. Weak turbulence for a vibrating plate: Can one hear a kolmogorov spectrum? *Phys. Rev. Lett.*, 97:025503–1–4, 2006.

[23] S. Dyachenko, A. C. Newell, A. Pushkarev, and V. E. Zakharov. Optical turbulence: weak turbulence, condensates and collapsing filaments in the nonlinear schrödinger equation. *Physica D*, 57:96–160, 1992.

[24] D. V. Evans and C. M. Linton. Trapped modes in open channels. *J. Fluid Mech.*, 225:153–175, 1991.

[25] D. V. Evans and C. M. Linton. Trapped modes in open channels. *J. Fluid Mech.*, 225:153–175, 1991.

[26] D. V. Evans and P. McIver. Trapped waves over symmetric thin bodies. *J. Fluid Mech.*, 223:509–519, 1991.

[27] D. V. Evans and R. Porter. Near-trapping of water waves by circular arrays of vertical cylinders. *Appl. Ocean Res.*, 19:83–89, 1997.

[28] D. V. Evans and R. Porter. Trapped modes about multiple cylinders in a channel. *J. Fluid Mech.*, 339: 331–356, 1997.

[29] D. V. Evans and R. Porter. Near-trapping of waves by circular arrays of vertical cylinders. *Appl. Ocean Res.*, 19:83–89, 1997.

[30] D. V. Evans and R. Porter. Trapping and near-trapping by arrays of cylinders in waves. *J. Eng. Math.*, 35:149–179, 1999.

[31] D. V. Evans and R. Porter. Trapping and near-trapping by arrays of cylinders in waves. *J. Eng. Math.*, 35:149–179, 1999.

[32] D. V. Evans and R. Porter. An example of non-uniqueness in the two-dimensional linear water-wave problem involving a submerged body. *Proc. R. Soc. Lond. A*, 454:3145–3165, 2002.

[33] D. V. Evans, M. Levitin, and D. Vassiliev. Existence theorems for trapped modes. *J. Fluid Mech*, 261: 21–31, 1994.

[34] E. Falcon, C. Laroche, and S. Fauve. Observation of gravity-capillary wave turbulence. *Phys. Rev. Lett.*, 98:094503–1–4, 2007.

[35] M. Farhat, S. Enoch, S. Guenneau, and A. B. Movchan. Broadband cylindrical acoustic cloak for linear surface waves in a fluid. *Phys. Rev. Lett.*, 101:134501–1–4, 2008.

[36] V. A. Fedotov, M. Rose, S. L. Prosvirnin, N. Papasimakis, and N. I. Zheludev. Sharp trapped-mode resonances in planar metamaterials with a broken structural symmetry. *Phys. Rev. Lett.*, 99:147401–1–4, 2007.

[37] S. Galtier, S. V. Nakarenko, A. C. Newell, and A. Pouquet. A weak turbulence theory for incompressible magnetohydrodynamics. *J. Plasma Phys.*, 63:447–488, 2000.

[38] M. A. Gdeisat, D. R. Burton, and M. J. Lalor. Eliminating the zero spectrum in Fourier transform profilometry using a two-dimensional continuous wavelet transform. *Optics Communications*, 266: 482–489, October 2006. doi: 10.1016/j.optcom.2006.05.070.

[39] M. Gharib and A. Weigand. Experimental studies of vortex disconnection and connection at a free surface. *Journal of Fluid Mechanics*, 321:59–86, 1996. doi: 10.1017/S0022112096007641.

[40] E. Granot. Emergence of a confined state in a weakly bent wire. *Phys. Rev. B*, 65(23):233101, May 2002. doi: 10.1103/PhysRevB.65.233101.

[41] I. Grant, N. Stewart, and I. A. Padilla-Perez. Topographical measurements of water waves using the projection moire method. *Appl. Optics*, 29:3981–3983, October 1990.

[42] R. Harter, I. D. Abrahams, and M. J. Simon. The effect of surface tension on trapped modes in water-wave problems. *Proc. R. Soc. A*, 463:3131–3149, 2007. doi: 10.1098/rspa.2007.0063.

[43] K. Hasselmann. On the non-linear energy transfer in a gravity-wave spectrum. part 1. general theory. *J. Fluid Mech.*, 12:481–500, 1962.

[44] E. Henry, P. Alstrom, and M. T. Levinsen. Prevalence of weak turbulence in strongly driven surface ripples. *Europhys. Lett.*, 52:27–32, 2000.

[45] X. Hu and C. T. Chan. Refraction of water waves by periodic cylinder arrays. *Phys. Rev. Lett.*, 95: 154501–1–4, 2005.

[46] X. Hu, Y. Shen, X. Liu, R. Fu, and J. Zi. Superlensing effect in liquid surface waves. *Phys. Rev. E*, 69: 030201–1–4, 2004.

[47] D. A. Huntley and A. J. Bowen. Field observations of edge waves. *Nature*, 243:349–365, 1973.

[48] R. S. Johnson. Edge waves: theories past and present. *Phil. Trans. R. Soc. A*, 365:2359–2376, 2007.

[49] D. S. Jones. The eigenvalues of $\nabla^2 u + \lambda u = 0$ when the boundary conditions are given in semi-infinite domains. *Proc. Camb. Phil. Soc.*, 49:668–684, 1953.

[50] J. D. Kaplunov and S. V. Sorokin. A simple example of a trapped mode in an unbounded waveguide. *J. Acoust. Soc. Am.*, 97:3898–3899, 1995.

[51] E. A. Kartashova. Weakly nonlinear theory of finite-size effects in resonators. *Phys. Rev. Lett.*, 72: 2013–2016, 1994.

[52] A. N. Kolmogorov. The local structure of turbulence in incompressible viscous fluid for very large Reynolds numbers. *Royal Society of London Proceedings Series A*, 434:9–13, July 1991.

[53] S. S. Kurennoy. Trapped modes in waveguides with many small discontinuities. *Phys. Rev. E*, 51:2498–2509, 1995.

[54] N. G. Kuznetsov and P. McIver. On uniqueness and trapped modes in the water-wave problem for a surface-piercing axisymmetric body. *Q. J. Mech. Appl. Math.*, 50(4):565–580, 1997.

[55] P. H. LeBlond and L. A. Mysak. *Waves in the ocean*. Elsevier, 1978.

[56] C. M. Linton and D. V. Evans. Integral equations for a class of problems concerning obstacles in waveguides. *J. Fluid Mech.*, 245:349–365, 1992.

[57] C. M. Linton and M. McIver. The existence of rayleigh–bloch surface waves. *J. Fluid Mech.*, 470:85–90, 2002.

[58] C. M. Linton and P. McIver. *Handbook of Mathematical Techniques for Wave/Structure Interactions*. CRC Press, 2001.

[59] C. M. Linton and P. McIver. *Handbook of Mathematical Techniques for Wave/Structure Interactions*. CRC Press, 2001.

[60] C. M. Linton and P. Parker. Embedded trapped modes in water waves and acoustics. *Wave Motion*, 45: 16–29, 2007.

[61] V. S. L'vov, S. V. Nakarenko, and O. Rudenko. Bottleneck crossover between classical and quantum superfluid turbulence. *Phys. Rev. B*, 76:024520–1–9, 2007.

[62] D. H. D. Maniar and J. N. Newman. Waves diffraction by a long array of cylinders. *J. Fluid Mech.*, 339: 309–330, 1997.

[63] X. Mao, W. Chen, X. Su, G. Xu, and X. Bian. Fourier transform profilometry based on a projecting-imaging model. *Journal of the Optical Society of America A*, 24:3735–+, 2007. doi: 10.1364/JOSAA.24.003735.

[64] A. Maurel, P. Cobelli, V. Pagneux, and P. Petitjeans. Experimental and theoretical inspection of the phase-to-height relation in Fourier transform profilometry. *Appl. Optics*, 48:380–+, January 2009. doi: 10.1364/AO.48.000380.

[65] A. Maurel, P. J. Cobelli, V. Pagneux, and P. Petitjeans. Experimental and theoretical inspection of the phase-to-height relation in fourier transform profilometry. *Applied Optics*, 48:380–392, 2009.

[66] M. McIver. An example of non-uniqueness in the two-dimensional linear water wave problem. *J. Fluid Mech.*, 315:257–266, 1996.

[67] M. McIver. Trapped modes supported by submerged obstacles. *Proc. R. Soc. Lond. A*, 456:1851–1860, 2000.

[68] M. McIver and R. Porter. Trapping of waves by a submerged elliptical torus. *J. Fluid Mech.*, 456:277–293, 2002.

[69] P. McIver. Trapping of surface water waves by fixed bodies in channels. *Q. J. Mech. Appl. Maths*, 44(2): 193–208, 1991. doi: 10.1093/qjmam/44.2.193.

[70] P. McIver. Trapping of surface water waves by fixed bodies in channels. *Q. J. Mechanics Appl. Math.*, 44(2):193–208, 1991.

[71] P. McIver. Wave interaction with arrays of structures. *Applied Ocean Research*, 24:121–126, 2002.

[72] P. McIver and D. V. Evans. The trapping of surface waves above a submerged, horizontal cylinder. *J. Fluid Mech.*, 151:243–255, 1985.

[73] P. McIver and M. McIver. Trapped modes in an axisymmetric water wave problem. *Q. J. Mech. Appl. Math.*, 50(2):165–178, 1997.

[74] P. McIver and M. McIver. Trapped modes in the water-wave problem for a freely floating structure. *J. Fluid Mech.*, 558:53–67, 2006.

[75] P. McIver and J. N. Newman. Trapping structures in the three dimensional water-wave problem. *J. Fluid Mech.*, 484:283–302, 2003.

[76] N. Mordant. Are there waves in elastic wave turbulence? *Phys. Rev. Lett.*, 100:234505–1–4, 2008.

[77] A. C. Newell, S. Nazarenko, and L. Biven. Wave turbulence and intermittency. *Physica D*, 152:520–550, 2001.

[78] C. S. Ng and A. Bhattacharjee. Interaction of shear-alfven wave packets: Implication for weak magnetohydrodynamic turbulence in astrophysical plasmas. *Astrophysical Journal*, 465:845–854, 1996.

[79] V. Pagneux. Revisiting the edge resonance for lamb waves in a semi-infinite plate. *J. Acoust. Soc. Am.*, 120(2):649–656, 2006.

[80] N. F. Parsons and P. A. Martin. Trapping of water waves by submerged plates using hypersingular integral equations. *J. Fluid Mech.*, 284:359–375, 1995.

[81] K. Patorski and M. Kujawinska. *Handbook of the Moiré Fringe Technique.* Elsevier, Amsterdam, 1993.

[82] O. P. Philips. Spectral and statistical properties of the equilibrium range in wind-generated gravity waves. *J. Fluid Mech.*, 156:505–531, 1985.

[83] C. Quan, C. J. Tay, H. M. Shang, and P. J. Bryanston-Cross. Contour measurement by fibre optic fringe projection and Fourier transform analysis. *Optics Communications*, 118:479–483, February 1995. doi: 10.1016/0030-4018(95)00287-I.

[84] B. A. Rajoub, D. R. Burton, and M. J. Lalor. A new phase-to-height model for measuring object shape using collimated projections of structured light. *Journal of Optics A: Pure and Applied Optics*, 7:368–+, June 2005. doi: 10.1088/1464-4258/7/6/018.

[85] B. A. Rajoub, M. J. Lalor, D. R. Burton, and S. A. Karout. A new model for measuring object shape using non-collimated fringe-pattern projections. *Journal of Optics A: Pure and Applied Optics*, 9:66–+, June 2007. doi: 10.1088/1464-4258/9/6/S10.

[86] C. H. Retzler. Trapped modes: an experimental investigation. *Appl. Ocean Res.*, 23:249–250, 2001.

[87] V. P. Ruban. Interaction of a vortex ring with the free surface of an ideal fluid. *Phys. Rev. E*, 62:4950–4958, October 2000. doi: 10.1103/PhysRevE.62.4950.

[88] R. Savelsberg and W. van de Water. Experiments on free-surface turbulence. *Journal of Fluid Mechanics*, 619:95–+, December 2008. doi: 10.1017/S0022112008004369.

[89] R. Savelsberg and W. van de Water. Turbulence of a Free Surface. *Physical Review Letters*, 100(3): 034501–+, January 2008. doi: 10.1103/PhysRevLett.100.034501.

[90] R. Savelsberg, A. Holten, and W. van de Water. Measurement of the gradient field of a turbulent free surface. *Experiments in Fluids*, 41:629–640, October 2006. doi: 10.1007/s00348-006-0186-x.

[91] D. Snouk, M. T. Westra, and W. van de Water. Turbulent parametric surface waves. *Phys. Fluids*, 21: 025102–1–8, 2009.

[92] G. S. Spagnolo, G. Guattari, C. Sapia, D. Ambrosini, D. Paoletti, and G. Accardo. Contouring of artwork surface by fringe projection and FFT analysis. *Optics and Lasers in Engineering*, 33:141–156, February 2000. doi: 10.1016/S0143-8166(00)00023-3.

[93] G. G. Stokes. Report on recent researches in hydrodynamics. *Report to 16th Meeting Brit Assoc. Adv. Sci., Southampton, Murrey, London*, pages 1–20, 1846.

[94] X. Su and W. Chen. Fourier transform profilometry: - a review. *Optics and Lasers in Engineering*, 35: 263–284, May 2001. doi: 10.1016/S0143-8166(01)00023-9.

[95] X. Su and W. Chen. Reliability-guided phase unwrapping algorithm: a review. *Optics and Lasers in Engineering*, 42:245–261, September 2004. doi: 10.1016/j.optlaseng.2003.11.002.

[96] X. Su, W. Chen, Q. Zhang, and Y. Chao. Dynamic 3-D shape measurement method based on FTP. *Optics and Lasers in Engineering*, 36:49–64, July 2001. doi: 10.1016/S0143-8166(01)00028-8.

[97] M. Takeda and K. Mutoh. Fourier transform profilometry for the automatic measurement of 3-D object shapes. *Appl. Optics*, 22:3977–3982, December 1983.

[98] M. Takeda and K. Mutoh. Fourier tranform profilometry for the automatic measurement of 3-d object shapes. *Appl. Opt.*, 22:3977–3982, 1983.

[99] M. Takeda, H. Ina, and S. Kobayashi. Fourier-transform method of fringe-pattern analysis for computer-based topography and interferometry. *Journal of the Optical Society of America (1917-1983)*, 72:156–+, January 1982.

[100] M. Takeda, H. Ina, and S. Kobayashi. Fourier-transform method of fringe-pattern analysis for computer-based topography and interferometry. *J. Opt. Soc. Am.*, 72:156, 1982.

[101] R. Tsubaki and I. Fujita. Stereoscopic measurement of a fluctuating free surface with discontinuities. *Measurement Science and Technology*, 16:1894–1902, October 2005. doi: 10.1088/0957-0233/16/10/003.

[102] F. Ursell. Trapping modes in the theory of surface waves. *Proc. Camb. Phil. Soc.*, 47:1346–358, 1951.

[103] F. Ursell. Edge waves on a sloping beach. *Proc. Roy. Soc. A*, 214:79–97, 1952.

[104] F. Ursell. Mathematical aspects of trapping modes in the theory of surface waves. *J. Fluid Mech.*, 183: 421–437, 1987.

[105] F. Vivanco and F. Melo. Surface Spiral Waves in a Filamentary Vortex. *Physical Review Letters*, 85: 2116–2119, September 2000. doi: 10.1103/PhysRevLett.85.2116.

[106] F. Vivanco and F. Melo. Experimental study of surface waves scattering by a single vortex and a vortex dipole. *Phys. Rev. E*, 69(2):026307–+, February 2004. doi: 10.1103/PhysRevE.69.026307.

[107] D. T. Walker, C.-Y. Chen, and W. W. Willmarth. Turbulent structure in free-surface jet flows. *Journal of Fluid Mechanics*, 291:223–261, 1995. doi: 10.1017/S0022112095002680.

[108] W. B. Wright, R. Budakian, and S. J. Putterman. Diffusing Light Photography of Fully Developed Isotropic Ripple Turbulence. *Physical Review Letters*, 76:4528–4531, June 1996. doi: 10.1103/PhysRevLett.76.4528.

[109] W. B. Wright, R. Budakian, D. J. Pine, and S. J. Putterman. Imaging of intermittency in ripple-wave turbulence. *Science*, 278:1609–1612, 1997.

[110] J. Yi. Modified fourier transform profilometry for the measurement of 3-D steep shapes. *Optics and Lasers in Engineering*, 27:493–505, July 1997. doi: 10.1016/S0143-8166(96)00042-5.

[111] E. Zappa and G. Busca. Comparison of eight unwrapping algorithms applied to Fourier-transform profilometry. *Optics and Lasers in Engineering*, 46:106–116, February 2008. doi: 10.1016/j.optlaseng.2007.09.002.

[112] D. Z. Zhang and A. Prosperetti. Ensemble phase-averaged equations for bubbly flows. *Physics of Fluids*, 6:2956–2970, September 1994. doi: 10.1063/1.868122.

[113] Q.-C. Zhang and X.-Y. Su. An optical measurement of vortex shape at a free surface. *Optics Laser Technology*, 34:107–113, March 2002. doi: 10.1016/S0030-3992(01)00097-4.

[114] X. Zhang. An algorithm for calculating water surface elevations from surface gradient image data. *Experiments in Fluids*, 21:43–48, May 1996. doi: 10.1007/BF00204634.

[115] X. Zhang and C. S. Cox. Measuring the two-dimensional structure of a wavy water surface optically: A surface gradient detector. *Experiments in Fluids*, 17:225–237, August 1994. doi: 10.1007/BF00203041.

[116] X. Zhang, D. Dabiri, and M. Gharib. Optical mapping of fluid density interfaces: Concepts and implementations. *Review of Scientific Instruments*, 67:1858–1868, May 1996. doi: 10.1063/1.1146990.

[117] B. Zhao and A. K. Asundi. Discussion on spatial resolution and sensitivity of fourier transform fringe detection. *Optical Engineering*, 39:2715–2719, October 2000. doi: 10.1117/1.1290683.

[118] J. Zhong and J. Weng. Spatial Carrier-Fringe Pattern Analysis by Means of Wavelet Transform: Wavelet Transform Profilometry. *Appl. Optics*, 43:4993–4998, September 2004. doi: 10.1364/AO.43.004993.